

# Investigation and Control of Beam Instabilities at the Karlsruhe Research Accelerator using a 3-D Digital Bunch-by-Bunch Feedback System

Zur Erlangung des akademischen Grades eines  
DOKTORS DER NATURWISSENSCHAFTEN (Dr. rer. nat.)

von der KIT-Fakultät für Physik  
des Karlsruher Instituts für Technologie (KIT)

angenommene  
DISSERTATION

von

Dipl.-Phys.  
**Edmund Blomley**

Tag der mündlichen Prüfung: 09. Juli 2021  
Referentin: **Prof. Dr. Anke-Susanne Müller**  
Korreferent: **Prof. Dr. Günter Quast**

---



This document is licensed under a Creative Commons Attribution 4.0 International License (CC BY 4.0): <https://creativecommons.org/licenses/by/4.0/deed.en>

# Contents

<b>1</b>	<b>Introduction</b>	<b>1</b>
<b>2</b>	<b>Accelerator Physical Background</b>	<b>5</b>
2.1	Electric and Magnetic Fields . . . . .	5
2.1.1	Static Magnetic Fields . . . . .	6
2.1.2	Fields in Radio Frequency Cavities . . . . .	7
2.2	Hamiltonian Formalism . . . . .	9
2.2.1	Straight Beam Line . . . . .	10
2.2.2	Curved Beam Line . . . . .	12
2.2.3	Liouville's Theorem . . . . .	13
2.3	Beam Dynamics . . . . .	13
2.3.1	Common Components . . . . .	13
2.3.2	Linear Optics . . . . .	17
2.3.3	Synchrotron Motion . . . . .	18
2.3.4	Tunes and Resonances . . . . .	20
2.3.5	Chromaticity and Dynamic Aperture . . . . .	22
2.3.6	Synchrotron Radiation . . . . .	24
2.4	Collective Effects . . . . .	27
2.4.1	Space Charge . . . . .	27
2.4.2	Scattering . . . . .	27
2.4.3	Wake Fields and Impedance . . . . .	28
2.4.4	Coupled-bunch instabilities . . . . .	29
2.4.5	Single-bunch instabilities . . . . .	32
<b>3</b>	<b>Karlsruhe Research Accelerator</b>	<b>33</b>
3.1	Injector . . . . .	33
3.1.1	Electron Source . . . . .	33
3.1.2	Booster Synchrotron . . . . .	34
3.2	Storage Ring . . . . .	36
3.2.1	Magnetic Lattice . . . . .	36
3.2.2	RF System . . . . .	38
3.2.3	Vacuum Chamber . . . . .	39
3.2.4	Insertion Devices . . . . .	39
3.3	Operation . . . . .	40
3.3.1	Injection & Energy Ramp . . . . .	40

---

---

3.3.2	Standard Operation . . . . .	41
3.3.3	Short Bunch Operation . . . . .	42
3.3.4	Other Beam Operation . . . . .	43
<b>4</b>	<b>Bunch-by-Bunch Feedback System</b>	<b>45</b>
4.1	Setup . . . . .	45
4.1.1	Beam Pick-Up . . . . .	46
4.1.2	Processing . . . . .	46
4.1.3	Transverse Feedback . . . . .	47
4.1.4	Longitudinal Feedback . . . . .	49
4.2	Configuration . . . . .	50
4.2.1	Temporal and Phase Alignment . . . . .	50
4.2.2	Feedback Filter . . . . .	51
4.3	Advanced Features . . . . .	53
4.3.1	Drive Sources . . . . .	53
4.3.2	Data Acquisition . . . . .	53
<b>5</b>	<b>Tune Diagnostics</b>	<b>57</b>
5.1	Measurement Techniques . . . . .	57
5.1.1	Excitation Measurement . . . . .	58
5.1.2	Feedback Measurement . . . . .	59
5.1.3	Phase Tracking Measurement . . . . .	64
5.2	Tune Dynamics . . . . .	69
5.2.1	Tune Influences . . . . .	69
5.2.2	Tune Stability Considerations . . . . .	70
5.2.3	Long Term Observation . . . . .	71
5.3	Chromaticity Measurements . . . . .	76
5.3.1	Measurement Technique . . . . .	76
5.3.2	Measurement Stability . . . . .	79
5.3.3	Operational Chromaticity . . . . .	79
5.3.4	Improved Tune Data Source . . . . .	79
5.3.5	Natural Chromaticity . . . . .	80
5.3.6	Future Improvements . . . . .	83
5.4	Tune Shift Due to Resistive-Wall Impedance . . . . .	83
5.4.1	Prior Work . . . . .	83
5.4.2	Dynamic Contributions . . . . .	84
5.4.3	Evolution of Tune Shifts . . . . .	88
5.4.4	Conclusion . . . . .	89
<b>6</b>	<b>Beam Dynamics</b>	<b>91</b>
6.1	Filling Pattern Manipulation . . . . .	91
6.1.1	Bunch Cleaning . . . . .	92
6.1.2	Single Bunch Injection . . . . .	93
6.1.3	Custom Filling Pattern . . . . .	94

---

---

6.2	Transverse Beam Damping . . . . .	97
6.2.1	Single-Kick Excitation . . . . .	97
6.2.2	Effect of BBB Feedback . . . . .	99
6.2.3	Improved Beam Stability . . . . .	103
6.3	Bunch Lengthening . . . . .	104
6.4	Longitudinal Beam Dynamics . . . . .	107
6.4.1	Eigenmodes during Injection and Energy Ramp . . . . .	107
6.4.2	Grow-Damp Measurements . . . . .	107
6.4.3	Temperature Dependency of Eigenmodes . . . . .	108
<b>7</b>	<b>Summary</b>	<b>115</b>
<b>8</b>	<b>Appendix</b>	<b>119</b>
A	Data Archiving at KARA . . . . .	119
A.1	Database Concept . . . . .	119
A.2	Compression Intervals . . . . .	120
A.3	Data Resampling . . . . .	122
A.4	Data Filtering . . . . .	122
A.5	Conclusion . . . . .	123
B	Indexing KARA Operation . . . . .	123
B.1	Motivation . . . . .	124
B.2	Filters . . . . .	124
B.3	Index Management . . . . .	126
B.4	Current Status . . . . .	127
B.5	Further Plans . . . . .	127
C	Python Framework . . . . .	128
C.1	Motivation . . . . .	128
C.2	Module overview . . . . .	128
C.3	Status and Further Plans . . . . .	130
	<b>Acronyms</b>	<b>131</b>
	<b>Bibliography</b>	<b>133</b>
	<b>Acknowledgments</b>	<b>139</b>

---



# 1. Introduction

Particle accelerators are complex large research infrastructures. The largest at present, the *Large Hadron Collider (LHC)* at *CERN*, is at the forefront of fundamental particle physics research. But even at smaller scales, the ability to successfully operate a particle accelerator requires a unique mixture of knowledge, experience, and workforce across many different disciplines. And even small accelerators, such as the Karlsruhe Research Accelerator (KARA) with only 110 m circumference compared to the 27 km of LHC being no less complex, provide opportunities for groundbreaking research and development of new diagnostics, as well as for applications across many different other scientific disciplines from medicine, biology, chemistry, material sciences, and to applications in arts and archeology. With relevant timescales in the micro- and nanoseconds regime and electrons oscillating nearly with the speed of light many million times per second, such a task requires sophisticated equipment to even provide a glimmer of information about the state and attributes of the beam motion. The highest and most difficult discipline in this regard, after being able to measure and being able to influence the beam, is the full control of the beam motion. Only the full control of beam motion allows certain effects to be systematically and fundamentally studied with the necessary precision. This in turn often leads to a better understanding of the challenges at hand and can thus ultimately lead to general improvements of the accelerator. The Bunch-by-Bunch (BBB) feedback system of KARA is such a tool which allows full control of certain aspects of beam motion. This thesis presents the work enabled by the system at KARA to study and improve beam operations, as well as provide new opportunities for applied beam physics which would not be otherwise possible.

The first part, Chapter 2, will try to give a brief overview of the field of accelerator physics involved. Starting with the fundamental Maxwell equations and the Lorentz force it will discuss the basics of every accelerator: Magnetic fields created by magnets of varying order and electric fields created by radio-frequency cavities. After that, it will introduce the Hamilton formalism which allows the properties of circular motion at the speed of light to be written and used more easily so as to be able to understand basic properties of a particle accelerator, more particularly, how the presence of electric- and magnetic fields leads to

---

transverse and longitudinal beam motion. Effects such as a self-preserving focusing, but also synchrotron radiation are important to understand how any particle accelerator can operate. Models are an important approach for applied accelerator physics, so some models, such as the linear optics model, are shown. But the most relevant non-linear effects are also mentioned. Finally, since many particles are present at all times, a short introduction into collective effects is given with some focus on instabilities between individual bunches or particles.

After the introduction to accelerator physics, Chapter 3 will present the Karlsruhe Research Accelerator (KARA). This includes a brief overview of the pre-accelerators required to even get a basic particle beam into the accelerator itself. Important aspects of the storage ring for later parts of the thesis are presented, including the magnetic lattice, the layout of the radio frequency (RF) system, the basic design of the vacuum chamber, and presence of insertion devices will be mentioned. After that, the chapter will end with discussing the different operation modes and regime KARA can and does operate in.

Chapter 4 will focus on the main tool of this thesis: BBB feedback system itself. At first, the basic working principle of detecting and acting on bunch-by-bunch motion is shown. This is followed by a overview of the configuration and setup options required to successfully apply the system. The last part will discuss the details of how the system can influence and analyse beam motion and which options it provides.

Chapter 5 will focus on one application of the BBB feedback system: It provides continuous readout of the tunes which serve as a characteristic parameter for the state of the accelerator. A detailed discussion of different approaches with which the tunes can be measured, followed by consideration of the basic limits and errors. While tunes typically are described as a fixed working point of the accelerator, especially in the context of the operation of KARA at different energy levels and in different beam optics, the tunes actually do change over the course of operation. The range and potential issues, with examples of certain scenarios are discussed, as well as showing how the change and possible area of tune motion can be visualized with the help of tune diagrams. This is followed by a detailed discussion of chromaticity measurements which depends on tune measurements. Since the BBB feedback system provides easy access to the tune values, significant contributions could be made which improve the availability and ease of use of chromaticity measurements. Additionally, measurements of the natural chromaticity are shown, which would not be possible without the BBB feedback system providing the necessary environment for preventing immediate beam losses. Lastly, the chapter will end with investigations of the transverse impedance, another effect which can be derived based on precise tune measurements.

Chapter 6 will focus on a very different topic: Beam dynamics, active measurements of beam motion, and other applications enabled by the BBB feedback system. First, it will discuss the filling pattern, which is the basic layout of filled and empty bunches. With

---

the capabilities provided by the BBB feedback system, it is possible to precisely act on individual bunches, which then opens up certain applications that would be unobtainable or much more difficult to achieve without the system. Some of the research of colleagues, whose work has enabled this, will be briefly mentioned. The next section discusses the effects of the feedback system on the transverse damping times of the beam motion: In which way the damping times can be influenced and which benefits this provides to the general operation and stability of KARA. The following section will move to the longitudinal plane of motion and discuss a special application in which the feedback system is used to excite specific beam motion and how this can improve injection efficiency in certain scenarios. The final section will focus on the complex structure of the Eigenmodes of longitudinal motion. Using the feedback system a systematic investigation into which Eigenmodes which are present at KARA is presented and how the modal composition will change if the main driver of these modes, so-called higher order mode (HOM) in the RF cavities, are changed.

Chapter 7 will summarize the thesis. The measurements and especially the tools which were developed to enable the measurements are discussed and put into context of future research opportunities.

Finally the Appendix documents some of the major challenges involved in accessing and processing the vast amount of data produced by the accelerator on a daily basis, as well as giving a brief overview of the tools developed to access and work with that data.

---



## 2. Accelerator Physical Background

Modern particle accelerators are highly complex large research facilities. They are found in many countries around the world serving many different purposes. Based on this chosen purpose, the actual design and the details of the relevant accelerator physics can vary significantly: There are linear and ring structures, colliders and synchrotron radiation sources, electron and ion accelerators. This chapter will only look at accelerator physics relevant for a discussion of the effects that are relevant for the Karlsruhe Research Accelerator (KARA), an electron storage ring and synchrotron radiation facility. This chapter serves as a broad overview of the fundamentals of a modern accelerator. It closely follows the excellent book *Beam Dynamics in High Energy Particle Accelerators* [1]. For the clarity of reading, the explicit citations of every equation and derivation is omitted in most cases. If not explicitly cited from a different source, it was taken from [1]. Typically at the end of each section, a citation with the relevant page numbers is given.

### 2.1 Electric and Magnetic Fields

Charged particles are influenced by electric and magnetic fields. Therefore – on an abstract level – a particle accelerator can be seen as a combination of such fields. The foundation for this is expressed using the Maxwell's equation in differential form:

$$\nabla \cdot \mathbf{D} = \rho, \quad (2.1)$$

$$\nabla \cdot \mathbf{B} = 0, \quad (2.2)$$

$$\nabla \times \mathbf{H} = \mathbf{J} + \frac{\partial \mathbf{D}}{\partial t}, \quad (2.3)$$

$$\nabla \times \mathbf{E} = -\frac{\partial \mathbf{B}}{\partial t}. \quad (2.4)$$

As well as the equation for the Lorentz force:

$$\mathbf{F} = q(\mathbf{E} + \mathbf{v} \times \mathbf{B}), \quad (2.5)$$

---

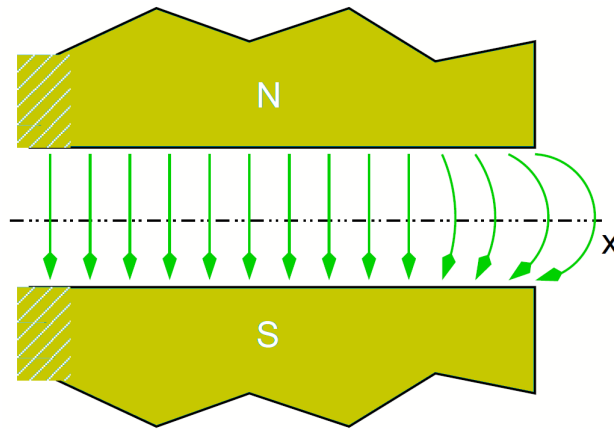


Figure 2.1: Cross-section of a dipole magnet. The magnetic field is vertical and static leading to a horizontal deflection with a defined radius. For the region of interest where particles experience it, the field it is homogeneous. Adapted from [2].

with the magnetic flux density  $\mathbf{B}$  and the electric field strength  $\mathbf{E}$  determining the force  $\mathbf{F}$  on a particle of charge  $q$  travelling with velocity  $\mathbf{v}$ . The electric displacement  $\mathbf{D}$  and magnetic intensity  $\mathbf{H}$  are related to the magnetic flux and the electric field by:

$$\mathbf{D} = \varepsilon_0 \mathbf{E}, \quad (2.6)$$

$$\mathbf{B} = \mu_0 \mathbf{H} \quad (2.7)$$

with  $\varepsilon_0$  and  $\mu_0$  being the electric permittivity and magnetic permeability for the vacuum case, which is generally assumed for the inside of the vacuum chambers of a particle accelerator. As long as the permittivity and permeability is constant the principle of superposition allows to be decomposed complex fields into a set of multipoles, which will be very useful for the discussion of magnetic fields [1, p.4-6].

### 2.1.1 Static Magnetic Fields

Magnets are used to steer and focus particle beams. The boundary conditions inside the vacuum chamber can be seen as a region of space free of charges and currents. Then, in addition to the second Maxwell equation 2.2, the magnetic field must satisfy:

$$\nabla \times \mathbf{B} = 0. \quad (2.8)$$

A field of the form  $\mathbf{B} = (B_x, B_y, B_z)$  with  $B_z = 0$  and  $B_x$  and  $B_y$ :

$$B_y + iB_x = C_n (x + iy)^{n-1} \quad (2.9)$$

fulfill these two boundary conditions, with  $C_n$  being a complex constant. This field is called a multipole with  $n$  indicating the order of the multipole. While it would be possible to sum the right hand side of 2.9 creating a composed field of multiple orders, only pure multipoles will be discussed here. The strength of a multipole can be defined as the normalised strength  $k_n$ :

$$k_n = \frac{q}{P_0} \frac{\partial^n B_y}{\partial x^n} \quad (2.10)$$

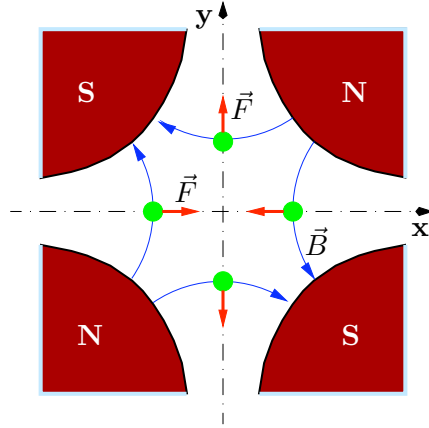


Figure 2.2: Cross-section of a quadrupole magnet. There is no field component in the center of the quadrupole and a linear force on particles off-axis either deflects the particle towards the center or in the opposite direction, depending on where the particle enters the field. If the horizontal or vertical plane leads to particles being forced to the center, this can be changed by inverting the polarity of the magnet. Adapted from [2].

with  $P_0$  being the so-called reference momentum of an ideal particle. In practice, long parallel wires can be combined around iron cores to generate pure multipole fields of any order [1, p.13-18]. Magnets with these pure multipoles for the first three orders are referred to as dipoles ( $n = 1$ ), quadrupoles ( $n = 2$ ), and sextupoles ( $n = 3$ ). Field distributions for dipole and quadrupole magnets are shown in Figures 2.1 and 2.2, whereas the sextupole magnet will be discussed in later sections of this chapter.

### 2.1.2 Fields in Radio Frequency Cavities

While it is sufficient to discuss static two dimensional fields for steering charged particles, the acceleration requires an electric field with an effective component parallel to the travel path of the reference particle. Additionally, acceleration above the MeV range requires oscillating electric fields. One option to generate these fields is by using a RF cavity. The region inside the cavity is treated as a vacuum in the same way as the interior of the vacuum chamber in general, with the walls as an ideal conductor. Maxwell's equation in free space leads to wave-like solutions for the electric and magnetic fields and, due to the boundary conditions of the cavity, these are satisfied by standing waves. Starting with the fourth Maxwell equation 2.4, the following wave equation can be found:

$$\nabla^2 \mathbf{E} - \frac{1}{c^2} \frac{\partial^2 \mathbf{E}}{\partial t^2} = 0 \quad (2.11)$$

with  $c = \frac{1}{\sqrt{\mu_0 \epsilon_0}}$ . A similar solution is obtained starting from the third Maxwell equation 2.3 for the magnetic field:

$$\nabla^2 \mathbf{B} - \frac{1}{c^2} \frac{\partial^2 \mathbf{B}}{\partial t^2} = 0. \quad (2.12)$$

Solutions for these wave equations are:

$$\mathbf{E} = \mathbf{E}_0 e^{i(\mathbf{k} \cdot \mathbf{x} - \omega t)} \quad (2.13)$$

$$\mathbf{B} = \mathbf{B}_0 e^{i(\mathbf{k} \cdot \mathbf{x} - \omega t)} \quad (2.14)$$

with the dispersion relation between the wave vector  $\mathbf{k}$  and the frequency  $\omega$ :

$$|k| = \frac{\omega}{c}. \quad (2.15)$$

Equations 2.13 and 2.14 cannot fulfill the necessary boundary conditions of a RF cavity, but the actual solutions for standing waves in a cavity can be seen as a superposition of plane wave solutions. Assuming a cylindrical cavity using cylindrical polar coordinates, one set of solutions can be expressed as follows:

$$E_r = -E_0 \frac{k_z}{k_r} J'_n(k_r r) \cos(n\theta) \sin(k_z z) e^{-i\omega t}, \quad (2.16)$$

$$E_\theta = E_0 \frac{nk_z}{k_r^2 r} J_n(k_r r) \sin(n\theta) \sin(k_z z) e^{-i\omega t}, \quad (2.17)$$

$$E_z = E_0 J_n(k_r r) \cos(n\theta) \cos(k_z z) e^{-i\omega t}, \quad (2.18)$$

$$B_r = iE_0 \frac{n\omega}{c^2 k_r^2 r} J_n(k_r r) \sin(n\theta) \cos(k_z z) e^{-i\omega t}, \quad (2.19)$$

$$B_\theta = iE_0 \frac{\omega}{c^2 k_r r} J'_n(k_r r) \cos(n\theta) \cos(k_z z) e^{-i\omega t}, \quad (2.20)$$

$$B_z = 0. \quad (2.21)$$

It is immediately apparent that the longitudinal magnetic field vanishes.  $J_n(x)$  is a Bessel function of order  $n$  and  $J'_n(x)$  is the derivative. Due to the boundary conditions that  $B_\theta$  and  $E_r$  have to vanish on the curved wall of the cavity, the wave number  $k_r$  is constrained to:

$$k_r = \frac{p_{nm}}{R} \quad (2.22)$$

with  $p_{nm}$  being the  $m$ th zero of the  $n$ th-order Bessel function and  $R$  being the radius of the cylinder. The constraint for  $k_z$  can be derived by the boundary conditions that need  $E_z = B_r = B_\theta = 0$  to be on the flat ends of the cavity, with  $z = 0$  and  $z = L$  defining both ends. This leads to  $\sin(k_z L) = 0$  and therefore:

$$k_z = \frac{l\pi}{L} \quad (2.23)$$

with  $l$  being the integer longitudinal mode number. Now it is possible to obtain the dispersion relation similarly as in equation 2.15 by substituting the electric field (2.16 - 2.18) into the wave equation 2.11:

$$k_r^2 + k_z^2 = \frac{\omega^2}{c^2} \quad (2.24)$$

Sets of solutions of this form are referred to as *TM modes*. A specific mode is commonly described as  $TE_{nml}$  with the indices  $n$  (azimuthal),  $m$  (radial), and  $l$  (longitudinal). The frequency  $\omega_{nml}$  of this mode is given by:

$$\omega_{nml} = c\sqrt{k_r^2 + k_z^2} = c\sqrt{\frac{p_{nm}^2}{R^2} + \frac{l^2\pi^2}{L^2}}. \quad (2.25)$$

The fundamental mode for creating an accelerating field is  $\text{TM}_{010}$ . The fields for this mode are:

$$E_r = 0, \quad (2.26)$$

$$E_\theta = 0, \quad (2.27)$$

$$E_z = E_0 J_0 \left( p_{01} \frac{r}{R} \right) e^{-i\omega t}, \quad (2.28)$$

$$B_r = 0, \quad (2.29)$$

$$B_\theta = -i \frac{E_0}{c} J_1 \left( p_{01} \frac{r}{R} \right) e^{-i\omega t}, \quad (2.30)$$

$$B_z = 0. \quad (2.31)$$

The frequency  $\omega_{010}$  is only dependent on the radius  $R$ :

$$\omega_{010} = p_{01} \frac{c}{R}. \quad (2.32)$$

While not being relevant for the frequency of the fundamental mode, the length of the cavity is important for the actual acceleration of particles. Since the fields in the cavity are oscillating, the time the particle needs to pass the cavity should be half of the RF period. Otherwise, the particle will either not experience the full positive field or will be de-accelerated by the polarity change.

In the ideal case, the total energy in the cavity is constant over time, but oscillates between the electric and magnetic field. Since the conducting walls of a real cavity are not ideal, some energy is dissipating on the walls. This rate of dissipation is quantified by the so-called quality factor  $Q$ . For  $Q \gg 1$ ,  $Q$  is the number of oscillations over which the energy falls by a factor  $e^{-\pi}$ . The dissipated power  $P_d$  is defined as:

$$P_d = \frac{\omega}{Q} E_{\text{total}}, \quad (2.33)$$

with  $E_{\text{total}}$  being the stored energy by the electric and magnetic fields. For a mode with an accelerating voltage of  $V_0$ , the so-called shunt impedance  $R_S$  is defined as:

$$R_S = \frac{V_0^2}{P_d}. \quad (2.34)$$

$R_S$  and  $Q$  are important quantities for describing the properties of a cavity [1, p. 43-57]

## 2.2 Hamiltonian Formalism

The previous section introduced static two-dimensional magnetic fields (or simply magnets) and oscillating electric- and magnetic fields in a RF cavity. Now the goal is to find a way to describe a combination of magnets, cavities and drift spaces (regions without magnetic or electric fields) forming a beam line. For a circular accelerator such as KARA this usually breaks down to defining smaller periodic elements. Particles moving through these periodic elements experience influences based on the external properties of the environment – like strength of a magnetic field – but also based on the internal property of the particle itself – such as momentum or angle. This is usually referred to as the beam dynamics of the accelerator. The Hamiltonian formalism provides a convenient way to describe the beam dynamics, as will be described in this section.

### 2.2.1 Straight Beam Line

In general, Hamilton's equations are expressed as:

$$\frac{dx_i}{dt} = \frac{\partial H}{\partial p_i} \quad (2.35)$$

$$\frac{dp_i}{dt} = -\frac{\partial H}{\partial x_i} \quad (2.36)$$

with  $x_i$  being the coordinates of the particle in  $i$  dimensions,  $p_i$  being the components of the momentum and the Hamiltonian  $H$ . For charged particles influenced by electromagnetic fields a possible Hamiltonian is:

$$H = \frac{(\mathbf{p} - q\mathbf{A})^2}{2m} + q\phi \quad (2.37)$$

where  $\phi$  is the scalar potential and  $\mathbf{A}$  the vector potential. These generalised potentials are related to the electric and magnetic fields:

$$E = -\nabla\phi - \frac{\partial\mathbf{A}}{\partial t} \quad (2.38)$$

$$B = \nabla \times \mathbf{A}. \quad (2.39)$$

The canonical momentum  $p$  is:

$$\mathbf{p} = m\mathbf{v} + q\mathbf{A}. \quad (2.40)$$

Since the electrons in KARA are moving with relativistic velocity, a Hamiltonian for a relativistic particle need to be found. Energy and momentum in the presence of an electromagnetic field can be expressed by:

$$E = \gamma mc^2 + q\phi, \quad (2.41)$$

$$\mathbf{p} = \beta\gamma mc + q\mathbf{A}, \quad (2.42)$$

with the usual definitions for  $\beta = v/c$  and  $\gamma = \frac{1}{\sqrt{1-\beta^2}}$ . Therefore the total energy and the canonical momentum are related in the presence of an electromagnetic field by:

$$(E - q\phi)^2 = (\mathbf{p} - q\mathbf{A})^2 c^2 + m^2 c^4. \quad (2.43)$$

Since the Hamiltonian can be defined by the total energy, a possible solution for the Hamiltonian for a relativistic charged particle is:

$$H = c\sqrt{(p_x - qA_x)^2 + (p_y - qA_y)^2 + (p_z - qA_z)^2 + m^2 c^2} + q\phi. \quad (2.44)$$

Up until now, the independent variable of Hamiltonian is the time  $t$ . The advantage of using the Hamiltonian formalism is that the Hamiltonian can be transformed to a different independent variable. For a beam line it is much more useful to define the position  $z$  along the beam line as the independent variable and to transform the variables like this:

$$H \Rightarrow -p_z \quad (2.45)$$

$$z \Rightarrow t \quad (2.46)$$

$$p_z \Rightarrow -H \quad (2.47)$$

$$t \Rightarrow z \quad (2.48)$$

defining a new Hamiltonian  $H_1$  as:

$$H_1 = -p_z = -\sqrt{\frac{(E - q\phi)^2}{c^2} - (p_x - qA_x)^2 - (p_y - qA_y)^2 - m^2c^2} - qA_z. \quad (2.49)$$

Solving the resulting new equations of motion will lead to expressions in coordinates of  $(x, p_x)$ ,  $(y, p_y)$  and  $(t, -E)$  in terms of the independent variable  $z$ . As long as the electric or magnetic fields are independent of the time  $t$ , the total energy of the particle will be constant, allowing solutions for the transverse variables  $(x, p_x)$  and  $(y, p_y)$  to be obtained knowing only the total energy and without needing to know the time  $t$  at which the particle is at any point along the beam line.

The next step is to introduce dynamic variables, since the relevant dynamics will happen between individual particles on a much smaller scale than the overall length of the beam line. This can be done by introducing a reference momentum  $P_0$  which will be the momentum an ideal particle should have from the design of the beam line. This will lead to describing all particles with a relative position and momenta to the so-called reference particle:

$$P_0 = \beta_0 \gamma_0 mc \quad (2.50)$$

with  $\beta_0$  being the speed of the reference particle. The longitudinal position of the reference particle will therefore be  $z^r = 0$  and particles arriving at an earlier time will have a longitudinal position  $z^r > 0$ . The longitudinal momentum is:

$$p_z^r = \frac{E}{cP_0} - \frac{1}{\beta_0} \quad (2.51)$$

again with the reference particle at  $p_z^r = 0$ . Particles with a higher momentum will be at  $p_z^r > 0$ . This is conventionally called the energy deviation of the particles  $\delta$ . Since from now on only these new dynamical variables will be used we redefine these variables,  $x$  and  $y$  will be the dynamic positions relative to the reference particle with the momenta  $p_x$  and  $p_y$ :

$$p_x = \frac{\beta_x \gamma mc + qA_x}{P_0}, \quad (2.52)$$

$$p_y = \frac{\beta_y \gamma mc + qA_y}{P_0}. \quad (2.53)$$

$s$  will now be the distance along the beam line and  $z$  the coordinate, which describes the longitudinal distance to  $s$ , and  $\delta$  the energy deviation:

$$z = \frac{s}{\beta_0} - ct, \quad (2.54)$$

$$\delta = \frac{E}{cP_0} - \frac{1}{\beta_0}. \quad (2.55)$$

This leads finally to the Hamiltonian of a charged particle expressed in dynamical variables relative to a reference particle with a reference momentum  $P_0$ :

$$H = \frac{\delta}{\beta_0} - \sqrt{\left(\delta + \frac{1}{\beta_0 - \frac{q\phi}{cP_0}}\right)^2 - (p_x - a_x)^2 - (p_y - a_y)^2 - \frac{1}{\beta_0^2 \gamma_0^2}} - a_z, \quad (2.56)$$

using the scaled vector potential  $\mathbf{a} = \frac{q}{P_0} \mathbf{A}$  [1, p. 61-71].

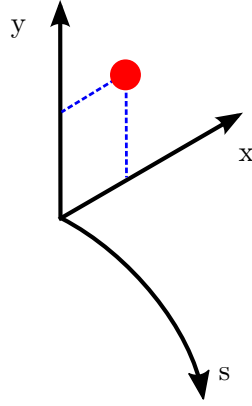


Figure 2.3: Curved coordinate system used for curved parts of the beam line.  $s$  follows the path of an ideal particle through the curved sections and  $x$  and  $y$  represent the displacement in horizontal and vertical direction in reference to this ideal particle.

### 2.2.2 Curved Beam Line

Since KARA is a circular accelerator it cannot be described as a combination of straight beam lines. To force charged particles on a curved path static dipole fields are used. In the previous section the particle was defined by the position  $s$  along the beam line. For the proper description in a dipole field, the  $s$  coordinate also has to follow the curved path, while  $x$  and  $y$  will still be the dynamic variables but also along the curved path. The curvature will only happen in the  $x$ - $z$  plane. The idea is again to transform the variables from Cartesian coordinates  $(X, Y, Z)$  to curved coordinates  $(x, y, s)$  as shown in Figure 2.3. The relationship can be described with:

$$X = (x + \rho) \cos\left(\frac{s}{\rho}\right) - \rho, \quad (2.57)$$

$$Y = y, \quad (2.58)$$

$$Z = (x + \rho) \sin\left(\frac{s}{\rho}\right) - \rho. \quad (2.59)$$

The transformed momenta will be:

$$p_x = P_X \cos\left(\frac{s}{\rho}\right) + P_Z \sin\left(\frac{s}{\rho}\right), \quad (2.60)$$

$$p_y = P_Y, \quad (2.61)$$

$$p_s = P_Z \left(1 + \frac{x}{\rho}\right) \cos\left(\frac{s}{\rho}\right) - P_X \left(1 + \frac{x}{\rho}\right) \sin\left(\frac{s}{\rho}\right). \quad (2.62)$$

Also the vector potential  $A$  has to be transformed in the same way:

$$A_x = A_X \cos\left(\frac{s}{\rho}\right) - A_Z \sin\left(\frac{s}{\rho}\right), \quad (2.63)$$

$$A_y = A_Y, \quad (2.64)$$

$$A_s = A_Z \cos\left(\frac{s}{\rho}\right) + A_X \sin\left(\frac{s}{\rho}\right). \quad (2.65)$$

This leads to a Hamiltonian in the curved coordinate system. At this point the same transformations as in the straight beam line case can be carried out: Changing the independent

variable from  $t$  to  $s$ , scaling by the reference momentum  $P_0$  and expressing the longitudinal variables in terms of energy deviation. This finally leads to the new Hamiltonian:

$$H = \frac{\delta}{\beta_0} - (1 + hx) \sqrt{\left( \delta + \frac{1}{\beta_0 - \frac{q\phi}{cP_0}} \right)^2 - (p_x - a_x)^2 - (p_y - a_y)^2 - \frac{1}{\beta_0^2 \gamma_0^2}} - (1 + hx)a_s, \quad (2.66)$$

with  $h = 1/\rho$  defined as the curvature, which is very similar to the result obtained for the straight beam line. For  $h \rightarrow 0$  it will be identical. The overall reference trajectory can now be fully described as a combination of the straight and curved Hamiltonians [1, p. 72-75].

### 2.2.3 Liouville's Theorem

To transform the properties of a particle from one point  $s_0$  to another  $s_1$ , a transfer map  $\vec{M}$  can be defined such as:

$$\vec{x}(s_1) = \vec{M}(\vec{x}(s_0)), \quad (2.67)$$

with  $\vec{x} = (x, p_x, y, p_y, z, \delta)$  describing the full six components of the particle at position  $s$ . The transfer map is found by solving Hamilton's equations. An important property of transfer maps following Hamilton's equations is that such transfer maps are *symplectic* and a combination of symplectic transformations is also symplectic. This means individual transfer maps can be constructed for certain elements, such as magnets, and the multiplication of these transfer maps will result in a new combined transfer maps. For symplectic transformations some quantities are conserved. In this case the conserved quantity is the particle density in the six-dimensional phase space of  $\vec{x}$ . This conservation of particles obeying the Hamilton's equations is also known as Liouville's theorem and can be written as:

$$\frac{d\rho}{dt} = \frac{\partial \rho}{\partial t} \sum_{i=1}^{2n} \frac{dx_i}{dt} \frac{\partial \rho}{\partial x_i} = 0. \quad (2.68)$$

This has important consequences for the beam dynamics and particles travelling along the beam line. If the phase space is conserved, particles which are focused will see an increase in divergence and vice versa. For the first order of linear transfer maps the conserved quantities are called emittances [1, p. 76-80].

## 2.3 Beam Dynamics

With the electric and magnetic fields and the Hamilton formalism, the beam dynamics can now be described starting with linear approximation of common elements and resulting linear optics, followed by properties of oscillating charged particles.

### 2.3.1 Common Components

Using the Hamiltonians defined in equations 2.56 and 2.56 common components along an accelerator beam line can be described with transfer maps. For a first order linear description, the Hamiltonian can be expanded to second order in the dynamical variables.

For a drift space – a region without electric or magnetic fields – with curvature  $h = 0$ ,  $\phi = 0$  and  $\mathbf{A} = 0$  the second-order Hamiltonian is:

$$H_2^{\text{drift}} = \frac{p_x^2}{2} + \frac{p_y^2}{2} + \frac{\delta^2}{2\beta_0^2\gamma_0^2}. \quad (2.69)$$

The transfer map can be found by solving Hamilton's equations using  $H_2^{\text{drift}}$ . For the linear consideration it is possible to write the transfer map  $\vec{M}$  in matrix form  $\vec{x}_1 = R_{\text{drift}}\vec{x}_0$  and  $s_1 = s_0 + L$ :

$$R_{\text{drift}} = \begin{pmatrix} 1 & L & 0 & 0 & 0 & 0 \\ 0 & 1 & 0 & 0 & 0 & 0 \\ 0 & 0 & 1 & L & 0 & 0 \\ 0 & 0 & 0 & 1 & 0 & 0 \\ 0 & 0 & 0 & 0 & 1 & \frac{L}{\beta_0^2\gamma_0^2} \\ 0 & 0 & 0 & 0 & 0 & 1 \end{pmatrix}, \quad (2.70)$$

with  $L$  being the length of the drift section.

A quadrupole has zero field for a particle exactly in the center with  $x = 0$  and  $y = 0$ . For this particular case the quadrupole would effectively be another drift section. But for particles not on the reference path they will experience the magnetic field (scaled by  $q/P_0$ ) given by:

$$\mathbf{b} = (k_1 y, k_1 x, 0), \quad \text{derived from} \quad \mathbf{a} = \left(0, 0, -\frac{k_1}{2}(x^2 - y^2)\right), \quad (2.71)$$

with  $k_1 = \frac{q}{P_0} \frac{\partial B}{\partial x}$  being the normalised field strength. This leads to the Hamiltonian  $H_2^{\text{quad}}$ :

$$H_2^{\text{quad}} = \frac{p_x^2}{2} + \frac{p_y^2}{2} + \frac{\delta^2}{2\beta_0^2\gamma_0^2} + \frac{k_1}{2}(x^2 - y^2). \quad (2.72)$$

Solving the equations of motion with  $H_2^{\text{quad}}$  will result in the transfer matrix  $R_{\text{quad}}$  with  $L$  being the distance the particles experience the quadrupole field:

$$R_{\text{quad}} = \begin{pmatrix} \cos(\omega L) & \frac{1}{\omega} \sin(\omega L) & 0 & 0 & 0 & 0 \\ -\omega \sin(\omega L) & \cos(\omega L) & 0 & 0 & 0 & 0 \\ 0 & 0 & \cosh(\omega L) & \frac{1}{\omega} \sinh(\omega L) & 0 & 0 \\ 0 & 0 & \omega \sinh(\omega L) & \cosh(\omega L) & 0 & 0 \\ 0 & 0 & 0 & 0 & 1 & \frac{L}{\beta_0^2\gamma_0^2} \\ 0 & 0 & 0 & 0 & 0 & 1 \end{pmatrix}, \quad (2.73)$$

with  $\omega = \sqrt{k_1}$ . With  $k_1 > 0$ , the particle in the horizontal plane will be focused, whereas the particle in the vertical plane will be defocused. For  $k_1 < 0$  the effect is reversed. This means that one quadrupole cannot focus both planes at the same time. In practice, if a quadrupole has a focusing or defocusing effect in a specific plane it can be switched by changing the polarity. Using the thin lens approximation, which ignores additional contributions due to the length of the quadrupole:

$$L \rightarrow 0, \quad (2.74)$$

$$k_1 L \rightarrow \frac{1}{f}, \quad (2.75)$$

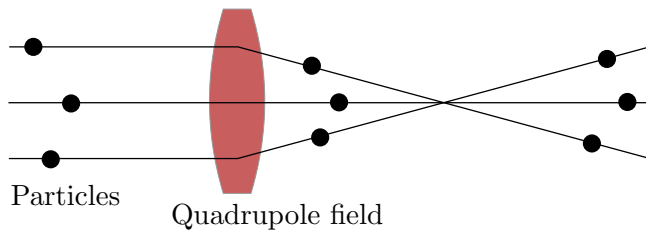


Figure 2.4: Quadrupole magnet working principle. Particles entering a horizontally focusing the quadrupole with a horizontal off-axis will be focused back towards the center with an effective focusing length  $f$ . At the same time this particle is being defocused with the focusing length  $f$  in the vertical plane, which is not shown here.

with  $f$  being constant, the transfer matrix for a horizontally focusing quadrupole  $R_{\text{QF}}$  can be written as:

$$R_{\text{QF}} = \begin{pmatrix} 1 & 0 & 0 & 0 & 0 & 0 \\ -\frac{1}{f} & 1 & 0 & 0 & 0 & 0 \\ 0 & 0 & 1 & 0 & 0 & 0 \\ 0 & 0 & \frac{1}{f} & 1 & 0 & 0 \\ 0 & 0 & 0 & 0 & 1 & 0 \\ 0 & 0 & 0 & 0 & 0 & 1 \end{pmatrix}. \quad (2.76)$$

$f$  can therefore be interpreted as the focusing strength of the quadrupole focusing the particle onto the reference path as shown in Figure 2.4. As previously discussed, the procedure to derive transfer maps allows to be combined multiple transfer maps, while maintaining the conserved quantities. To construct a beam line consisting of a horizontally focusing quadrupoles, drift sections and a horizontally defocusing quadrupole the full transfer matrix would be:

$$R = R_{\text{drift}} R_{\text{QD}} R_{\text{drift}} R_{\text{QF}}. \quad (2.77)$$

The horizontally defocusing quadrupole is required to focus the beam in the vertical plane. Since so far the motion is not coupled between the planes,  $R$  can be expressed as:

$$R = \begin{pmatrix} R_x & 0 & 0 \\ 0 & R_y & 0 \\ 0 & 0 & R_z \end{pmatrix}, \quad (2.78)$$

with  $R_x$  expressed only in  $L$  and  $f$ :

$$R_x = \begin{pmatrix} 1 - \frac{L}{f} \left(1 + \frac{L}{f}\right) & \frac{L}{f} (2f + L) \\ -\frac{L^2}{f} & 1 + \frac{L}{f} \end{pmatrix}. \quad (2.79)$$

Such a configuration of a beam line is called a FODO cell. With proper selection of  $f$ ,  $L$ , and the amount of FODO cells, a stable and periodic particle trajectory can be found. Although this is probably one of the most basic configurations possible, it is widely used in modern accelerators. As shown in Chapter 3, the pre-accelerator of KARA has a FODO lattice. The drift sections (O) are in practice not pure drift sections, but are typically filled with other components, most importantly dipole magnets or RF cavities.

As discussed previously, the Hamiltonian for a dipole field has to include the curved nature of the trajectory and is given by equation 2.66. The  $B$  field of a dipole is in the vertical direction and constant:

$$\mathbf{B}^{\text{dipole}} = (0, B_0, 0). \quad (2.80)$$

A scaled vector potential  $\mathbf{a}$  can be derived with  $a_x = a_y = 0$  like this:

$$\mathbf{a} = \left( 0, 0, -k_0 x + \frac{k_0 h x^2}{2(1 + hx)} \right), \quad (2.81)$$

with the curvature  $h$  and the normalised field strength  $k_0 = q/P_0 B_0$ . Then, the approximated Hamiltonian of second order can be derived to be:

$$H_2^{\text{dipole}} = \frac{p_x^2}{2} + \frac{p_y^2}{2} + \frac{\delta^2}{2\beta_0^2 \gamma_0^2} + \left( k_0 - h \left( 1 + \frac{\delta}{\beta_0} \right) \right) x + \frac{k_0 h x^2}{2}. \quad (2.82)$$

For a particle to stay on the reference trajectory the curvature should be:

$$h = k_0. \quad (2.83)$$

For a particle with the reference momentum and with  $\rho = \frac{1}{h}$  this leads to:

$$B\rho = \frac{P_0}{q}. \quad (2.84)$$

The product of the magnetic field  $B$  and the curvature  $h$  therefore only depends on the momentum and the charge, with the latter being constant at KARA. This is also referred to as the *beam rigidity*. A matrix representation for the dipole can be derived in the same way as for the quadrupole and drift sections, but the individual terms become complex due to the curved reference. One important characteristic is already apparent in the Hamiltonian in equation 2.82: Particles with non-zero energy deviation  $\delta$  will deviate from the reference trajectory while travelling through the dipole field depending on the energy deviation and the magnetic field strength. This effect is referred to as *dispersion* and couples longitudinal and horizontal motion. Particles with too large an energy deviation will therefore be lost along the curved trajectory due to geometrical limits of the beam line. Energy deviation will be corrected inside the RF cavities that are used in circular accelerators. Section 2.1.2 already discussed the fields inside a RF cavity using the TM<sub>010</sub> mode. A Hamiltonian  $H^{\text{RF}}$  can be derived which will have an explicit dependence on the variable  $s$  due to the time dependence field inside the RF cavity. An approximation can be made by integrating the Hamiltonian over the length of the cavity  $L$  to find an averaged version  $\langle H \rangle$ :

$$\langle H \rangle = \frac{1}{L} \int_{-L/2}^{+L/2} H^{\text{RF}} ds. \quad (2.85)$$

This averaged Hamiltonian can now again be expanded to second order resulting in:

$$H_2^{\text{RF}} = \frac{p_x^2}{2} + \frac{p_y^2}{2} + \frac{\delta^2}{2\beta_0^2 \gamma_0^2} + \frac{\alpha}{4\pi} \cos(\phi_0) k^2 (x^2 + y^2) - \frac{\alpha}{\pi} \sin(\phi_0) k z + \frac{\alpha}{2\pi} \cos(\phi_0) k^2 z^2, \quad (2.86)$$

with  $k$  being a constant related to the cavity radius.  $\alpha$  is defined as:

$$\alpha = \frac{qV_0}{P_0 c}, \quad (2.87)$$

with the cavity voltage  $V_0$ , which is the total voltage the particle experiences by passing the changing electric field in the cavity. The fourth term in the Hamiltonian represents a focusing effect in  $x$  and  $y$  due to the azimuthal magnetic fields in the  $TM_{010}$  mode. The fifth term leads to the change in energy deviation  $\delta$ , which is independent on the particle coordinates, resulting in the same change for every particle in the beam. The average change in energy deviation can be approximated to:

$$\Delta\delta \approx \alpha \sin \phi_0, \quad (2.88)$$

and is therefore dependent on the cavity voltage  $V_0$  and phase of the RF  $\phi_0$  [1, p. 83-115].

### 2.3.2 Linear Optics

With the previously discussed components it is now possible to construct more complex beam lines in a similar way as with the FODO lattice. At this point it will be useful to introduce parameters which will represent the combined beam line. For this, for example the horizontal transfer matrix for the FODO lattice  $R_x$  (eq. 2.79) can be expressed as:

$$R_x = I_2 \cos \mu_x + S_2 A_x \sin \mu_x, \quad S_2 = \begin{pmatrix} 0 & 1 \\ -1 & 0 \end{pmatrix} \quad (2.89)$$

with  $I_2$  being the identity matrix,  $S_2$  the antisymmetric matrix and  $\mu_x$  will be the phase advance.  $A_x$  can then be defined as:

$$A_x = \begin{pmatrix} \gamma_x & \alpha_x \\ \alpha_x & \beta_x \end{pmatrix}. \quad (2.90)$$

Since the transfer matrix is symplectic,  $A_x$  has only three independent parameters.  $\alpha_x$ ,  $\beta_x$  and  $\gamma_x$  are known as the *Courant-Snyder parameters* [3] or the *Twiss parameters*.  $R_x$  can now be fully expressed with the Courant-Snyder parameters and the phase advance:

$$R_x = \begin{pmatrix} \cos \mu_x + \alpha_x \sin \mu_x & \beta_x \sin \mu_x \\ -\gamma_x \sin \mu_x & \cos \mu_x - \alpha_x \sin \mu_x \end{pmatrix}. \quad (2.91)$$

With this, the Courant-Snyder parameters and the phase advance can be determined for every element along a beam line of multiple components. For a circular accelerator made of multiple periodic cells the Courant-Snyder parameters are defined by one periodic cell. In the phase space  $(x, p_x)$ , the particle will be on an ellipse after each periodic cell. The property of the ellipse can be expressed with the Courant-Snyder parameters as shown in Figure 2.5. Individual elements will change the form of the ellipse, but the area of the ellipse is conserved throughout the beam line. Liouville's theorem (eq. 2.68) already states that the density of the phase space is conserved as long as the dynamics are described using the time-independent Hamilton's equations. While this is true for the full phase space, the Courant-Snyder parameters will provide conserved quantities for every degree of motion for only small energy deviations  $\delta$ . In fact this holds true also for particle distributions in periodic beam lines. For a particle distribution in  $\langle x \rangle$  and  $\langle p_x \rangle$ , the so-called RMS or geometrical emittance  $\epsilon_x$  is given by:

$$\epsilon_x = \sqrt{\langle x^2 \rangle \langle p_x^2 \rangle - \langle xp_x \rangle^2}. \quad (2.92)$$

If the reference momentum  $P_0$  itself is changed – for example due to a significant change in energy – the emittance  $\epsilon_x$  is not conserved. Instead the so-called normalised emittance can be defined using the relativistic factors  $\beta_0$  and  $\gamma_0$ :

$$\epsilon_x^{\text{norm}} = \beta_0 \gamma_0 \epsilon_x. \quad (2.93)$$

The normalised emittance is also conserved for changes in reference momentum. Increasing the energy will result in the geometric emittance being reduced. This is also referred to as *adiabatic damping*. For circular accelerators the reference momentum is usually constant for most beam operations. The change in reference momentum either happens during the pre-acceleration steps or during the so-called energy ramp, which in the case of KARA takes a couple of minutes compared to beam operation in the range of 20 – 24 hours.

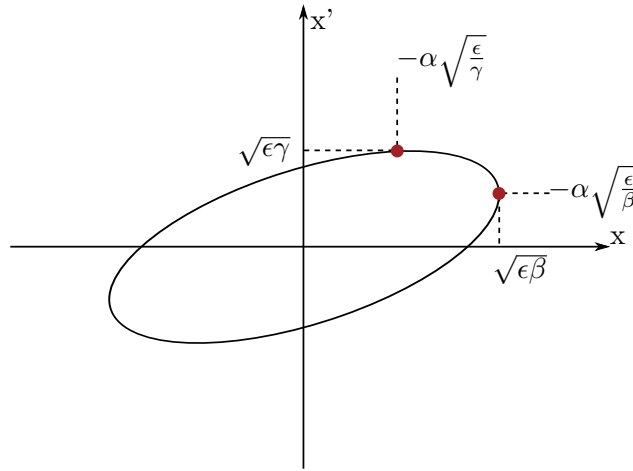


Figure 2.5: Phase ellipse. Displayed is the phase ellipse defined by the Courant-Snyder parameters. While the ellipse is transformed the overall area is conserved as long as the dynamics are described using Hamilton’s equations.

The Courant-Snyder parameter  $\beta_x$  is often also referred to as the *beta function*. Due to the alternate focusing and defocusing of the quadrupoles the particles perform horizontal and vertical oscillation – referred to as betatron oscillation. The  $\beta$ -function describes the maximum local amplitude a single particle or a particle distribution will have along the beam line. Figure 2.6 illustrates the  $\beta$ -function as the envelope. The actual horizontal beam size  $\sigma_x$  at the position  $s$  along the beam line can then be expressed using the  $\beta$ -function and the geometrical emittance [1, p. 127-147]:

$$\sigma_x(s) = \sqrt{\epsilon_x \beta_x(s)}. \quad (2.94)$$

### 2.3.3 Synchrotron Motion

Until now the general assumption was mostly that the motion in each plane can be described independently of each other. But the Hamiltonians for the dipole and RF cavity already indicated coupling between the planes. For a circular accelerator the coupling between the horizontal and longitudinal plane is significant. The *dispersion* was already mentioned in context of the dipole: Particles with an energy deviation will travel on different trajectories through the dipole field. This leads to an overall different circumference

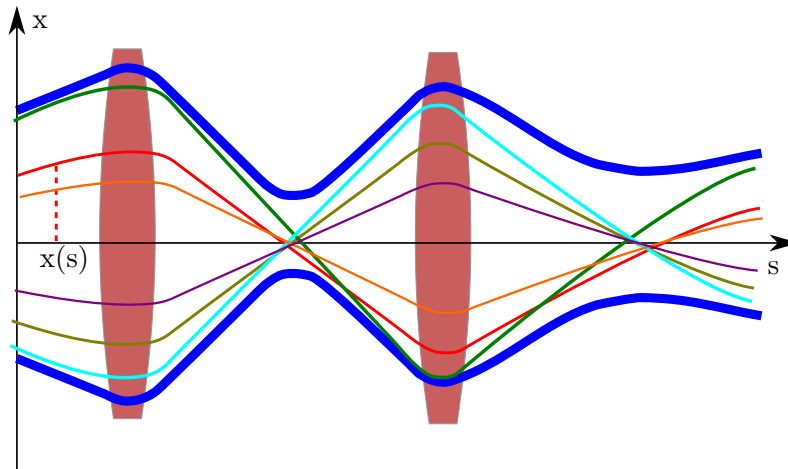


Figure 2.6: The  $\beta$ -function as the envelope of possible particle trajectories. While individual particles will take different paths and amplitudes while travelling through a periodic section of a beam line, the  $\beta$ -function defines the envelope of the maximum trajectory for every point along the beam line. This also defines the overall beam size. Adapted from [2].

$C$  the particles travel along, depending on the amount of energy deviation compared to the reference path of length  $C_0$ :

$$C = C_0 + \int_0^{C_0} \frac{x}{\rho} ds. \quad (2.95)$$

If  $x$  only depends on energy deviation and dispersion, the *momentum compaction factor*  $\alpha_c$  can be defined as the relative change in path length compared to the reference path:

$$\alpha_c = \frac{1}{C_0} \int_0^{C_0} \frac{D_x}{\rho} ds, \quad (2.96)$$

with  $D_x$  being the dispersion. Particles travelling along a different circumference will also take more or less time to perform one full revolution. The relation between momentum and time of flight is referred to as the *phase slip factor*  $\eta_p$  which can be expressed by the momentum compaction factor as:

$$\eta_p = \alpha_c - \frac{1}{\gamma_0^2}. \quad (2.97)$$

Varying travel paths also lead to varying arrival times at the RF cavities, as shown in Figure 2.7, resulting in the particles experiencing more cavity voltage for a smaller circumference and less voltage for a larger circumference. This changes the energy deviation towards  $\delta = 0$ . This is also called *phase-focusing*. Similar to the betatron oscillations for vertical and horizontal motion, this forces the particles to perform longitudinal oscillation around the energy of the reference particle, the so-called synchrotron oscillation. The amplitude of the oscillation will also be small compared to the overall RF wavelength, since stable oscillation will only be possible for a phase  $\phi_s$  with  $\frac{\pi}{2} < \phi_s < \pi$ . Using the phase slip factor a Hamiltonian can be found describing the synchrotron motion:

$$H^s = \frac{qV_{\text{rf}}}{\omega_{\text{rf}}P_0C_0} \left( \sin(\phi_s) \frac{\omega_{\text{rf}}z}{c} - \cos \left( \phi_s - \frac{\omega_{\text{rf}}z}{c} \right) \right) - \frac{1}{2} \eta_p \delta^2. \quad (2.98)$$

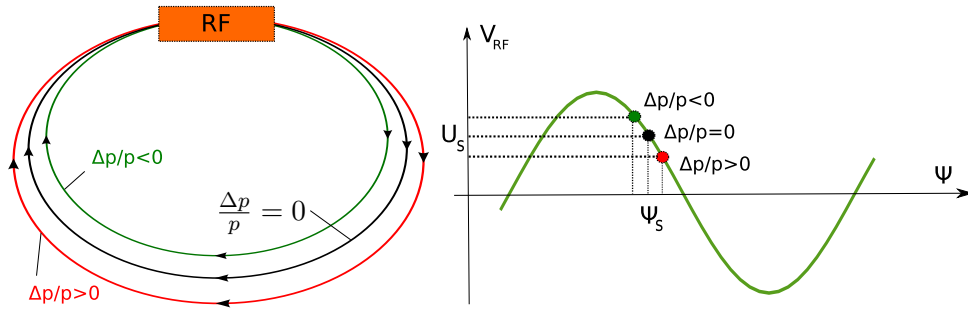


Figure 2.7: Principle of phase focusing of an RF cavity. The left side shows the circular representation with particles taking longer (red) or shorter (green) travel paths compared to the particle with zero momentum deviation. Above transition energy, this will lead to particles with less momentum arriving earlier. These particles will see a higher average field inside the cavity, as shown on the right plot showing the field over the phase of the cavity. Particles with more momentum will arrive later and gain less voltage. This will automatically focus particles with momentum deviation towards particles with zero deviation and introduces longitudinal oscillations. Adapted from [2].

Looking at the longitudinal phase space  $(z, \delta)$  the Hamiltonian  $H^s$  represents motion following the contours, as shown in Figure 2.8. Closed contours represent stable oscillation whereas open contours will lead to particles being lost. The contour which crosses at one point is called the *separatrix*, since it separates stable and unstable regions in the phase plot. The stable region is defined as the *RF bucket*. The overall number of RF buckets in a circular accelerator is defined by the *harmonic number*  $h$  using the revolution frequency  $\omega_{\text{rev}}$ :

$$h = \frac{\omega_{\text{rf}}}{\omega_{\text{rev}}}. \quad (2.99)$$

The maximum energy deviation which will still lead to stable synchrotron oscillation is referred to as the *energy acceptance* of the accelerator.

### 2.3.4 Tunes and Resonances

Particles travelling along a periodic beam line perform horizontal, vertical and longitudinal oscillations. The main contribution to transverse (betatron) oscillation are the focusing and defocusing of the quadrupole magnets, whereas the reason for longitudinal (synchrotron) oscillations are energy deviations and phase focusing in the RF cavities. The phase advance  $\mu$  describes the fraction of the full oscillation cycle the particles experience while passing an element. Adding up every phase advance for one revolution will result in the horizontal betatron tune  $\nu_x$  and vertical betatron tune  $\nu_y$ :

$$\nu_x = \frac{1}{2\pi} \oint \frac{ds}{\beta_x(s)}. \quad (2.100)$$

The synchrotron tune  $\nu_s$  is defined by:

$$\nu_s = \frac{1}{2\pi} \sqrt{-\frac{qV_{\text{rf}} \omega_{\text{rf}} C_0}{cP_0} \eta_p \cos \phi_s}. \quad (2.101)$$

$\phi_s$  is the *synchronous phase* which is the RF phase the reference particle will experience in the cavities. The particles usually perform multiple full betatron oscillations during one

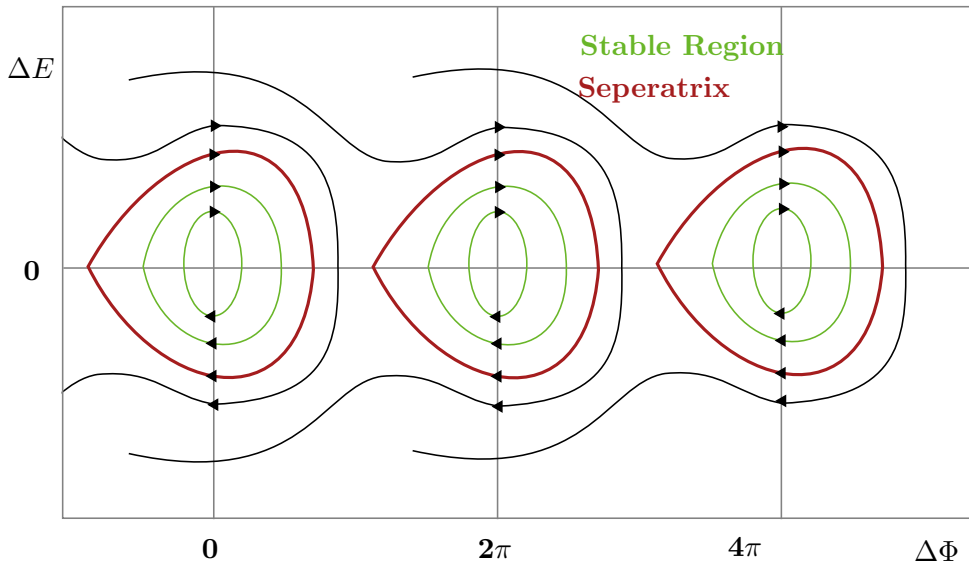


Figure 2.8: Longitudinal phase space showing the seperatrix. The lines show contours of constant  $H$  and correspond to phase space trajectory of the particles. The outer most closed contour is called the seperatrix (red) defining the length of the RF bucket and the distance between two neighboring RF buckets. The height of the bucket represents maximum possible energy deviation for stable particles, the RF acceptance. Adapted from [1].

revolution, while one full synchrotron oscillation typically takes multiple revolutions. The tunes are an important characteristic with which to describe the working point of the accelerator. For the betatron tunes it is important to not perform exactly full integer number of oscillations during one revolution, since this would lead to resonant behaviour adding up on the oscillation amplitude and quickly exceeding the boundaries of the beam line, as illustrated in Figure 2.9. Since the already completed full number of oscillations along one revolution is not relevant in this context, the betatron tunes are often just given as the fractional part of full oscillation. This is also the frequency which can easily be measured at one singular point of the accelerator. The fractional tune can then be determined by dividing the measured betatron frequencies  $\omega_{x,y}$  and the revolution frequency  $\omega_{\text{rev}}$ :

$$\nu_{x,y}^{\text{fractional}} = \frac{\omega_{x,y}}{\omega_{\text{rev}}}. \quad (2.102)$$

For convenience, the notation  $\nu_x$  or  $\nu_y$  assumes the fractional tune. A particular resonance can then be defined as:

$$m_x \nu_x + m_y \nu_y = l, \quad (2.103)$$

where  $m_x$ ,  $m_y$  and  $l$  are all integers. This defines a line in the so-called *tune diagram* with the axes  $\nu_x$  and  $\nu_y$  as shown in Figure 2.10. For a working point  $(\nu_{x0}, \nu_{y0})$   $d$  is the distance from the line, defined by equation 2.103:

$$\frac{|m_x \nu_{x0} + m_y \nu_{y0} - l|}{\sqrt{m_x^2 + m_y^2}} = d. \quad (2.104)$$

For small  $d$  it is:

$$\sin(\pi(m_x \nu_{x0} + m_y \nu_{y0} - l)) \approx \pm \pi d \sqrt{m_x^2 + m_y^2}. \quad (2.105)$$

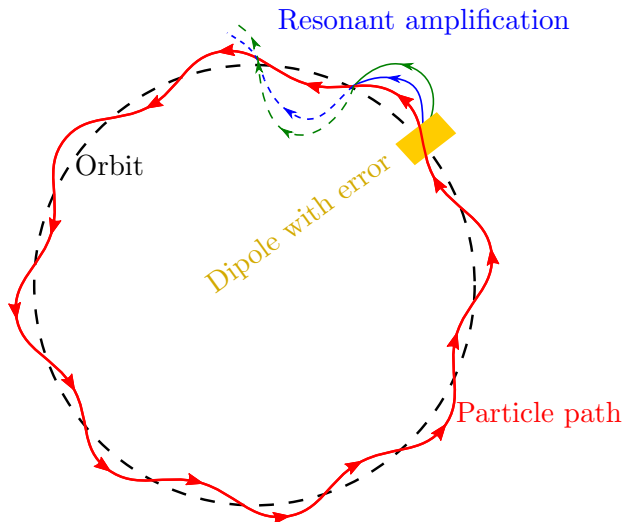


Figure 2.9: Visualization of resonant behaviour. If a particle path (red), as in this case, follows an exact integer number of oscillations for one revolution, small unavoidable errors in the magnetic fields of magnets – in this case a dipole magnet (yellow) will lead to rapid rising amplitude of oscillations for each consecutive revolution, leading to the particle quickly being lost due to the geometrical limits of the vacuum chamber. The fractional tune has to be chosen in such a way that the particle performs many revolutions before it returns to the same trajectory again, therefore mitigating such resonant behaviour. Adapted from [2].

Therefore, the higher the order of the resonance  $|m_x| + |m_y|$ , the closer the working point has to be before the resonance has a significant effect. Particles with a tune close to a resonant line will experience varying resonant behavior depending on the order of resonance. A full-integer or dipole resonance are closed orbit variations represented by varying of the  $\beta$ -function. A half-integer or quadrupole resonance are focusing errors resulting in change in oscillation amplitude. A third-integer or sextupole resonance leads to tune shifts.

### 2.3.5 Chromaticity and Dynamic Aperture

The focusing strength of a quadrupole  $k_1$  as defined in 2.71 depends on the energy of the particle which was assumed thus far to be the reference particle. With the intrinsic variation of energy due to synchrotron motion, this cannot be assumed for a real accelerator. Since the focusing effect of the quadrupole is depending on the energy, this will lead to the phase advance  $\mu$  changing with energy. The *horizontal chromaticity*  $\xi_x$  is then defined as the variation of the horizontal phase advance  $\mu_x$ :

$$\xi_x = \frac{P_0}{2\pi} \frac{d\mu_x}{dP_0}. \quad (2.106)$$

The vertical chromaticity  $\xi_y$  is defined in the same way using the vertical phase advance  $\mu_y$ . The chromaticity will therefore lead to an energy dependent change in tune. The contribution to the chromaticity by the quadrupoles can be written as:

$$\xi_x = P_0 \frac{d\nu_x}{dP_0} = -\frac{1}{4\pi} \oint \beta_x k_1 ds. \quad (2.107)$$

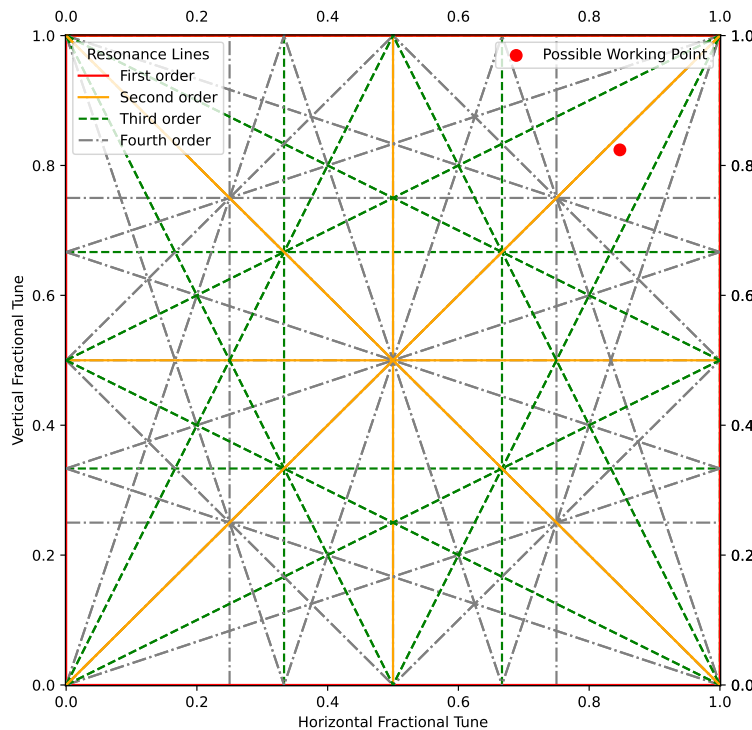


Figure 2.10: Tune Diagram representing the area of possible working points. The vertical tune is plotted over the horizontal tune with the resonance lines following the condition defined in equation 2.103. The order of resonances is shown up to 4th order. Diagonal lines describe coupling resonances. Ideally the working point should be within a safe distance to any resonance line shown here, but some parameter changes during operation might require passing resonances of higher order.

Since  $k_1$  is positive and the  $\beta_x$  is typically large for horizontally focusing quadrupoles, the horizontal chromaticity will be negative and large. One of multiple undesired effects of large chromaticity is that the spread in tune might lead to working points being affected by resonance lines which would otherwise be far enough away, leading to resonant behaviour. Effecting the chromaticity without effecting basic lattice functions like dispersion,  $\beta$ -function and the orbit is possible by using sextupole magnets. A sextupole field is shown in Figure 2.11. Such a field can correct focusing errors due to energy mismatch as illustrated in Figure 2.12. The components of the magnetic field are:

$$b_x = k_2xy, \quad (2.108)$$

$$b_y = \frac{1}{2}k_2(x^2 - y^2), \quad (2.109)$$

$$b_z = 0. \quad (2.110)$$

The sextupole field strength  $k_2$  is defined as:

$$k_2 = \frac{q}{P_0} \frac{\partial^2 B_y}{\partial x^2}. \quad (2.111)$$

The full Hamiltonian for a sextupole  $H^{\text{sext}}$  is:

$$H^{\text{sext}} = \frac{\delta}{\beta_0} - \sqrt{\left(\delta + \frac{1}{\beta_0}\right)^2 - p_x^2 - p_y^2 - \frac{1}{\beta_0^2 \gamma_0^2}} + \frac{1}{6}k_2(x^3 - 3xy^2). \quad (2.112)$$

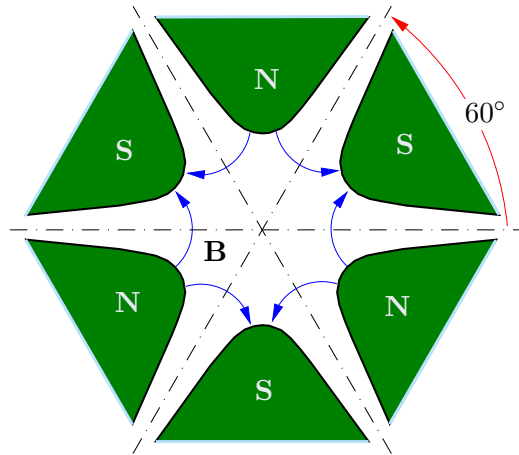


Figure 2.11: Schematic overview of a sextupole cross section. The field of a sextupole introduces non-linear dynamics and cannot be clearly separated into a horizontal and vertical effect such as for the quadrupole fields.

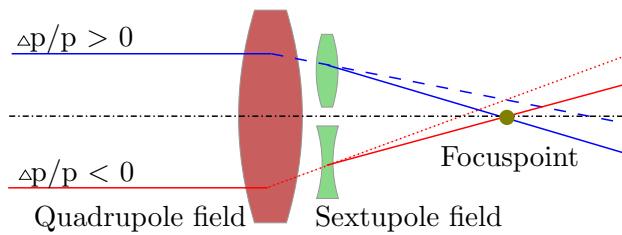


Figure 2.12: Working principle of a sextupole magnet. Sextupole magnets allow for correction of energy deviation in particles and therefore can compensate for the effect that particles with energy deviation will experience a different focusing within quadrupoles. Adapted from [2].

The approach taken in Section 2.3 approximating the Hamiltonian to second order would result in the disappearance of the sextupole contribution and can therefore not be taken here. With the help of sextupole magnets the chromaticity can be controlled and adjusted to values close to zero, but sextupoles also introduce non-linear effects on the beam dynamics and cannot be represented by two dimensional transfer matrices. In general, this and other non-linear effects can be very complex and will introduce limitations to particle motion. This limitation is referred to as the *dynamic aperture*.

### 2.3.6 Synchrotron Radiation

So far, the effect of energy deviation in dipoles leading to dispersion and synchrotron oscillation due to phase focusing in the RF cavities have been discussed, but not the source of energy deviation in the first place. Charged particles will emit electromagnetic radiation while being accelerated. This effect scales with the square of the rate of acceleration and depends on the angle, so, for example, RF cavities contribute only a small fraction to the overall radiation whereas dipole magnets amount for the significant part. The radiation emitted by charged particles moving on a circular path is called *synchrotron radiation*, which can be neglected for non-relativistic speeds. The total radiation power  $P$  for a

relativistic particle with charge  $q$  and constant speed  $\beta_0 c$  following a circular trajectory of radius  $\rho$  is given by:

$$P_{\text{radiation}} = \frac{C_\gamma c \beta_0^4 E_0^4}{2\pi \rho^2}. \quad (2.113)$$

$E_0$  is defined as the energy of a particle with the reference momentum  $P_0$ :

$$P_0 = \frac{\beta_0}{c} E_0 \quad (2.114)$$

and  $C_\gamma$  being a constant related to the mass  $m$  of the particle:

$$C_\gamma = \frac{q^2}{3\epsilon_0 (mc^2)^4}. \quad (2.115)$$

Emitting radiation is non-symplectic leading to a change in emittance due to a change in momentum  $P$ . Assuming that the overall change in emittance is small, the change in vertical emittance for one beam revolution can be written as:

$$\frac{d\epsilon_y}{dt} = -\frac{\epsilon_y}{T_0} \oint \frac{dP}{P_0} \approx -\frac{U_0}{E_0 T_0} \epsilon_y \quad (2.116)$$

with  $T_0$  being the revolution period and  $U_0$  being the energy loss per turn for a particle with reference momentum. This will lead to an exponential damping of the emittance:

$$\epsilon_y(t) = \epsilon_y(0) e^{-2t/\tau_y} \quad (2.117)$$

with the damping time  $\tau_y$  defined by:

$$\tau_y = 2 \frac{E_0}{U_0} T_0. \quad (2.118)$$

The energy loss per turn  $U_0$  can be found by integrating over the radiation power  $P_{\text{radiation}}$ :

$$U_0 = \oint P_{\text{radiation}} \frac{ds}{\beta_0 c} = \frac{C_\gamma c}{2\pi} \beta_0^3 E_0^4 I_2 ds. \quad (2.119)$$

By convention, the *second synchrotron radiation integral*  $I_2$  is defined as:

$$I_2 = \oint \frac{1}{\rho^2} ds. \quad (2.120)$$

For the horizontal emittance the coupling due to dispersion  $D_x$  has to be taken into account. The *fourth synchrotron radiation integral*  $I_4$ , in the case of constant dipole fields, is defined as:

$$I_4 = \oint \frac{D_x}{\rho^3} ds \quad (2.121)$$

The horizontal damping time is then defined as:

$$\tau_x = \frac{2}{j_x} \frac{E_0}{U_0} T_0, \quad (2.122)$$

using the *horizontal damping partition number*  $j_x$ :

$$j_x = 1 - \frac{I_4}{I_2}. \quad (2.123)$$

Without dispersion the partition number is  $j_x = 1$ . Then the horizontal damping time is the same as the vertical damping time, since vertical dispersion can usually be neglected.

With a constant dipole field it can be assumed that  $I_4 \ll I_2$  and the partition number can be approximated to  $j_x \approx 1$ . For the damping of the longitudinal motion the energy deviation  $\delta$  has to be taken into account, which will lead to varying path lengths for full revolutions. Taking this into account the energy loss  $U$  is:

$$U = \oint P_{\text{radiation}} \left( 1 + \frac{D_x}{\rho} \beta_0 \delta \right) \frac{ds}{\beta_0 c}. \quad (2.124)$$

The energy dependent energy loss is then:

$$\frac{dU}{dE} = \beta_0 j_z \frac{U_0}{E_0}, \quad (2.125)$$

with the *longitudinal damping partition number*  $j_z$ :

$$j_z = 2 + \frac{I_4}{I_2}, \quad (2.126)$$

resulting in the longitudinal damping time  $\tau_z$ :

$$\tau_z = \frac{2}{j_z} \frac{E_0}{U_0} T_0. \quad (2.127)$$

Therefore the only difference in the damping times are the damping partition numbers. The *Robinson damping theorem* states:

$$j_x + j_y + j_z = 4. \quad (2.128)$$

Although the balance due to the partition numbers can be shifted by introducing for example dipole gradients, the overall rate of damping is fixed by the beam energy and rate of energy loss due to synchrotron radiation. Until now, the exponential damping of the emittance would lead to an emittance of 0 for  $t \rightarrow \infty$ . This is referred to as the *classical model* for synchrotron radiation. But in reality, the radiation is emitted randomly by discrete photons leading to excitation of synchrotron and betatron oscillation. This *quantum excitation* leads to an equilibrium emittance  $\epsilon_0$  balanced by the classical radiation damping and quantum excitation. The change in emittance can be written as:

$$\frac{d\epsilon_x}{dt} = -\frac{2}{\tau_x} \epsilon_x + \frac{2}{j_x \tau_x} C_q \gamma_0^2 \frac{I_5}{I_2}. \quad (2.129)$$

$C_q$  is the quantum radiation constant and  $I_5$  is the *fifth synchrotron radiation integral* defined as:

$$I_5 = \oint \frac{\mathcal{H}_x}{|\rho^3|} ds, \quad (2.130)$$

with the dispersion function  $\mathcal{H}_x$ . The equilibrium emittance is then

$$\epsilon_0 = C_q \gamma_0^2 \frac{I_5}{j_x I_2}. \quad (2.131)$$

This leads finally to the equation for the horizontal emittance taking into account the quantum excitation:

$$\epsilon_x(t) = \epsilon_x(0) e^{-2t/\tau_x} + \epsilon_0 (1 - e^{-2t/\tau_x}). \quad (2.132)$$

The natural emittance depends on the dispersion, and although the vertical dispersion is assumed to be zero, the vertical emittance will not also damp to 0. This is due to the opening angle of synchrotron radiation, which can be approximated to  $\frac{1}{\gamma}$ . Therefore particles in sections of horizontal dispersion may emit photons with vertical momentum, leading to vertical betatron excitation and a non-zero vertical natural emittance. However in practice, the vertical emittance is usually limited by alignment and tuning errors.

## 2.4 Collective Effects

Until now most discussions have focused around dynamics of individual particles. Collective effects summarize effects of short and long range particle-to-particle, as well as particle-to-environment interaction. As discussed previously, due to the acceleration and energy loss compensation using RF cavities, the particles are arranged in bunches clearly separated by  $\omega_{\text{RF}}$ . The actual bunch size is small compared to the RF period, as discussed in Section 2.3.3. Also the total number of bunches is defined by the RF period and the revolution frequency, resulting in the harmonic number  $h$ .

### 2.4.1 Space Charge

One bunch in a typical accelerator contains around  $10^{10}$  charged particles, with every particle having its own magnetic and electric fields interacting with surrounding particles. One can envisage a bunch as a smooth distribution of charge. Space charge effects will then lead to a change in the distribution based on the distribution itself. If the charge distribution is changing, this will lead to a change in beam size. Therefore space charge effects will lead to a defocusing on the beam. Because the forces due to space charge are non-linear and depend on the beam size itself, the effects on  $\beta$ -functions and phase advance cannot be derived by an exact, simple expression. However, as long as the space charge forces are small, approximations can be made. In general, a tune change  $\Delta\nu$  due to a integrated focusing error  $\Delta K$  can be written as:

$$\Delta\nu \approx \frac{1}{4\pi} \Delta K \beta_{x0}, \quad (2.133)$$

with  $\beta_{x0}$  being the  $\beta$ -function without space charge effects. The tune change  $\Delta\nu_x$  is the tune change for an individual particle inside the bunch, which can also be different compared to the tune of the whole bunch motion and is therefore referred to as the *incoherent tune shift*. Each particle can have a different tune and the distribution of tunes is called the *tune spread*. For a Gaussian beam the tune spread can be estimated by:

$$\Delta\nu_{x,\text{spread}} \approx 2\Delta\nu_x. \quad (2.134)$$

Space charge effects will also lead to creating image charges in the vacuum chamber which will lead to a *coherent tune shift* of the whole bunch. Other than the incoherent tune shift, the coherent tune shift can easily be observed by a change in oscillation frequency of the bunch and can be compensated for, for example, by using quadrupoles. [1, p. 395-428]

### 2.4.2 Scattering

Particles inside a bunch do not only interact via their electric and magnetic fields but also due to scattering. In general, scattering can be described as momentum conversion between the momentum vectors of the scattering particles. This *intra beam scattering* will lead to a growth in emittance. For electron storage rings the emittance grow is not significant compared to the effects of synchrotron radiation, discussed in Section 2.3.6. Transverse scattering of particles leads to a momentum transfer from the transverse to the longitudinal plane and therefore the particles will gain an energy deviation  $\delta$ . Events leading to large

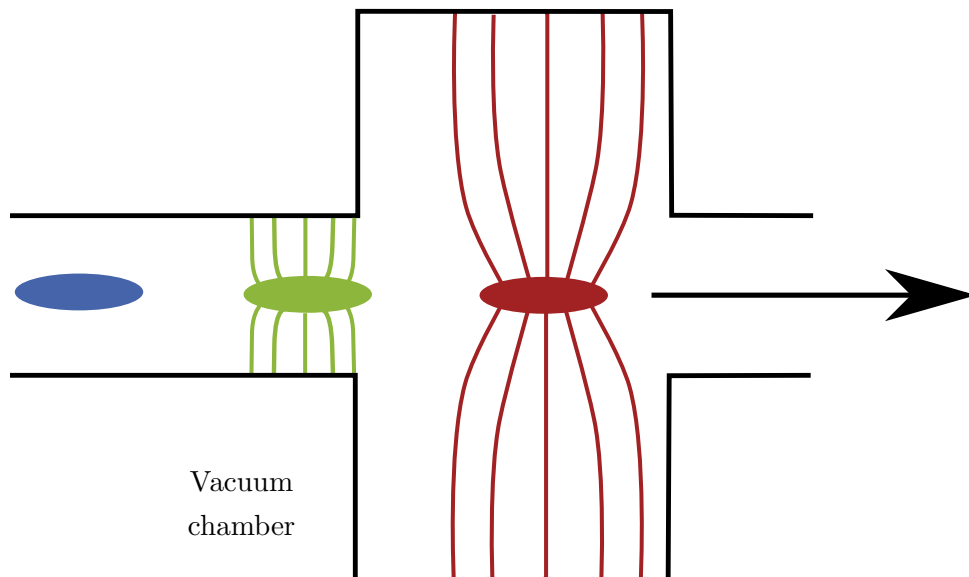


Figure 2.13: Visualization of wake fields inside a vacuum chamber. The electric and magnetic fields of an electron bunch (red) will create wake fields inside the vacuum chamber which will interact with following bunch (green). This bunch again will produce its own wake fields. The properties of the wake fields depend also on the electrical and geometrical properties of the vacuum chamber with every change in the shape adding some contribution to the wake fields.

momentum transfers will result in the particles exceeding the energy acceptance of the accelerator, resulting in the particles being lost. Since such a scattering event involves two particles with one particle gaining energy and one particle losing energy by the same amount  $\delta$ , both particles will be lost. This effect is called the *Touschek effect* and is one of the main factors in limiting the beam lifetime and leading to a steady loss of particles over time. The *Touschek lifetime*  $\tau_T$  is defined as the loss rate of particles over time  $dN_b/dt$  and depends on the number of particles, beam sizes and energy deviation leading to particle loss  $\delta_{\max}$ :

$$\frac{dN_b}{dt} \propto \frac{N_b^2}{\sigma_x \sigma_y \sigma_z \delta_{\max}^3}. \quad (2.135)$$

The second relevant scattering process leading to loss of particles is *residual gas scattering*, the scattering of individual particles of the particle bunch with remaining gas atoms in the vacuum chamber. Such a scattering event will eventually lead to a loss of a single particle compared to the two particle loss event of Touschek scattering. Depending on the characteristics of the accelerator, losses are usually dominated by one of these two scattering events. [1, p. 446-458]

### 2.4.3 Wake Fields and Impedance

So far, the effects discussed are limited to one bunch or interactions between the bunch and the vacuum chamber. But the electric and magnetic fields of each bunch will also lead to fields effecting following bunches. Such fields are therefore called *wake fields*. The *wake function* expresses the wake field as a function of distance from the source

to the particles experiencing the wake field. Wake fields can be long range and persist long enough to also interact with the original source on future revolutions. To analyze the effect on beam dynamics it is convenient to work in the frequency domain, where the beam oscillates with a certain frequency and beam instabilities present themselves as perturbations with amplitudes growing over time. The Fourier transformation of wake fields will result in an *impedance*. Significant wake fields are created in cavities, also referred to as *resonator impedance*. Impedance contributions by the vacuum chamber have less capacitive or inductive contributions but mainly pure resistive components because of its smooth structure. This impedance is called *resistive-wall impedance* and depends on the size, shape, and electrical properties of the vacuum chamber material. Changes in the vacuum structure also add to the general impedance budget of the accelerator. Figure 5.22 shows some examples of wake field propagation along the vacuum chamber. Wake fields will have many different effects such as emittance growth and distortion of particle distributions, and these can cause beam instabilities [1, p. 469-510].

#### 2.4.4 Coupled-bunch instabilities

For discussing bunch interactions and instabilities, a bunch can be viewed as a macro-particle  $n_b$  with charge and mass equal to the sum of charge and mass of all particles  $N_b$  in the bunch. Long-range wake fields can lead to coupled-bunch instabilities (CBI). In general, these wake fields will increase the amplitudes of betatron and synchrotron oscillations. As with most other cases due to the different characteristics of betatron and synchrotron motion the transverse and longitudinal situations can be looked at separately. For transverse motion with constant betatron function  $\omega_\beta$  the equation of motion in presence of a wake field  $F_x$  for the  $n$ -th bunch and the reference energy  $E_0$  can be written as:

$$\frac{d^2 x_n}{dt^2} + \omega_\beta^2 x_n = \frac{F_x c^2}{E_0 N_b}. \quad (2.136)$$

The wake field  $F_x$  is the sum of the fields generated by all bunches  $n'$  and all previous turns  $k$ . Furthermore, the field is the average field of the whole accelerator found by the sum of all wake potentials  $W(z)$  divided by the circumference  $C_0$ :

$$F_x = -\frac{(qN_b)^2}{C_0} \sum_{k=0}^{\infty} \sum_{n'=0}^{n_b-1} W(z) x_{n'} \left(t + \frac{z}{c}\right). \quad (2.137)$$

$z$  is the distance between the bunches  $n'$  and  $n$  and  $k$  times the circumference:

$$z = -\frac{n' - n}{n_b} C_0 - k C_0. \quad (2.138)$$

Solving the equation of motion using several approximations and replacing the wake field  $W$  by the transverse impedance  $Z^\perp$  will give:

$$\Omega_\mu - \omega_\beta = -i \frac{q^2 n_b N_b c \omega_{\text{rev}}}{8\pi^2 E_0 \nu_x} \sum_{p=-\infty}^{\infty} Z^\perp(\omega_p). \quad (2.139)$$

$\mu$  is the mode index describing the relative position configuration of all bunches. For  $\mu = 0$  all bunches have the same  $x$  position, at  $\mu = 1$  the relative position of all bunches

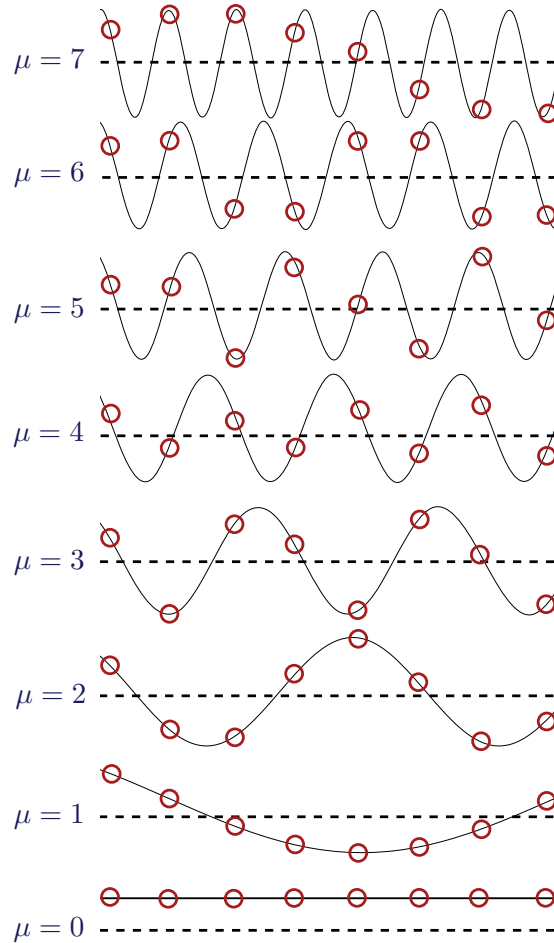


Figure 2.14: Visualization of the mode numbers  $\mu$  for coupled-bunch motion. All possible modes for a configuration for  $n_b = 8$  bunches are shown. The dashed line represents the reference path with  $x_n = 0$ . For  $\mu = 1$  the particles are arranged along a cosine period equal the circumference of the ring,  $\mu = 2$  a cosine period equal to half the circumference and so on. Adapted from [1].

is arranged along a cosine wave with a period equal to the ring size. For  $\mu = 2$  the cosine period is half the circumference and so on. The number of modes depends on the number of bunches:  $0 \leq \mu < n_b$ . Figure 2.14 shows all modes for an example of 8 bunches.  $\Omega_\mu$  is the betatron frequency of the mode  $\mu$ . The real part gives the betatron oscillation frequency in the presence of wake fields and the imaginary part gives the growth or damping rate of the mode amplitude. The frequencies  $\omega_p$  at which the impedance is evaluated is defined as:

$$\omega_p = \omega_\beta + (\mu - n_b p)\omega_{\text{rev}}. \quad (2.140)$$

$\omega_p$  are the frequencies at which the wake fields will be excited and need to be evaluated when calculating the effects on the beam. To evaluate the growth rate for the resistive wall impedance, the minimum  $\omega_{p,\text{min}}$  has to be used. For this,  $p$  must be  $p = 1$  and for  $\mu$ :

$$\mu = n_b - \text{int}(\nu_x) - 1, \quad (2.141)$$

with  $\text{int}(\nu_x)$  being the integer part of the horizontal tune. The growth rate for the fastest-growing mode induced by the resistive wall impedance is then:

$$\frac{1}{\tau} = \text{Im} \Omega_\mu = \frac{1}{I_c} \frac{(cC_0)^{3/2}}{4\pi^2\gamma_0} \frac{\langle I \rangle}{\nu_x b^3} \sqrt{\frac{4\pi}{Z_0 c}} \frac{1}{\sigma \sqrt{1 - \nu_{x,\text{frac}}}}, \quad (2.142)$$

with  $b$  being the radius of the vacuum chamber,  $\sigma$  the conductivity and  $I_c$  the characteristic current. Therefore, coupled-bunch modes for resistive wall impedance can be found close to  $n_b - \nu_x$ .

In general the amplitude of coupled-bunch modes depends on the wake fields, machine and beam parameters, but for accelerators with a high enough number of bunches, there will always be anti-damped modes present. For modes generated by resistive wall impedance there is also no current threshold and the growth-rate increases with beam current. In practice there is usually an effective current threshold where the growth-rates become larger than the damping effects due to synchrotron radiation and decoherence due to individual bunches oscillating with varying tunes.

For the longitudinal motion, wake fields due to resistive wall can be neglected. The main contribution to wake fields originates in the RF cavities. The longitudinal position  $z$  of a bunch is related to the energy deviation for this bunch  $\delta_n$  and the phase slip factor  $\eta_p$ :

$$\frac{dz_n}{dt} = -\eta_p c \delta_n. \quad (2.143)$$

Influences changing the energy deviation so far were due to the oscillation of the fields inside the RF cavities and synchrotron radiation with now an additional contribution in the cavities due to the wake fields. This resonator impedance  $Z^\parallel$  can be shown to be:

$$Z^\parallel(\omega) = \frac{R_s}{1 + iQ \left( \frac{\omega_r}{\omega} - \frac{\omega}{\omega_r} \right)}. \quad (2.144)$$

$R_s$  is the shunt impedance and  $Q$  the quality factor previously discussed in Section 2.1.2, and  $\omega_r$  is the resonant frequency of the cavity. Assuming the largest contribution comes from the fundamental mode  $\mu = 0$  and a resulting small tune shift,  $\Omega_\mu$  can be approximated by:

$$\Omega_\mu = \omega_z + \Delta\omega_z + \frac{i}{\tau}. \quad (2.145)$$

The synchrotron tune shift  $\Delta\omega_z$  is:

$$\Delta\omega_z = -\frac{q^2 n_b N_b \omega_{\text{rev}}^2 \eta_p Q R_s}{4\pi^2 E_0 h}. \quad (2.146)$$

For a large quality factor  $Q$  the growth rate is:

$$\frac{1}{\tau} = \frac{q^2 n_b N_b \omega_{\text{rev}} \eta_p Q^2 R_s \Delta\omega}{4\pi^2 E_0 h}. \quad (2.147)$$

This positive growth rate will lead to a longitudinal instability known as the *Robinson instability*. The impedance effectively adds an additional energy loss to the beam. This creates an imbalance in the energy loss for particles above or below the frequency of the reference particle. This can mostly be compensated for by operating the RF cavity slightly above the resonant frequency.

Since the growth rates of such instabilities is slow compared to the revolution time of the beam, active feedback systems can be used to measure and counteract frequencies in the beam motion which would otherwise lead to beam losses. This will be discussed in Chapter 4 and Chapter 6 in more detail [1, p. 512-540].

#### 2.4.5 Single-bunch instabilities

So far in the context of CBI, the bunches were viewed as macro particles and the effects of long-ranging wake fields effecting the growth and damping rates of certain bunch modes  $\mu$  across multiple bunches were considered. Separating one bunch into sub-macro particles of its own will show that short-range wake fields will lead to exponential growth of these sub-macro particles. The tail end of the bunch is then effected more strongly than the start of the bunch, hence such instabilities are referred to as *head-tail instabilities*. These instabilities not only depend on the presence of wake fields but also on non-zero chromaticity. Although this head-tail instability does not have a current threshold, for small, positive non-zero chromaticity, the damping effects of the accelerator is usually sufficient to suppress these instabilities. In general, single-bunch instabilities cannot be compensated for in the same way as CBI using an active feedback system due to the growth times being too short for a multi-turn feedback process [1, p. 540-551].

---

## 3. Karlsruhe Research Accelerator

The Karlsruhe Research Accelerator (KARA) is an electron storage ring at the Karlsruhe Institute of Technology (KIT) located in Karlsruhe, Germany. KARA provides synchrotron radiation for a diverse range of scientific applications along its beam lines but also serves as a research and test facility for accelerator design, diagnostics, and instrumentation.

### 3.1 Injector

Before electrons can be stored in KARA, they first have to be generated from an electron source and pre-accelerated in an injection section to reach the energy of 0.5 GeV required for stable circulation.

#### 3.1.1 Electron Source

The source of the electrons - usually referred to as the E-Gun - consists of a copper cathode, a grid, and an anode. By applying a field of 90 keV, electrons are freed from the

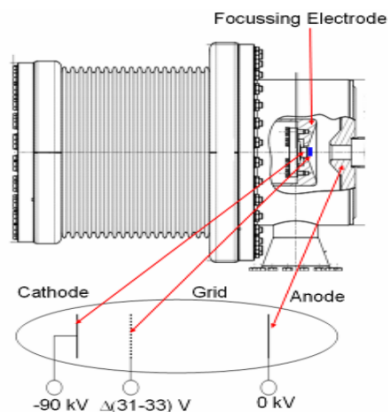


Figure 3.1: Schematics of the electron source. An electric field of 90 keV is applied to a copper block freeing electrons in the process and accelerating them to 90 keV [4].

---

cathode. Figure 3.1 shows the basic structure of the E-Gun [4]. The electrons are initially focused and subsequently enter the microtron. There, the electrons pass an RF linear accelerator (LINAC) multiple times. Every passage of the LINAC increases the energy of the electrons by roughly 5 MeV. After the initial pass the electrons are forced to perform a  $180^\circ$  turn and pass the LINAC a second time before they proceed to enter the magnetic fields of one of the two main dipole magnets of the microtron. After a drift section and the second dipole magnet the electrons return to the LINAC where they again gain more energy. Since the magnetic fields are static the electrons will travel on an extended path during the next circulation. This process is repeated until the electrons have passed the LINAC ten times and gained 50 MeV in total. Due to its characteristic form, this type of microtron is also called a race-track microtron. Figure 3.2 shows a schematic overview. After the final energy gain the electrons are deflected by another dipole magnet and are transported to the booster synchrotron through a transfer line [5].

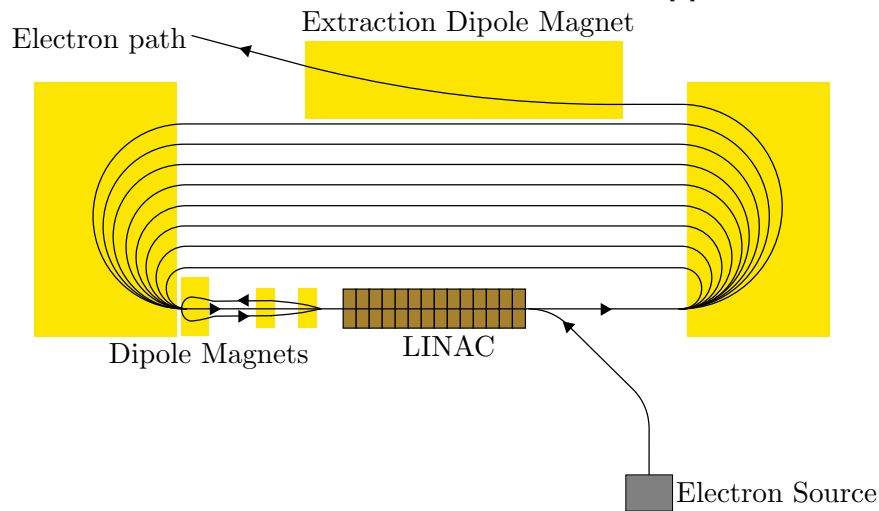


Figure 3.2: Schematics of the microtron. The electrons from the source reach the LINAC and experience an accelerating RF field providing an energy gain of 5 MeV. The dipole magnets (yellow) and the vacuum chambers are arranged so as to lead to 10 re-circulations through the LINAC for an overall energy gain of 50 MeV.

### 3.1.2 Booster Synchrotron

The booster synchrotron is a small storage ring and has some similar characteristics to KARA. It has a circumference of 26.4 m and consists of a FODO lattice which was discussed in more detail in Section 2.3.1. Every second  $D$  of the FODO lattice holds two dipole magnets. The remaining drift sections are used for the transfer line coming from the microtron and the one leading to the storage ring as well as the RF cavity and some general diagnostics. Figure 3.3 shows the schematics of the booster including the basic parameters in Table 3.1. Figure 3.4 shows the  $\beta$ -functions and horizontal dispersion.

The beam generated in the microtron LINAC has a 3 GHz longitudinal structure defined by the RF system there. On the other hand, the booster RF system works at a frequency of 500 MHz, which means that the beam needs to be re-bunched at this stage. KARA and the booster share the same  $f_{\text{RF}}$ , corresponding to buckets of a duration of 2 ns,

Parameter	Value
Energy	53 – 503 MeV
h	44
Circ.	26.4 m
$f_{\text{RF}}$	500 MHz
$f_{\text{rev}}$	11.36 MHz
$I_{\text{beam}}$	5 mA
Cycle	1 Hz

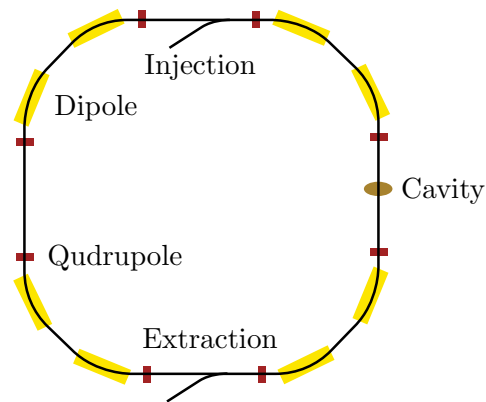


Table 3.1: Booster Parameters    Figure 3.3: Booster Schematics. Showing the FODO structure, injection, extraction, and RF cavity.

so no further RF manipulations are needed. The beam circulates in the booster for about 0.6 s allowing for roughly seven million revolutions. During this time the energy of the electrons is increased. This is achieved by an increase of the field in the dipole magnets leading to an energy gain due to the phase focusing effect described in Section 2.3.3. At the same time, the RF voltage and the quadrupole fields are increased to compensate the growing losses due to synchrotron radiation and adjust for the change in momentum. At the end of the energy ramp fast kicker magnets are triggered leading to the extraction of the beam towards KARA. Over the next 0.4 s the magnets and RF voltage are restored to the original values at the start of the energy ramp to accept the next beam coming from the microtron, creating an overall 1 Hz injection cycle. Figure 3.5 shows the measured injection cycle of the booster synchrotron.

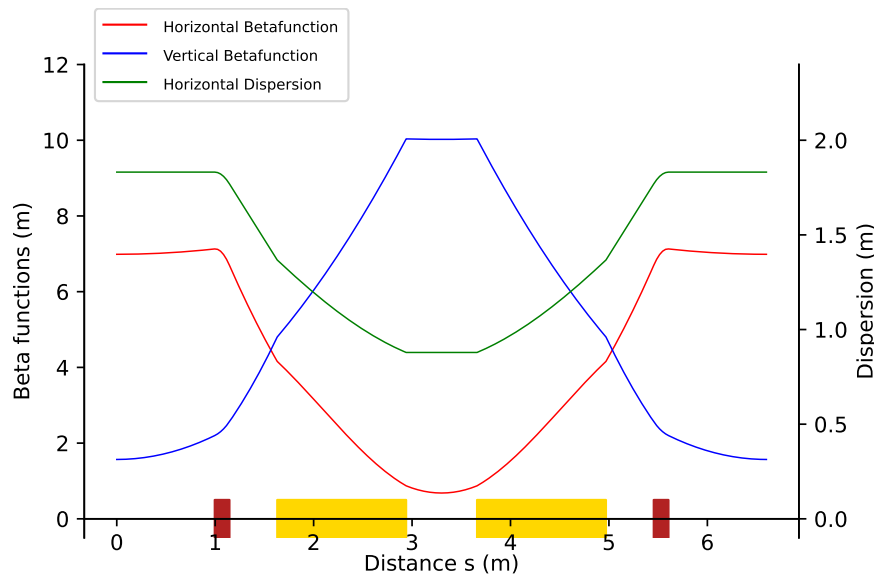


Figure 3.4: Booster Synchrotron Optics. Displayed are the two  $\beta$ -functions and the horizontal dispersion. On the horizontal axis the location and length of the magnets is shown (dipole magnet is shown in yellow, quadrupole magnet is red). Only one quarter of the booster is shown, since the optics repeats itself every quarter.

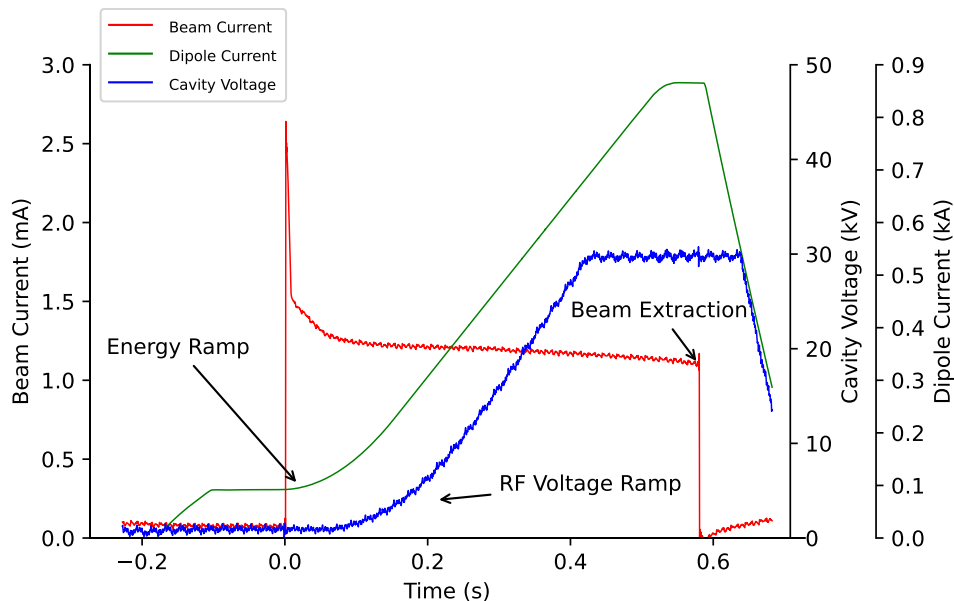


Figure 3.5: The 1 Hz Booster Synchrotron Beam Cycle. This plot shows the relevant part of the 1 Hz booster cycle. On the x-axis is the time in seconds. All curves are arbitrarily scaled to visualize the effects of the injection cycle. Injection into the booster happens at  $T = 0$  s. The beam current (in red) drops by roughly 50% after the injection due to the changes in RF frequency and general acceptance concerns due to the transition from the microtron and transfer line to the booster [5]. Right after the injection the dipole field (in green) is increased leading to the energy gain of the electrons from 53 MeV to 503 MeV. The cavity voltage (in blue) also rises to compensate for the increase in synchrotron radiation losses. The energy ramp procedure takes roughly 0.6 s. Once the electrons reach the final energy the extraction process is triggered. Once the beam is extracted, the dipole and cavity fields use the remaining 0.4 s to reset for the next injection cycle.

## 3.2 Storage Ring

At KARA the magnetic lattice, RF system, instrumentation, and diagnostic toolkit are more complex than in the injection section in order to achieve long-term, stable, and flexible beam operation. Table 3.2 lists the most relevant parameters.

### 3.2.1 Magnetic Lattice

The storage ring has a fixed symmetry of four sectors based around the magnetic lattice of its main magnets. Each sector consists of two periodic cells of magnets. Each cell consists of two dipole, five quadrupole, and three sextupole magnets forming a double bend achromat (DBA) lattice. Figure 3.6 shows the layout of such a cell. The position of the magnets in the second cell of each sector are mirrored with respect to the first cell. Between the two cells forming one sector there are short drift sections which are referred to as a short straight sections. The longer drift sections between two sectors are called long straight sections. The key reason to use a more complex magnetic lattice is the possibility of tuning the synchrotron radiation integrals  $I_2$  and  $I_5$  which were discussed in

Table 3.2: Parameters for KARA.

Parameter	Value
Energy	0.5 – 2.5 GeV
Harmonic number	184
Circumference	110.4 m
$f_{\text{RF}}$	500 MHz
$f_{\text{rev}}$	2.71 MHz
$I_{\text{beam}}$	0.01 – 200 mA
Lattice	double bend achromat
Dipole magnets	16
Quadrupole magnets	40
Sextupole magnets	24

Section 2.3.6, allowing to achieve a lower emittance and more control over the  $\beta$ -functions. Two dipole magnets are used to compensate the dispersion. Depending on the needs of the operation cycle the five quadrupole families can be configured for low emittance, low vertical  $\beta$ -functions in the straight sections, or low  $\alpha_c$  leading to beam optics with very short electron bunches. In contrast, during the injection at 0.5 GeV, it is more advantageous to choose optics with a large acceptance so as to have more flexibility in matching the beam coming from the injector section. The transition to the desired optics can either happen during the increase of energy or also after the final energy is reached by adjusting all five quadrupole families at the same time.

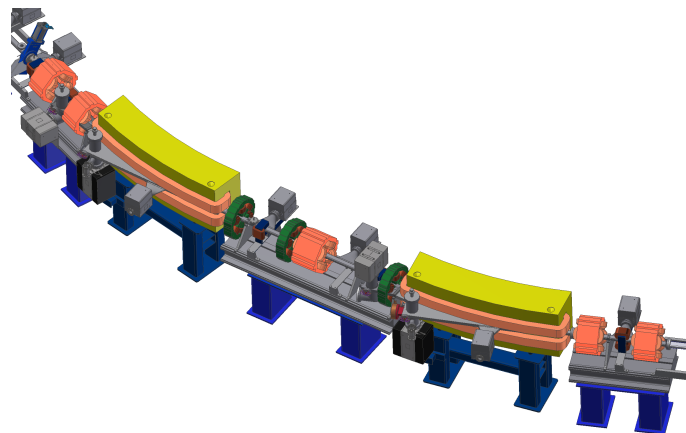


Figure 3.6: Storage ring magnet lattice. This shows the 3D model of one half of the magnetic lattice with two dipole magnets (yellow), five quadrupole magnets (red), and three sextupole magnets (green) forming the double bend achromat (DBA) structure.

### 3.2.2 RF System

The RF system of KARA consists of two RF stations on opposite sides of the storage ring with two cavities per station located in two of the four short straight sections. Figure 3.7 shows the model of one station. The RF system needs to be able to compensate for an energy loss of 622 keV per revolution at 2.5 GeV [6]. The RF stations are controlled by a digital low-level RF (LLRF) system enabling not only close monitoring of all relevant parameters but also allow for controlled excitations and active measurements [7]. Each station consists of a klystron and waveguides to create and guide the microwaves to two cavities. Part of the waveguides is a circulator to protect the klystron from potential reflections and a so-called *Magic-T* which splits the microwaves equally in front of the two cavities. While both cavities will get the exact same input microwave signal, each cavity can be tuned individually. Therefore the response of the beam – including possible reflections – is specific for each cavity. At KARA the effective behaviour of each cavity can be changed in two different ways: Mechanical deformation and temperature adjustment. Since the input frequency  $f_{RF}$  of the microwaves of the klystron is the same for all cavities, the mechanical deformation allows for tuning each cavity to be in resonance with this frequency. The temperature of the cavities is well controlled but can be changed, which influences the presence of higher order mode (HOM). These HOM will effect the longitudinal beam stability. This will be further explored in Chapter 6. Both stations are required to compensate the beam losses at 2.5 GeV. For beam energies below 2.1 GeV one station would be sufficient. But since running only one station has major implications on the (longitudinal) beam dynamics, typically both stations are always in operation.

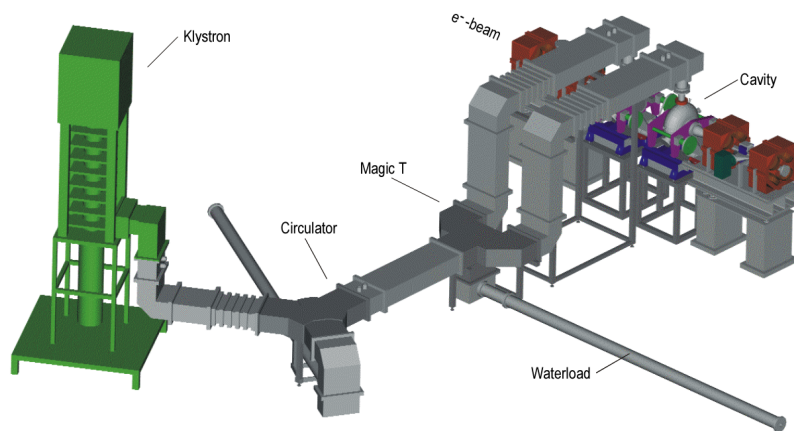


Figure 3.7: Overview of one KARA RF Station. The klystron creates the microwaves which are distributed to two cavities, which can be tuned individually. The Magic-T, the circulator, and waterloads are necessary infrastructure to support distribution and safety considerations regarding possible reflections of high power microwaves. Two of these stations exist at KARA to balance out the beam energy losses due to synchrotron radiation.

### 3.2.3 Vacuum Chamber

The vacuum chamber of any accelerator is an important part allowing the creation of the required ultra high vacuum for stable beam operation with high lifetimes. At KARA the vacuum is around  $1 \times 10^{-9}$  bar. Even at this low pressure, the scattering of the electrons with residual gas significantly impacts to the overall life time of the beam [8]. The dimensions of the vacuum chamber define the geometrical acceptance. The transversal plane of the KARA vacuum chamber is shown in Figure 3.8. The flat shape is a typical form for electron based accelerators due to the synchrotron radiation leading to a flattened electron beam shape. The shape of the vacuum chamber is changing in various locations: for example due to RF cavities, beam instrumentation, vacuum pumps, synchrotron radiation chambers, and in-vacuum movable devices, such as insertion devices or scrapers [9]. All of these factors contribute to the geometrical impedance discussed in Section 2.4.3. KARA is a test facility where insertion devices and beam instrumentation change over time, varying the dimensions of the vacuum chamber at specific locations and therefore affecting the overall impedance of the accelerator.

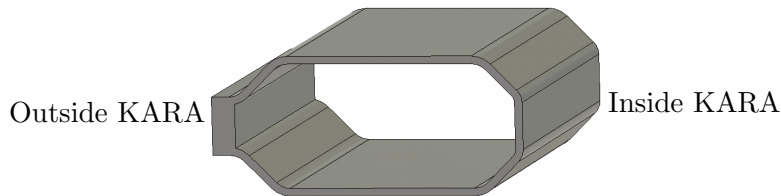


Figure 3.8: The transversal plane of the KARA vacuum chamber. This shows the basic layout and dimensions of the vacuum chamber with a width of 72 mm and a height of 32 mm. The flat shape is a typical form for electron based accelerators due to the synchrotron radiation leading to a flattened electron beam shape. Due to the necessity of supporting infrastructure such as vacuum pumps, RF cavities, injection area, and others the vacuum chamber is not homogeneous. Especially the vertical chamber size is reduced substantially in the areas of the straight sections so as to facilitate insertion devices.

### 3.2.4 Insertion Devices

Usually the physical space around the vacuum chamber of a storage ring is quite limited to install additional diagnostics or other devices. Therefore, by design, several drift or straight sections exist. At KARA there are four long (4.51 m) and four short (2.24 m) straight sections. As previously discussed, two short straight sections are occupied by the RF stations and another one is needed for the transfer line from the booster, leaving overall five straight sections to be used for special applications. While some additional beam instrumentation is also located inside the straight sections, the main use case are so-called insertion devices. There are many different variations and types of insertion devices, but their main purpose is to create synchrotron radiation with higher overall flux or other characteristics which cannot be achieved by synchrotron radiation emitted at dipole magnets. To generate synchrotron radiation these insertion devices force the beam

to oscillate locally along the beam path with specific period lengths leading to constructive interference of synchrotron light. To limit the effect this kind of beam disturbance has on the other sections of the storage ring the beam needs to be matched at the entrance and exit of the straight sections, both by local corrections of the orbit and also by global adjustments of the beam optic. One important parameter to control is the vertical  $\beta$ -function. Additionally, insertion devices usually also have the option to reduce or increase the strength of the oscillation by either changing the current in the magnetic coils (in the case of electro-magnetic coils) or physically increasing the distance of the magnetic coils from the center of the vacuum chamber. For example at KARA, all insertion devices only have a negligible influence on the beam during the injection process. The specific characteristics of insertion devices will not be discussed in this thesis. But insertion devices often use a different structure on the local vacuum chamber so as to be able to move the coils closer to the beam in order to be more effective. At KARA, one insertion device only has a vertical vacuum chamber size of 8 mm compared to the default height of 32 mm. The effect of the insertion devices on the impedance will be discussed in Chapter 5. Table 3.3 shows an overview of insertion devices that changed the impedance in the time period relevant for this thesis.

Table 3.3: Overview of Insertion Devices that are or were in use since 2013 at KARA.

Range of vertical chamber size means that the in-vacuum gap is movable.

Year of Installation	Name	Vertical Chamber Size
2007	SUL [10]	8 mm
2013	CatAct [11]	15 mm
2015-2016	SCU15 [12]	7-15 mm
2016	CLIC [13]	13 mm
2017	X-Spec [14]	7-110 mm
2018	SCU20 [15]	7-15 mm

### 3.3 Operation

KARA can keep the electron beam stored at any energy between 0.5 GeV and 2.5 GeV for many hours and operates in different beam optics and current regimes. Since the injector section can only deliver electron bunches with limited bunch charge and a maximum energy of 0.5 GeV, operating KARA usually involves an operation cycle with an injection period, an energy ramp and a final beam operation state with steadily decreasing beam current.

#### 3.3.1 Injection & Energy Ramp

During the injection period the booster synchrotron transfers additional electrons every second into the storage ring, where the previously injected electrons are being combined with the incoming electrons using a three kicker injection scheme [16]. To allow for efficient accumulation, the orbit of the electron beam is specifically designed with an off-center orbit

bump around the section where the injection takes place. Around 35 bunches from the booster reach the storage ring. This group of electron bunches in the storage ring is referred to as a *bunch train*. By slight delays in the timing of the injection cycle multiple trains can be injected. Injecting in the same bunch train leads to accumulating bunch currents in that train. The distribution and bunch current of the filled electron beam is usually referred to as the filling pattern. Depending on the operation mode and the desired overall beam current, the injection usually takes less than one hour to reach the desired beam current.

Once enough electrons are accumulated, the injection process is switched off and the energy ramp of the storage ring is initialized. While the general principle of the energy ramp is the same as in the booster synchrotron, the energy ramp in the storage ring happens on a longer timescale of some minutes compared to the 0.6 s of the booster. This is required due to the design of the iron coils of the main dipole magnets. The slow energy ramp allows for monitoring the changing beam conditions closely and for keeping the beam orbit in the limits of the geometrical acceptance. The automated orbit correction adjusts the orbit dynamically during the energy ramp at a rate of up to 2 Hz. Possible implications of the orbit correction on the beam dynamics will be discussed later. While the energy ramp can be stopped at any energy, the final energy is usually either 1.3, 1.6 or 2.5 GeV. While the energy ramp itself only requires the dipole to increase their magnetic fields, it is necessary to also increase the quadrupole and sextupole magnets accordingly, since the effective strengths of the magnetic fields are energy dependent. Otherwise the beam would not be able to keep the same orbit or even stay inside the vacuum chamber. By adjusting the quadrupole magnets the beam optics can be transformed from the initial injection optics focused on large acceptance to the desired beam optics depending on the planned operation mode.

### 3.3.2 Standard Operation

The most used operation mode at KARA aims at providing stable electron beam conditions for an extended period of time. This allows for synchrotron light experiments with a stable flux. Most experimental setups at KARA are using synchrotron radiation in the X-ray regime. Due to the characteristics of the synchrotron light spectrum (see 2.3.6) the preferred electron beam energy is 2.5 GeV. Since the flux of the radiation increases with the electron beam current, standard operation aims at injecting as much beam current as possible. This is usually achieved by using a filling pattern of up to four trains. Since in this operation mode all of the insertion devices are in use, the beam optics are designed for a small vertical  $\beta$ -function in the long straight sections [10], reducing the effect of the insertion devices on the global beam optic. The currently used optics can be seen in Figure 3.9, shown for one sector of the storage ring with very small vertical  $\beta$ -functions at the beginning and the end of the sector, which is where the long straight sections are.

To keep the synchrotron radiation at a stable position over several hours the electron beam needs to stay at the same horizontal and vertical position – or in other words to keep the same orbit. This is achieved by an automatic orbit feedback system. For the standard operation cycle, the beam is injected once per day. Figure 3.10 shows a typical full life

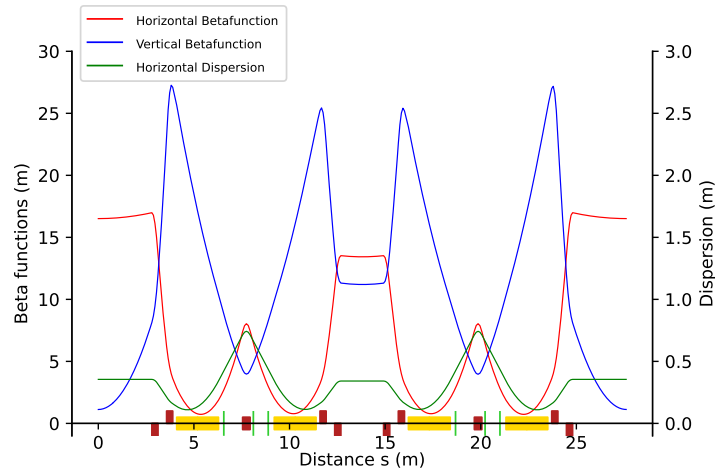


Figure 3.9: Standard Operation Optics. Shown are the  $\beta$ -functions and horizontal dispersion for one quarter of the storage ring. On the horizontal axis the location and length of the magnets is shown (dipole magnet in yellow, quadrupole magnet in red, sextupole magnet in green). These are the optics used for most of KARA operations at 2.5 GeV. The main goal of these optics is to provide small vertical  $\beta$ -functions in the straight sections. This is especially important for the long straight sections, which are located at the beginning and end of this figure, and are used to support insertion device operation [17].

cycle. Once the final energy is reached, the beam current drops over time in an exponential decay. Typically there is still a certain amount of beam current available after the 24 hour period, but at this point the flux of the synchrotron radiation has normally diminished. Therefore a new injection is scheduled which requires the removal of the existing beam and resetting of the storage ring parameters to allow a new injection cycle starting at 0.5 GeV.

### 3.3.3 Short Bunch Operation

While the standard operation mode's aim is to provide stable synchrotron radiation over several hours, the short bunch operation focuses on research of electron bunch behavior. While the bunch length in standard operation is in the order of 100 ps, the bunch length in short bunch operation is typically below 10 ps [18]. The natural bunch length increases with beam energy which is why the final energy for the short bunch operation mode is below the energy of the standard operation mode [19]. In the past this was typically at 1.3 GeV, due to beam stability considerations, but recently a short bunch mode has been established at injection energy of 0.5 GeV [20, 21]. To reduce the bunch length further the momentum compaction factor  $\alpha_c$  has to be reduced [22]. Since the momentum compaction factor is given by the integral over the dispersion as shown in Section 2.3.3, the overall dispersion has to be lowered. In contrast to the optics adjustments during the energy ramp, the transformation to the short bunch optics is performed after the increase of energy by additional adjustments of the quadrupoles. Figure 3.11 shows the optics where the dispersion is partially negative, resulting in an overall smaller integrated dispersion. During short bunch operation the filling pattern, injected total beam current,

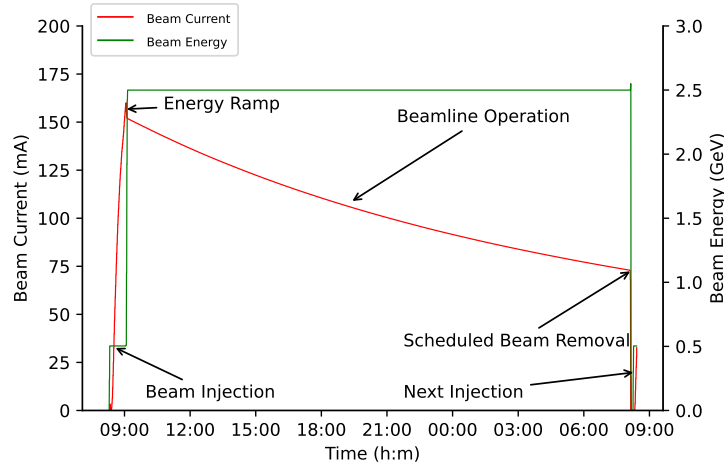


Figure 3.10: Standard Operation Mode Cycle. This plot shows the typical 24 hours of an electron beam injected for standard mode operation aiming for high accumulated currents and stable beam conditions at 2.5 GeV. The beam current (red) is accumulated during the injection at an energy of 0.5 GeV (green). During the energy ramp to 2.5 GeV some current is lost due to the drastic changes in beam dynamics.

and duration of one fill can vary drastically, depending on the planned experiment. The region of interest in the synchrotron radiation for this operation mode is in the far infrared and THz regime. Due to the reduced bunch length, the electron bunches emit high intensity coherent synchrotron radiation (CSR), which can be analyzed to study the electron bunch properties using the synchrotron radiation [22].

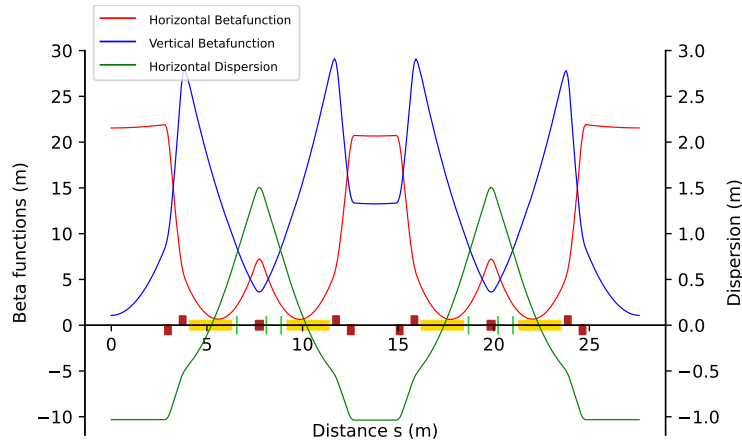


Figure 3.11: Short Bunch Optics. Shown are the  $\beta$ -functions and horizontal dispersion function. On the horizontal axis the location and length of the magnets is shown (dipole magnet in yellow, quadrupole magnet in red, sextupole magnet in green). These optics focus on providing very short bunches by decreasing the momentum compaction factor  $\alpha_c$  [17].

### 3.3.4 Other Beam Operation

Next to the two main operation modes described above there are also time slots reserved for machine development. Machine developments are dedicated beam time that covers a wide

range of topics starting at measuring default beam parameters such as the dispersion, beam alignment, conditioning or commissioning of new devices, investigating issues of beam stability, and developing new beam optics, among others. Operational parameters such as filling pattern, energy, or beam optics will change depending on the research topic of the machine development

## 4. Bunch-by-Bunch Feedback System

Beam stability is a major concern in operating a particle accelerator. To be able to properly counteract potential instabilities on the timescales around milliseconds and shorter, some form of automatic feedback system is required. While feedback systems for many aspects of an accelerator exist, this chapter will focus on a so-called BBB feedback system. Such a system, generally speaking, is able to interact with the individual particle bunches which usually exist in an alternating RF based accelerator. The main motivation for this is that it allows such a feedback system to damp coupled-bunch motion and prevent CBI. The BBB feedback system is also a central element for this thesis. Most measurements and analysis in the following chapters 5 and 6 are based on measurements acquired or made possible by this system. It is therefore crucial to understand its working principle, setup, and capabilities, which all will be discussed in this chapter.

### 4.1 Setup

To understand the working principle of a feedback system, the challenge of interacting with individual bunches can be separated into three tasks: Measurement of the oscillation of every bunch using a beam pick up, processing and analysing the bunch motion so as to calculate a correction signal, and feeding back this correction signal onto the beam using kicker structures. Ideally CBI should be damped before they can grow too much, so a fast response time is critical. With current technology, a response time after one revolution is achievable, which in the case of the KARA, results in a response time of about 368 ns. A schematic overview of this concept is shown in Fig. 4.1. Modern Bunch-by-Bunch (BBB) feedback systems use fully digital processing chains working with analog signals only on the in- and outgoing signals using analog-to-digital converter (ADC) and digital-to-analog converter (DAC). This digital approach allows for many additional applications making use of the available data which can be monitored and stored while being processed.

---

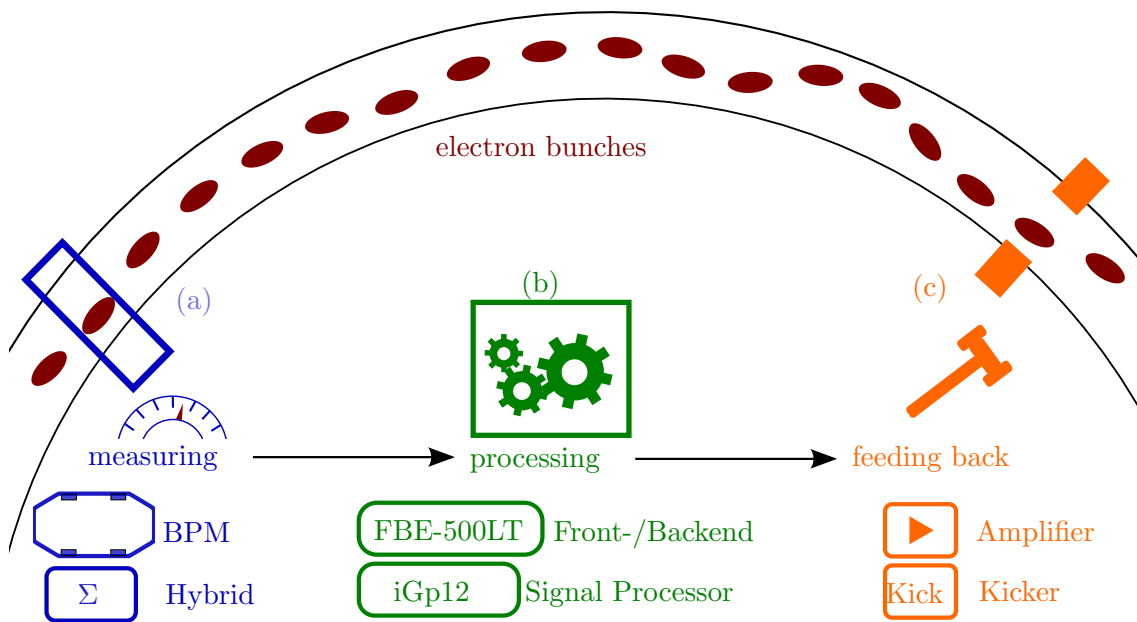


Figure 4.1: Working principle of the Bunch-by-Bunch (BBB) feedback system. The vacuum chamber and the electron bunches (in red) are not to scale. Shown are the three parts of a BBB feedback system: Measuring beam oscillations using a BPM and a BPM hybrid, digital processing of the data using a front-end/back-end (FBE) and a signal processor and feeding back a correction signal on the beam using an amplifier and a kicker structure.

#### 4.1.1 Beam Pick-Up

Measuring the motion of the beam is the first step of the feedback chain. This is made possible by measuring the position of the electrons using four button electrodes integrated into the vacuum chamber part of a beam position monitor (BPM), as shown in Fig. 4.2. With such a BPM, the relative positional difference from one revolution to the next for each bunch can be measured. The absolute position of the bunch is irrelevant for this use case. One such BPM serves as the input for the BBB system. Depending on how the information from the four buttons is combined, the signals can be split into oscillation information for the horizontal ( $\Delta X$ ), vertical ( $\Delta Y$ ) and longitudinal ( $\Sigma$ ) plane of motion. This recombination of the button information is done before the actual digital processing starts by using a so-called BPM hybrid network. Fig. 4.3 visualizes the working principle by showing a block diagram of how the signals of the individual buttons are processed. This has the advantage that the digital processing can be separated into each plane of motion from the start. To get a separation of the individual electron bunches, the readout frequency of the BPM has to be at least  $f_{RF} = 500$  MHz.

#### 4.1.2 Processing

The actual BBB system hardware takes care of the digital processing part. It consists of four separate hardware units: One front-end/back-end (FBE) and three signal processor (SP). The purpose of the FBE is to correctly sample the incoming signal with the central

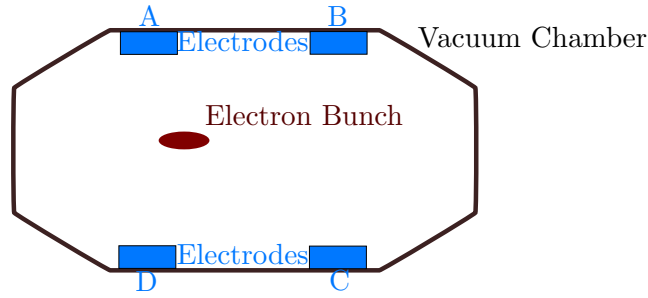


Figure 4.2: Schematic overview of a button based beam position monitor (BPM). Each button (blue) is an electrode with a RF throughput. A passing electron bunch with its attendant electric field will induce some charge in each of the electrodes, depending on the distance to the electrode. By adding and subtracting the buttons in specific ways, a relative horizontal, vertical and longitudinal position can be acquired. This will then serve as the input to the processing part of the feedback system. See Fig. 4.3 for details of how the signals are combined.

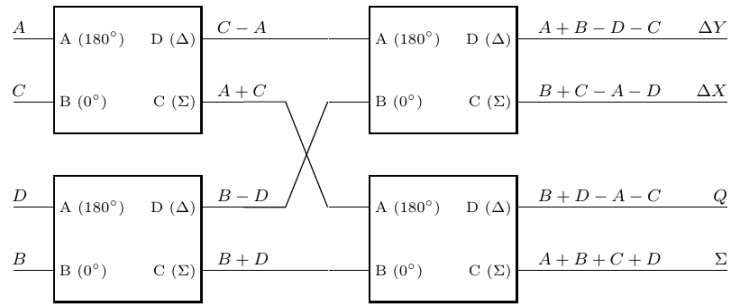


Figure 4.3: Block diagram of the BPM hybrid. The BPM hybrid is a passive RF component which takes the four signals from a button BPM  $A$ ,  $B$ ,  $C$ ,  $D$ , as seen in Fig. 4.2 and transforms these to four output signals:  $\Delta X$  and  $\Delta Y$  for the horizontal and vertical position,  $\Sigma$  for the sum and therefore longitudinal signal and the diagonal difference  $Q$ , which is terminated and not used [23].

$f_{\text{RF}} = 500$  MHz of the main RF system, which feeds the RF cavities and therefore defines the individual bunches as discussed in Sec. 2.3.3. Figure 4.4 shows the block diagram of the FBE unit. The signals from the BPM are therefore all fed through the FBE and mixed with  $f_{\text{RF}}$ . Each signal is then directed to one signal processor (SP). Each of the three SP are fully identical, but can be configured to the specifics of each oscillation plane. Additional timing signals are also added at this stage providing additional references, such as the revolution signal  $f_{\text{rev}} = 2.71$  MHz. This allows for the assignment of a fixed number to each bunch. The front panel of the SP is shown in Fig. 4.5.

#### 4.1.3 Transverse Feedback

The output signal of the SP is not strong enough to drive any kicker structure. Therefore the generated output signal has to be amplified using a suitable RF amplifier. A suitable kicker structure for transverse feedback is a *stripline*. The stripline in use at KARA is shown in Fig. 4.6. It has a high shunt impedance, a broad band frequency response from

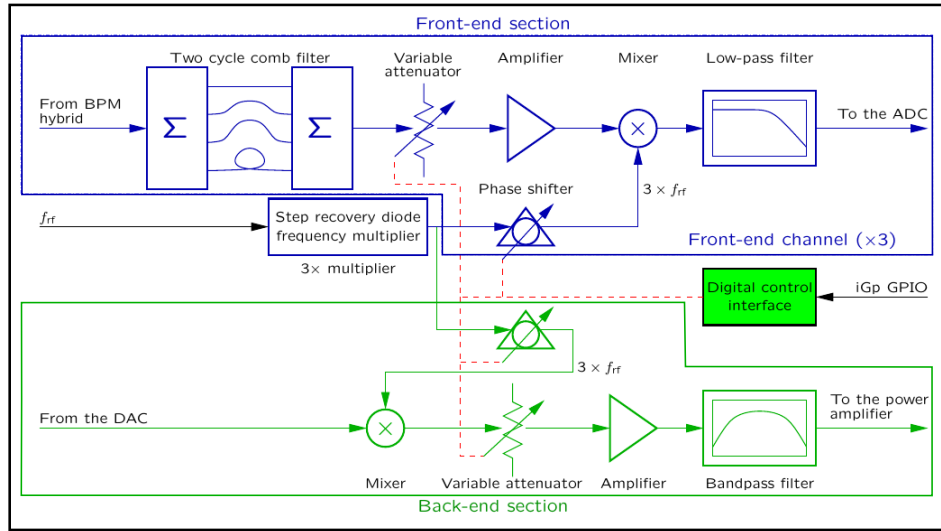


Figure 4.4: Block diagram of the front-end/back-end (FBE). The FBE incorporates electronics for pre- and post-processing the BBB feedback system signals. The unit is equipped with three identical front-end channels – for processing horizontal, vertical, and longitudinal signals. Front-end channels are designed for converting the BPM output to the baseband signal which can be directly used by the signal processor (SP) [24].

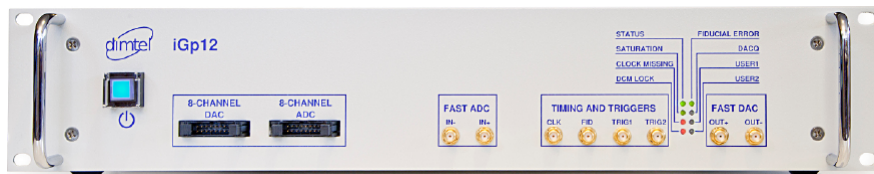


Figure 4.5: Front panel of a signal processor (SP). One unit processes the input and output of the horizontal, vertical or longitudinal signal. FAST ADC is the input signal, CLK expects the RF clock  $f_{RF} = 500$  MHz, and FID takes the revolution trigger  $f_{rev} = 2.71$  MHz. The signal output is FAST DAC, which will be sent to the kicker structure after being amplified by a RF amplifier.

0 – 250 MHz, and a length of 30 cm per section. Each of the two sections carries parallel plates in either horizontal or vertical configuration. This allows for the deflection of passing electrons by using a travelling RF wave in the opposite direction to the passing electron beam. As long as the overall size of the stripline is the same length as the bunch spacing (2 ns  $\sim$  30 cm), this makes it possible to influence the electron bunches individually [25].

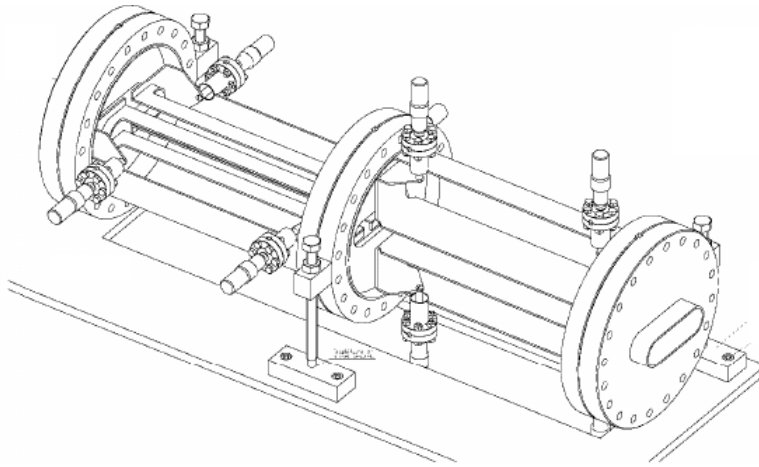


Figure 4.6: Cut-out view of two adjacent stripline structures for horizontal and vertical feedback. The stripline used at the KARA storage ring is based on the original development for Swiss Light Source (SLS) and ELETTRA [25]. Each section carries parallel plates in either horizontal or vertical configuration. This allows for the deflection of passing electrons by using a RF travelling wave in the opposite direction to the passing electron beam.

#### 4.1.4 Longitudinal Feedback

To influence the bunch motion longitudinally a kicker structure is needed which is able to create the necessary longitudinal electric fields, as discussed in Sec 2.1.2. Such a structure is a RF cavity, similar to the accelerating cavities of the RF system. The central frequency of this kicker cavity  $f_c$  has to fulfill the condition:

$$f_c = (p \pm 0.25)f_{\text{RF}} \quad (4.1)$$

with  $p$  being a positive integer. For the design of the cavity we followed the kicker design implemented in BESSY II. The design frequency for the KARA cavity is  $f_c = 1.375$  GHz. The inner parts of the kicker cavity can be seen in Fig. 4.7. Therefore in contrast to the transverse feedback, the output signal of the SP cannot be used directly, but has to be upconverted first. For this upconversion the outgoing signal of the SP is fed back into the FBE, but now to the back-end part. There, it is mixed with  $3 \cdot f_{\text{RF}}$ . Only now after the back-end, is the signal amplified by an amplifier. Before the connection to the kicker cavity, an RF splitter is used to create four evenly split signals which are fed into four of the eight ports to obtain suitable feedback. The other four ports are connected to a load [26].

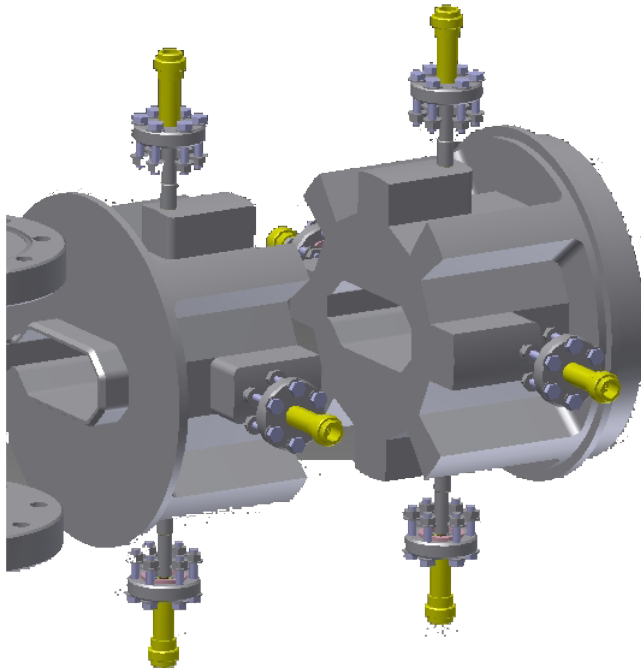


Figure 4.7: Cut-out view of the longitudinal kicker cavity. Shown is the inner structure with two segments, each with 4 ports. The longitudinal kicker cavity is a broad band structure which allows longitudinal influence on passing electron bunches and damping of all possible oscillation modes. It is based on developments at DAΦNE [27] and BESSY II [26]. The designed central frequency is  $f_c = 1.375$  GHz. This requires an input signal which is upconverted from the baseband signal of the SP. The signal is split to 4 ports of the cavity, whereas the other 4 ports are connected to a load.

## 4.2 Configuration

The BBB feedback system at KARA offers a large range of configuration parameters. This allows for maximum flexibility, but at the same time these parameters have to be carefully aligned to the beam conditions and to the specific requirements of each plane of motion. Each SP can be configured individually.

### 4.2.1 Temporal and Phase Alignment

To make the feedback system independent of a fixed location and cable lengths, it is possible to adjust most signals with regard to phase and timing. Aligning all these signals is crucial for successfully commissioning and operating the BBB feedback system. The SP and FBE units allow for the adjustment of the relevant parameters via the control system interface. Parameters required for basic commissioning are listed in Table 4.1. The incoming and outgoing data signals passing the ADC and DAC have to be aligned so that the  $n$ th measured bunch on the incoming signal from the BPM is the same as the  $n$ th bunch on the outgoing signal to the kickers. For achieve this both channels have a coarse delay to offset whole RF buckets (2 ns steps) and a fine delay inside the bucket. Compared to the size of the RF bucket, the actual bunch only occupies a small part of the bucket, as discussed in 2.3.3. Figure 4.8 shows the alignment options in detail. The frond-end phase

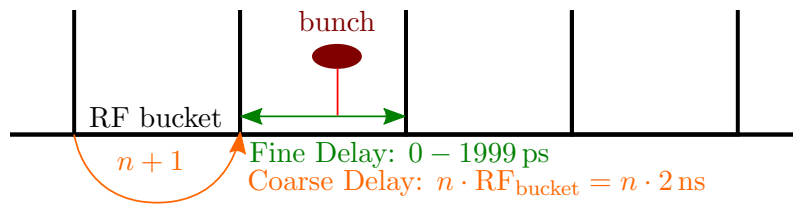


Figure 4.8: Schematic of temporal alignment. Both the input and the output signals have to be temporally aligned to the bunch signals. For this, each signal can be adjusted by a coarse and a fine delay. The coarse delay is in number of buckets and therefore shifts the signal by  $n \cdot 2$  ns. The fine delay can shift the signal by 1-1999 ps.

aligns the reference 500 MHz clock signal to the beam signal. The fiducial delay makes sure that the trigger signal for the revolution trigger is stable. The fiducial offset defines the bunch numbering relative to the revolution clock. This is relevant for defining the first bunch and relative alignment between the three SP, so that the  $n$ th bunch is the same across all three planes of motion. The back-end phase is only relevant for the outgoing longitudinal signal, since it has to be upconverted and is therefore mixed again with the main clock signal. The  $\text{RF}_{\text{bucket}}$  is a useful unit in this context. It is defined by the overall  $f_{\text{RF}} = 500$  MHz and the harmonic number  $h$ . The overall number of buckets is  $h \cdot \text{RF}_{\text{bucket}}$ . Therefore, one  $\text{RF}_{\text{bucket}}$  represents 2 ns in the time domain.

The overall procedure follows these steps:

1. Fiducial delay, so as to move the edge of the revolution trigger by  $\frac{1}{2}\text{RF}_{\text{bucket}}$  off the edge of the machine revolution clock signal
2. Front-end phase, so as to maximize the incoming signal from the BPM for the transverse planes or minimizes it for the longitudinal
3. ADC and DAC fine delays, so as to adjust for the actual bunch inside the  $\text{RF}_{\text{bucket}}$
4. ADC and DAC coarse delays, so as to ensure that the correct the bunch is influenced
5. Back-end phase, so as to maximize the outgoing longitudinal signal which is then mixed again with the reference clock.

The ADC/DAC alignment is also shown in greater detail in Fig. 4.8.

### 4.2.2 Feedback Filter

The phase and temporal alignment, as discussed in the previous section, takes into account factors like geometrical position and cable length, which are the same for all bunches. For the desired active damping feedback on the individual bunch a phase shift of  $\frac{\pi}{2}$  relative to the bunch oscillation is required to suppress its own oscillation. Since every bunch can potentially oscillate with different phases in respect to other bunches, it is not possible to set a phase which would be valid for each bunch. Determining the individual phase shift for each bunch is achieved by an RF filter. For this use-case a Finite Impulse Response (FIR) filter is a suitable choice, since it has a linear response, rejects DC noise, and has phase and amplitude response at a given frequency. Such a filter is defined by the number filter

Table 4.1: List of parameters to align phase and timing for each SP.

Parameter	Function	Range
Front-end phase	$f_{\text{RF}} \Rightarrow \text{SP}$	0 - 4095
Fiducial Delay	$f_{\text{rev}} \Rightarrow \text{SP}$	0 - 1999 ps
Fiducial Offset	$f_{\text{rev}} \Rightarrow \text{SP}$	0 - 183 $\text{RF}_{\text{bucket}}$
ADC Fine Delay	$\text{BPM} \Rightarrow \text{SP}$	0 - 1999 ps
ADC Coarse Delay	$\text{BPM} \Rightarrow \text{SP}$	0 - 183 $\text{RF}_{\text{bucket}}$
DAC Fine Delay	$\text{SP} \Rightarrow \text{Kicker}$	0 - 1999 ps
DAC Coarse Delay	$\text{SP} \Rightarrow \text{Kicker}$	0 - 183 $\text{RF}_{\text{bucket}}$
Back-end Phase	$f_{\text{RF}} \Rightarrow \text{Kicker}$	0 - 4095

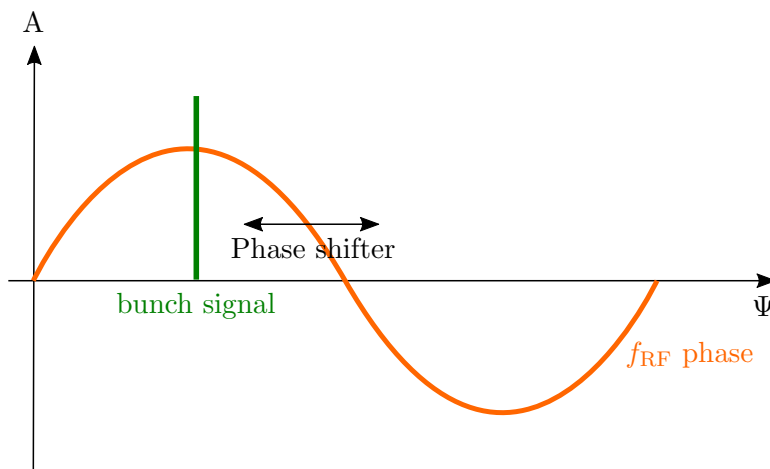


Figure 4.9: Schematic of phase alignment. The phase alignment happens in the front-end part of the FBE unit. The 500 MHz reference clock can be phase-shifted before it is getting mixed with the comb-filtered beam signal (see Figure 4.4 for the detailed block diagram).

coefficients ( $N$ ) also called taps. Using more taps means more complex filter behaviour which allows for narrower but also steeper response. It also requires more memory to store the coefficients. As we will see later, the transverse tunes may change significantly during the life time of the electron beam, which adds another criterion which must be taken into account. This usually means selecting a lower number of taps so as to get a wide response in the filter, which makes the filter usable for a wider range of tune values. All parameters used to describe a filter set are listed in the Table 4.2. Other parameters are the gain, which is a linear scaling factor between 0.0 and 1.0. The fractional frequency defines the center of the filter with the highest gain. Ideally, this should be close to the real bunch oscillation frequency. The phase allows for a relative phase shift of the filter. In the open-loop scenario without active feedback and in the theory, a phase shift of  $180^\circ$  is needed to achieve damping behavior. But for the closed-loop feedback other contributions have to be taken into account: a  $90^\circ$  shift due to a position measurement at the BPM but an angular kick at the kicker, the phase advance between the kicker, and the BPM and the phase advance over one turn (since the kick happens one turn after the measurement).

Table 4.2: List of parameters for the filter design.

Parameter	Function	Range
Taps	Number of filter coefficients	1 - 32
Gain	Relative scaling factor	0.0 - 1.0
Fractional frequency	Estimated bunch oscillation frequency	0.000 - 1.000
Phase	Relative phase shift of output	$-180^\circ$ - $180^\circ$

The relative phase compensates for all of these individual contributions. Additionally, some applications are designed to excite the bunch motion instead of the usually desired damping, requiring a  $180^\circ$  shift of the relative phase. Examples of filters with different number of taps are shown in Fig. 4.10. Four different filter sets can be stored on the SP. This makes it possible to seamlessly switch to a different filter without disturbing the feedback operation, which is useful in transitioning to regions with significantly different beam optics. If more than four different filter sets were to be needed, one of the inactive sets could be safely replaced by a newly calculated filter.

### 4.3 Advanced Features

To fulfill the main purpose – active damping feedback – the configuration options and setup listed so far would be enough. But the system also offers access to additional features, which the system intrinsically has to use anyway so as to be able to damp all possible coupled-bunch motion and for any individual bunch. The direct access to these advanced features is what makes the BBB feedback system a versatile diagnostic tool.

#### 4.3.1 Drive Sources

Each SP unit provides up to three drive sources which can create arbitrary signals, based on a set of adjustable parameters. These parameters include the excitation frequency  $f_e$  and an optional span and period to allow small variations around  $f_e$ . It is also possible to select which bunches should be affected by this excitation. Fig. 4.11 explains how these parameters form a signal which modulates the feedback signal. This can be used to drive the beam with any frequency up to  $\frac{f_{RF}}{2} = 250$  MHz. Using more than one drive source allows different drive signals to be overlaid in respect to any of the possible parameters. For example, one drive source could be set up to excite a certain range of bunches with frequency  $f_x$ , while another drive source could excite some other bunches with frequency  $f_y$ . The drive sources can also be operated in parallel to active damping feedback.

#### 4.3.2 Data Acquisition

Each of the SP units provides three data acquisition engines which are capable of recording beam motion. The overview of the three engines is listed in Table 4.3. All three engines can be accessed in parallel. The single-bunch (SB) engine can only acquire data of a specified single bunch, whereas the other two engines acquire data sets for all 184 buckets.

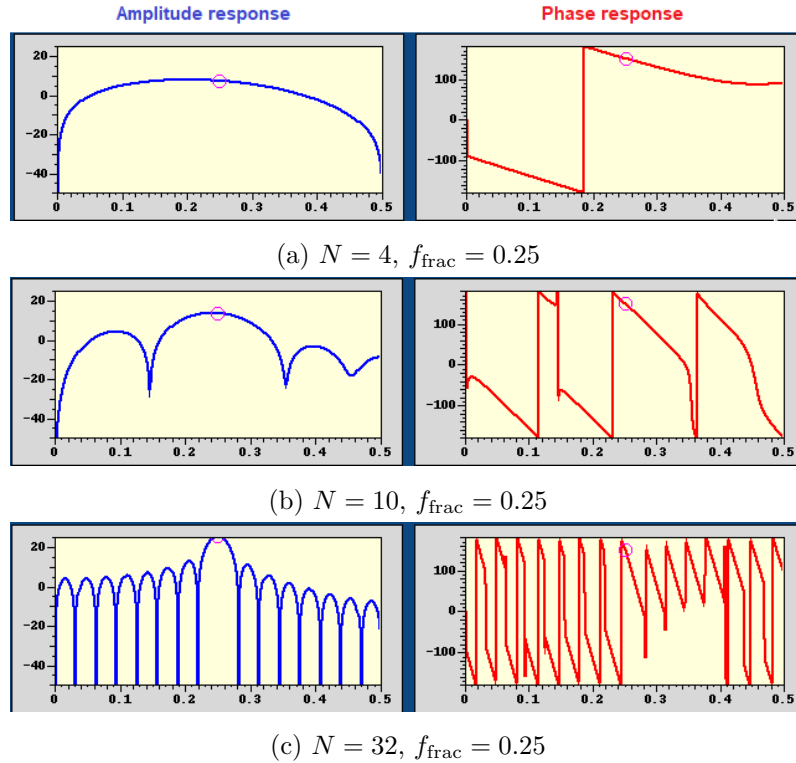


Figure 4.10: Generated FIR filter for the same  $f_{\text{frac}}$  with increasing number of taps  $N$ . The left (blue) curve shows the amplitude response. A higher gain in amplitude response will lead to an increased effect on the bunch. The right (red) curve shows the phase response. The circle serves as a visual marker to indicate the behavior for the defined fractional frequency  $f_{\text{frac}} = 0.25$  in amplitude and phase. For this example, at this position, the gain of the filter is the highest. (a) shows the minimum required taps to fulfill the basic requirements for a working filter. This low number of taps shows a medium gain and near flat response for a wide range of tunes in the amplitude response. Also the phase response (red line) allows for a wide range of fractional tunes. Increasing the number of taps will lead to an increased gain in amplitude response, but it narrows the possible tune range which will produce the desired filter effect.

The full data samples are only provided on request due to bandwidth constraints. In the default behavior the raw data is post-processed by the SP. This post-processed data consists of a mean and an RMS oscillation level for all of the 184 buckets, the time domain signal of the bunch with the maximum amplitude, and Fast Fourier Transformation (FFT) spectrum averaged over of multiple buckets. The calculation of the spectra can be adjusted by limiting the buckets to be taken into consideration, and by an averaging factor. The bunch limitation can be used to ignore empty buckets whereas the averaging might have to be increased for lower bunch currents. Both factors will affect the signal to noise ratio.

The SRAM and BRAM engines support the option to downsample the data by a factor  $n$ , which is an integer number up to the maximum of 32. Thereby the acquisition length can be increased by a factor of  $n$ , for example in the case of the SRAM engine, from 25.2 ms

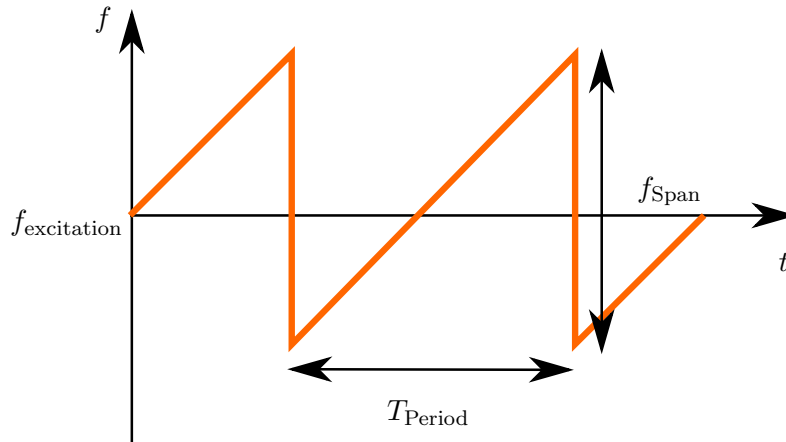


Figure 4.11: Overview of drive sources parametrization.  $f_{\text{excitation}}$  defines the main frequency of the excitation signal. With  $f_{\text{Span}}$  and  $T_{\text{Period}}$  it is possible to define a frequency sweep around this excitation frequency.

Table 4.3: List of data acquisition engines. Each SP provides multiple acquisition engines which can be accessed in parallel.

Engine	Readout Frequency (Hz)	Acquisition length (revolutions)	(ms)	Data points (kilosamples)
SRAM	2	68 384	25.2	12 500
BRAM	5	1536	0.565	282
SB	1	98 304	36.2	98

up to a maximum of 806.4 ms. The frequency range  $f_{\text{range}}$  is reduced due to downsampling  $n$  by:

$$f_{\text{range}} = \frac{f_{\text{rev}}}{2} \cdot \frac{1}{n}. \quad (4.2)$$

Depending on the region of interest, this allows lower frequencies with higher resolution or longer time-domain characteristics per acquisition to be studied. The given readout frequencies in Table 4.3 define the maximum internal processing speed of each acquisition engine. But each engine also supports a trigger by an external source, as long as the external trigger frequency is below the internal readout frequency. Additionally, each engine can be switched between continuous and single acquisition mode. Single acquisition mode can be triggered by the external hardware trigger as well as by a internal software trigger. This allows each SP unit to be synchronized to the same trigger event, making it possible to observe a given event from each perspective. Furthermore, due to the single acquisition mode or with a slow external trigger, this also allows enough time to extract an event in full detail before the next acquisition is triggered. The acquisition control supports additional parameters: The growth time  $T_{\text{Grow}}$ , the hold-off time  $T_{\text{Hold}}$ , pre-/post acquisition, and the grow-damp mode. Figure 4.12 shows an overview of how these parameters influence the acquisition window. Of special interest is the grow-damp mode. This will switch to the defined second filter coefficient set as discussed in Section 4.2.2 for

a defined and short period of time ( $T_{\text{Hold}} + T_{\text{Grow}}$ ) before switching back to the original filter.

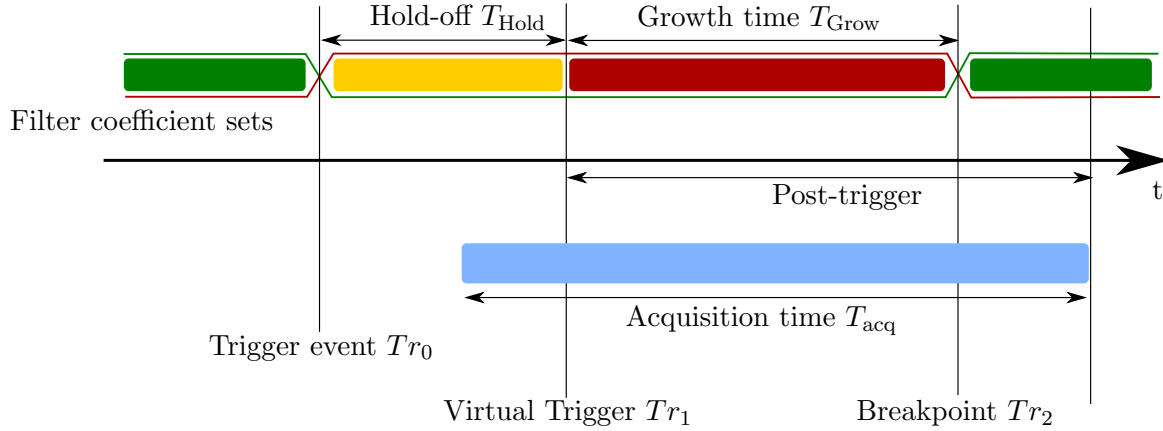


Figure 4.12: Parameters of acquisition engines. Next to the acquisition time  $T_{\text{acq}}$  there are various other parameters which will define the acquisition window. The acquisition can be triggered by an external or internal source. If the grow-damp mode is enabled, the coefficient filter set is switched from the default set (green) to the second set (red). The optional hold-off time  $T_{\text{Hold}}$  opens the feedback loop for the specified time to let the beam motion evolve naturally. The growth time  $T_{\text{grow}}$  defines the amount of time the second filter set is in use. Afterwards it will switch back to the default filter. The actual start of the acquisition window is by default defined by the virtual trigger  $Tr_1$ , which overlaps with  $Tr_0$  in case the hold-off time is 0. If needed it can also be shifted to start earlier by defining the post-trigger window smaller than the overall acquisition window. The break point  $Tr_2$  is available with every data set to be able to distinguish where the filter coefficient change happened.

## 5. Tune Diagnostics

The tunes describe the number of oscillations the electron bunches perform per revolution (see Sec. 2.3.4). It is an important characteristic of beam motion and the configuration of the magnetic lattice, also referred to as the *beam optics*. Due to the nature of KARA operating at different energies and different optics, as discussed in Chapter 3, the tunes will inevitably change during the course of operation. Therefore measuring and monitoring the tunes is important. The BBB feedback system provides multiple ways of measuring the tunes and, more crucially, also allows for continuous measurement across all states of beam operation. The first part of this chapter will address the different aspects of measuring the tunes using the BBB feedback system. Afterwards, how and why the tunes vary over time is discussed – with examples during the regular operation cycle, as well as the big picture over multiple years. This is followed by a section discussing *chromaticity* measurements, which the introduction of the BBB feedback system made possible to be measured automatically. Lastly, the transverse impedance as a current-dependent tune shift will be discussed.

### 5.1 Measurement Techniques

Since analysis and discussions in this chapter mostly focus on measurements of the horizontal and vertical tunes, the first part will focus on the different aspects and approaches made possible by using the BBB feedback system at the KARA. The physical meaning and mathematical description of tunes was previously discussed in Sec. 2.3.4. The tune describes the number of oscillation periods the particles perform during one revolution for one plane of motion. To measure the tunes, the acquisition engines of the BBB feedback system are used, which were discussed in Sec. 4.3.2. The acquisition engines not only record the oscillation in time domain, but already apply a Fast Fourier Transformation (FFT) and provide a spectrum. If the betatron oscillation is strong, the resonance frequencies can be directly seen in the spectrum. However, without instabilities, the resonance frequency usually cannot be identified. Therefore, measuring the tunes typically involves an active part to artificially enhance the magnitude of the frequencies in the spectrum.

---

As discussed in Sec. 4.3.2, the feedback system can measure and record the beam motion using different acquisition engines. Using either the block random-access memory (BRAM) or static random-access memory (SRAM) engine changes the length of the time domain signal, and therefore has an influence on the frequency resolution of the spectrum. The amount of consecutive revolutions the engine can acquire is listed in Tab. 4.3. The SRAM engine is able to record up to  $\approx 65\,000$  revolutions for each of the 184 possible bunches, culminating in over 12 million data points for each measurement. The BRAM measures for  $\approx 1536$  revolutions only, but provides a higher acquisition frequency of 5 Hz. The spectrum is calculated for each bunch and can be used to create an averaged spectrum over all bunches. Not every bucket is necessarily filled. A *spectrum pattern* can be set to define the the range of bunch numbers, which should be used for the averaged spectrum. The SRAM engine is able to calculate such a spectrum twice per second providing a data set with roughly 32 000 data points each. Two automatic peak finders will look for dominant frequencies in the spectrum. Since the resonance frequency is typically known to be in a specific frequency range, the peak finder can be limited to only look for peaks in that particular range. The peak finder returns the frequency and its amplitude. This reduces the data set down to only two data points per peak finder. The fractional tune  $\nu$  can be calculated using the measured frequency  $f$  and the revolution frequency  $f_{\text{rev}}$ :

$$\nu = \frac{f}{f_{\text{rev}}}, \quad (5.1)$$

also discussed in Sec. 2.3.4. The magnitude or amplitude can serve as an important quality factor to make sure that the found peak is distinctive enough by comparing the relative amplitude to general noise level of the spectrum. This approach to identifying the fractional tunes using only 2 data points for each measurement allows to continuously measure and store the data provided by the peak finder at the 2 Hz rate of the SRAM engine or at the 5 Hz rate provided by the BRAM engine in the general database.

### 5.1.1 Excitation Measurement

A common approach for tune measurements is a broad band excitation on the beam using horizontal and vertical kicker structures [28, p. 19]. In the case of KARA, the stripline which is also part of the feedback system setup discussed in Sec. 4.1.3, can be used in combination with the drive sources (Sec. 4.3.1). For the excitation using the drive source an excitation frequency and a frequency sweep range can be specified as shown in Fig. 4.11. Usually a frequency sweep range of 100 kHz is useful, since the betatron frequency is typically well known to be in this range. If the frequency is completely unknown, an even wider frequency range can also be applied, or, alternatively, the central excitation frequency can be changed until a response in the beam spectrum can be seen. Depending on the amplitude of the external drive, a peak will be visible at the given excitation frequency but the response at the resonance frequency is usually stronger. Figure 5.1 shows such a spectrum with driven excitation. Once the actual betatron frequency is known, the external drive frequency should be chosen in such a way that it can be clearly distinguished from the betatron frequency. Table 5.1 lists the relevant parameters required to successfully setup the frequency sweep so as to make the resonance frequency visible in

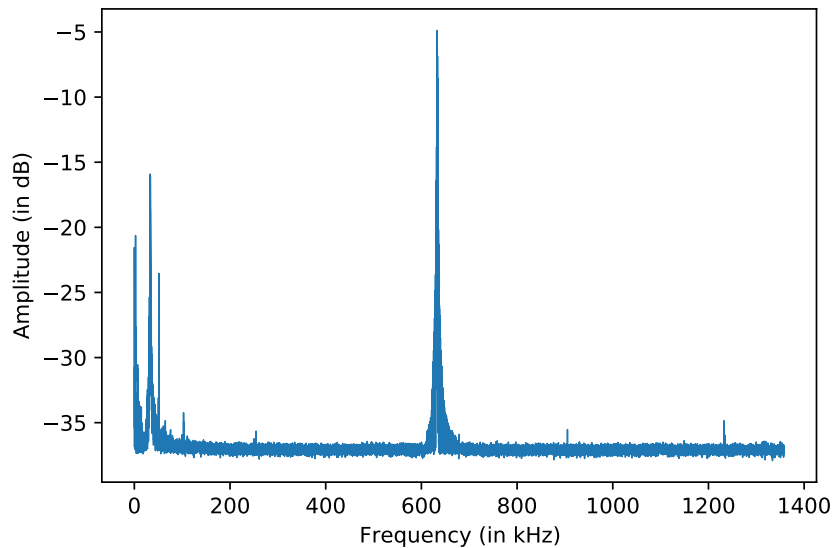


Figure 5.1: Example spectrum using the excitation method for tune measurements. This shows the result of a driven excitation by the BBB feedback system. The BBB system is set up to sweep over a frequency range of 100 kHz. Since the excitation amplitude is relatively small, a measurable response happens only around the betatron frequency. Looking for a maximum in that range will result in the peak finder measuring the betatron frequency.

Table 5.1: Parameters for excitation measurements.

Parameter	Description
Drive pattern	Excites the given bunches
Drive amplitude	Relative strength of excitation
Drive frequency	Excitation frequency
Sweep range	Sweep range around drive frequency
Sweep period	Time it takes for one frequency sweep

the measured beam spectrum. While this excitation approach is ideal to quickly find and identify the tunes, for example while exploring new optics settings, it becomes challenging to align all parameters so as to achieve the reasonable excitation in the spectrum for all different operation modes at KARA. Additionally, for operating near the limit of the accelerator either, in terms of overall beam current or dedicated – but intrinsically less stable – beam optics, ideally any additional beam distortion should be avoided. There is also the practical concern in the case where horizontal and vertical tunes are too close to each other, that even with using the peak finder limits, the resonance peak cannot be easily contributed to the correct oscillation plane. Therefore the excitation method is generally not used for continuously measuring the tunes across all operation states.

### 5.1.2 Feedback Measurement

A similar approach, but using the intrinsic properties of the active feedback loop of the BBB system, provides clear benefits compared to the excitation measurements. Independently

of the desire to measure the tunes, the active feedback loop is generally always preferred to be present so as to prevent beam instabilities from growing. More details on the feedback filters were discussed in Sec. 4.2.2, but once set up, the active feedback can counteract oscillations in following revolutions, leading to a very quick response. The transfer function  $L(\omega)$  naturally has a peak at the resonance frequency. For the active feedback, the transfer gain from the detection to the feedback input is given by  $\frac{1}{1+L(\omega)}$ , which will therefore create a negative peak – the so-called *notch* – at the resonance frequency [29]. An example of a beam spectrum with such a notch can be seen in Fig. 5.2.

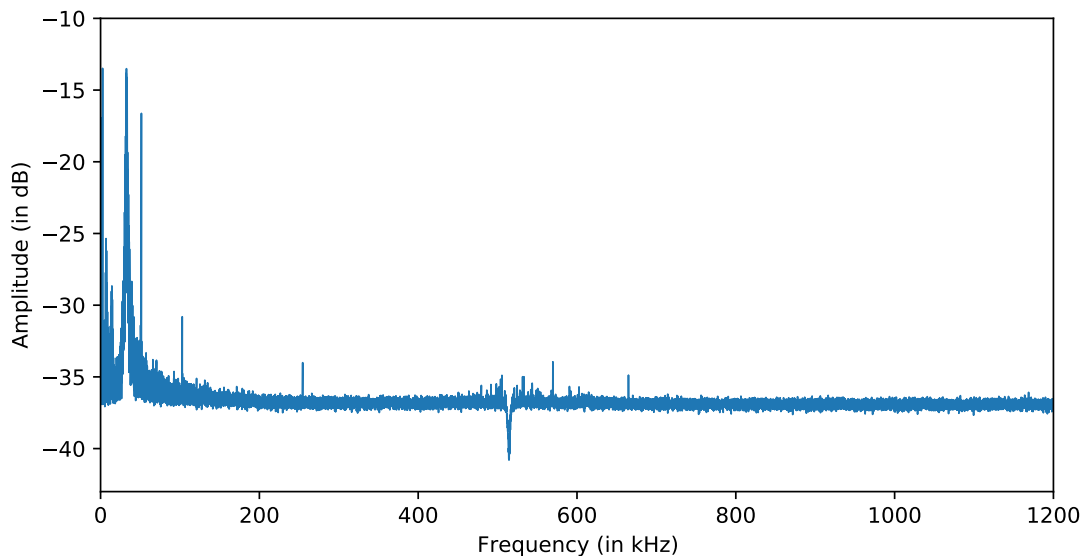


Figure 5.2: Example spectrum using the feedback method for tune measurements. Since the notch created by the feedback system is the only negative peak it is straightforward to track and monitor the notch for stable long term tune measurements.

Since there are no other negative peaks in the given spectrum, automatically detecting the notch becomes straightforward using the peak finder. Using the active damping of the feedback loop is very much desired for all operation states and therefore the loop is generally always active, providing the frequency detection via the notch as a byproduct of improved beam stability. The feedback filters can be set up in a way such that they provide active damping for a wide range of oscillation frequencies. As a consequence, these filters usually do not have to change for the different operation modes of KARA. If needed, the filters can be set up in such a way, that the transition from one filter to another happens seamlessly and will not interrupt feedback operation or the peak detection. Next to the general parameters for adjusting the averaging and bunch selection for the spectrum calculation, this leaves only one variable parameter with significant impact on the notch itself: the so-called *shift gain*, represented by an integer number between 0 and 7 in the BBB feedback system. An increase of 1 doubles the feedback strength and therefore affects the depth and shape of the notch. Figure 5.3 shows the notch for varying feedback gains for the same beam condition. Generally speaking, the overall beam current contributes to the relative depth of the notch, since the overall beam signal strength is reduced with reduced beam current. This is mostly mitigated due to the situation that the accelerator is usually either operated in a medium to high beam current regime and low beam currents

are not encountered during stable operation. If KARA is operated in an overall low beam current regime, the gain can easily be adapted. Monitoring and storing the tune based on

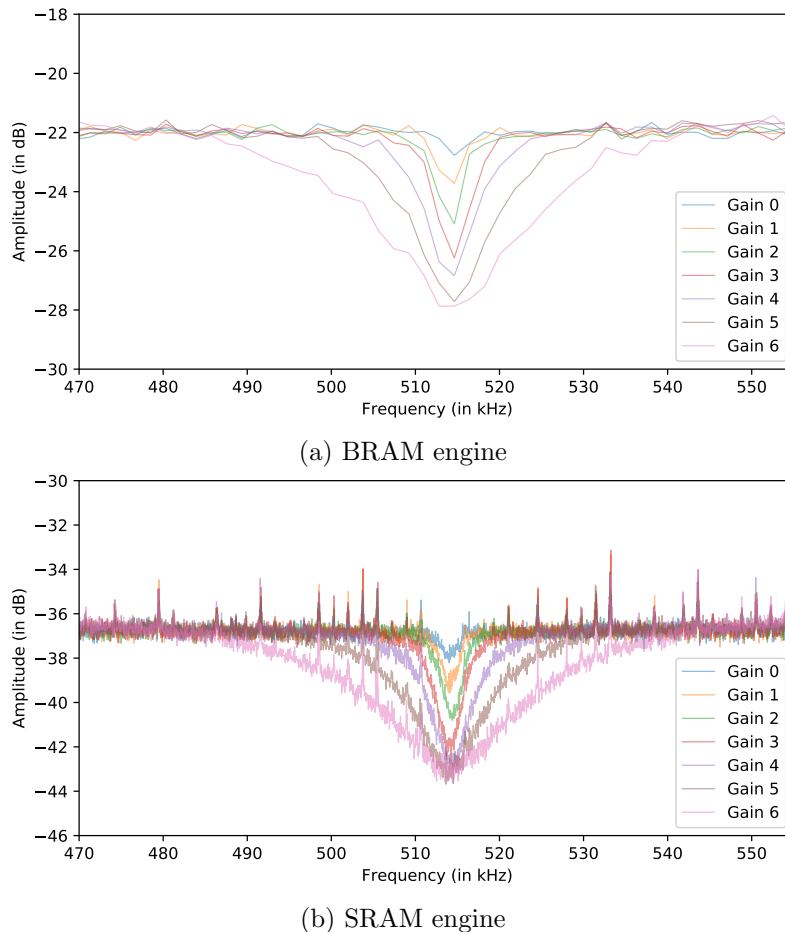


Figure 5.3: Tune notch for different feedback gains. Shown are the differences in the notch based on varying the overall gain of the feedback system. The top plot (a) shows the BRAM and the bottom plot (b) the SRAM acquisition engine. For a reasonable tune stability and signal to noise ratio, a notch depth  $\approx 3$  dB below the noise floor is sufficient. Using too much gain will have detrimental effects on beam stability and lifetime. Therefore for this given example, a feedback gain of 2 would be an acceptable level.

notch detection of the active feedback system leads to a robust long term measurement setup, since the active feedback is desired for nearly all operation modes of KARA. It is furthermore important to understand the limits of the tune measurement. One important lower resolution limit for the tune error  $\delta\nu$  is defined by the length of the acquisition window or the number of consecutive revolutions  $N$  and the FFT applied as given by:

$$|\delta\nu| \leq \frac{1}{2N}. \quad [28, \text{p. 21}] \quad (5.2)$$

Of interest for the error evaluation are also the statistical variations for a tune measurement over time. For this, the standard deviation was measured for different gains and averaging settings. The results are shown in Fig. 5.4 and listed in Tab. 5.2. Although an increased gain increases the depth of the notch, it shows a detrimental effect on the

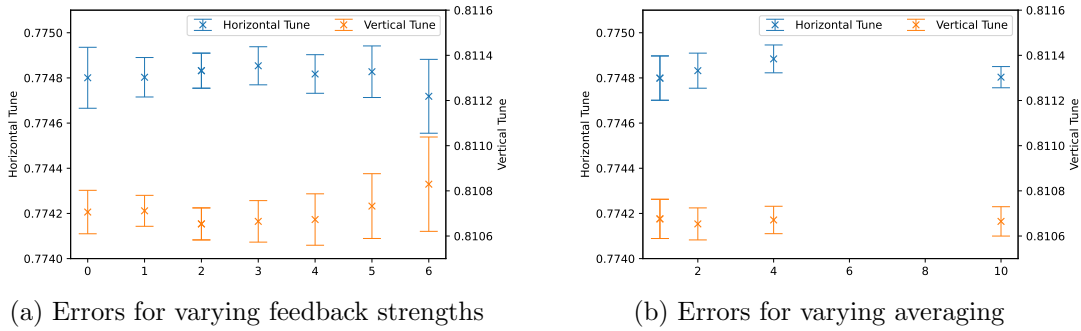


Figure 5.4: Study of statistical fluctuations of the feedback tune measurement. As long as the notch is visible in the feedback spectrum it can be easily identified. The depth and stability of the notch can be influenced by the overall feedback gain (a) or the averaging over multiple measurements (b). Shown is the effect in the standard deviation for different gains and averaging.

precision for the tune measurements. Fig. 5.3 shows that such a notch also gets wider, increasing the fluctuations on the peak finder. Too much gain will lead to an over-response of damping. Increasing the averaging does not have a significant effect. Since for this scenario, around 120 bunches were filled, the averaging over all filled bunches already greatly increased the signal to noise ratio, allowing for less overall averaging and therefore leading to quicker response in tune changes. This might also indicate that the resolution limit of the measurement approach is reached and cannot be improved upon by more averaging.

For the BRAM engine the theoretical best resolution achievable is  $\delta\nu_{\text{BRAM}} = 0.0003$ , based on its maximum acquisition length. This resolution is less than the standard deviation for most SRAM configurations. Therefore the BRAM engine is not suitable for precise tune measurements and will not be used further in the following sections. Based on the results for the SRAM engine, three conclusions can be made. First, although a higher shift gain increases the depth of the notch, it does not always increase the precision of the measurement. An ideal setting seems to be around a shift gain of 2 or 3. Secondly, more averaging does not improve the tune measurement, at least in this case. If enough bunches are available for the averaging, a rather low averaging factor is sufficient. This is also convenient, since the acquisition engine stays sensitive to changing tunes. For situations with significantly less bunches filled, the overall averaging will become more important. Thirdly, tune measurements using the SRAM engine is not limited by the best possible frequency resolution:  $\delta\nu_{\text{SRAM}} \approx 8 \cdot 10^{-6}$ . Overall, a minimum error can be defined based on these results:

$$\Delta\nu = 0.0001. \quad (5.3)$$

With the massive reduction of data from 12 million data samples down to two data points for the frequency and the amplitude of the notch, it becomes crucial to identify the quality of the notch measurement. There are some scenarios where the tune data clearly indicates problems with the notch readout. This is mostly due the peak finder not being able to find any notch at all. In that case the tune readout will randomly oscillate between the configured frequency limits of the peak finder with typical frequency ranges of 400–500 kHz, which is simple to spot in the measurement data. The most likely cause

Table 5.2: Statistical error for feedback tune measurements with varying feedback gains.

Shift Gain	Horizontal Std. Deviation	Vertical Std. Deviation
0	$\pm 0.0001$	$\pm 0.0001$
1	$\pm 0.00009$	$\pm 0.00007$
2	$\pm 0.00008$	$\pm 0.00007$
3	$\pm 0.00008$	$\pm 0.00009$
4	$\pm 0.00009$	$\pm 0.0001$
5	$\pm 0.0001$	$\pm 0.0001$
6	$\pm 0.0002$	$\pm 0.0002$

to losing the notch readout is miss-configured acquisition settings. This could be either due to the settings being just wrong or because the beam situation has changed to such a degree that the configuration is no longer ideal, for example if the beam reaches very low beam currents. Also unmitigated instabilities will effect the notch readout, since the shape of the notch will be affected. But there are also more subtle effects on the frequency readout, such as an instability that is almost under control, but still disturbs the notch readout. Important in judging the quality of a tune readout is therefore the amplitude of the peak, which is also measured alongside the frequency.

The previous measurements of varying depths of the tune notch already pointed to an ideal notch depth for the smallest fluctuations in tune readout, which is around  $-3$  dB relative gain to the noise floor of the spectrum. This creates some room for a reduction in notch depth based on overall natural beam current decrease over time. Constantly monitoring the amplitude makes it possible to identify the source of distortion, since for example, an overall decrease in beam current would also lead to an overall, but slow decrease in depth. Additionally, there is typically a second peak finder configured for the SRAM engine with the same frequency limits, but looking for positive peaks. This allows for the identification of a loss of notch readout due to an instability, which would manifest itself with a peak of nearly the same frequency, but a positive relative amplitude measured by the second peak finder. If there is no corresponding rise of the second peak finder, this would point to either a change in acquisition engine parameters, a change of tune larger than covered by the peak finder limits, or a substantial loss in beam current to either a very low or zero beam current. Looking at additional parameters such as the overall beam current allows to for the further narrowing down of the reason for a potential loss in tune readout.

Although the absolute amplitude of the notch is stored, the relevant value – the relative depth compared to the noise floor of the spectrum – is not provided by the feedback system. The noise level is constant during a fixed beam operation state. But it might change during transitions such as an energy ramp or over longer periods of time due to overall adjustments to the configuration, layout of the feedback system or other changes in either accelerator configuration or beam parameters. Since this is a likely scenario while looking at time ranges of multiple years, it is crucial to determine the noise level alongside the peak finder measurements so as to be able to calculate the relative notch depth and

use this as a quality criteria for the reliability of the tune measurement. Using the live spectrum a method was set up to calculate the mean noise floor and store this additional information, as well as directly calculating the relative notch depth without the need to store the full spectrum. For this it was assumed that the tail of the spectrum represents the noise level. Using a certain range of the tail spectrum the mean value can be calculated and stored as the measured noise floor. Using this value, the relative notch depth can be derived. Storing both values also makes sure that the taken assumption of constant noise floor for a fixed state of beam operation can be verified. Unfortunately, this approach is not possible for archived measured peak finder data, since the noise floor information cannot be reconstructed. Therefore, a different approach is to look at the brief periods of time before and after each beam operation cycle. There are typically at least some minutes of peak finder data available without actual beam in the accelerator. If this period can be isolated, the amplitude of the peak finder can also be used as the level for spectrum noise. It is important to consider in this case that since the peak finder will always look for the minimum in the given frequency range, the noise level derived via this method is systematically lower than the average noise level. Fig 5.5 compares both approaches. The difference is around 0.7 dB, which has to be taken into account when the notch depth of older measurements is compared to more recent measurements using the averaged noise level. Taking the relative notch depth, as well as possible peaks above the noise level into account, it is therefore possible with high degree of confidence to decide for each individual tune measurement if the read back value of the notch detection is reliable, which is crucial for studying changes in tunes.

### 5.1.3 Phase Tracking Measurement

Both the excitation and the feedback approach share some similarities, such as the method of data acquisition, spectrum calculations, and tune extraction. The phase tracking method however, is a completely different technique, fully independent of the SRAM acquisition engine and its limitations. The basic idea is that exactly at the betatron frequency, the amplitude of the beam transfer function (BTF) has zero slope and the phase difference between excitation and beam motion changes by  $180^\circ$  across the resonance [28, p. 26]. If the BTF is measured, this phase shift information can be used to constantly the beam at exactly the resonance frequency using a phase-locked loop (PLL) to lock on the  $90^\circ$  phase difference. This loop will adjust the drive frequency to stay on the correct phase to excite exactly the betatron frequency. Therefore the drive frequency will be identical to the betatron frequency and can be used to determine the tunes.

Fig. 5.6 shows a simplified block diagram for such a phase tracking loop. To be able to measure the precise phase transition, this method only takes a single bunch into consideration. To make it possible to measure the BTF, this bunch has to be excited. A very low excitation level is sufficient for the BBB system to pick up the BTF. Due to this and the need to only excite a single bunch, this approach is mostly a fully transparent measurement, although active excitation is needed. At the same time using a PLL allows for fast response times, depending on the loop filter gain and decimation. A higher gain will lead to a faster response to changes in frequency, but might also lead to over-correcting

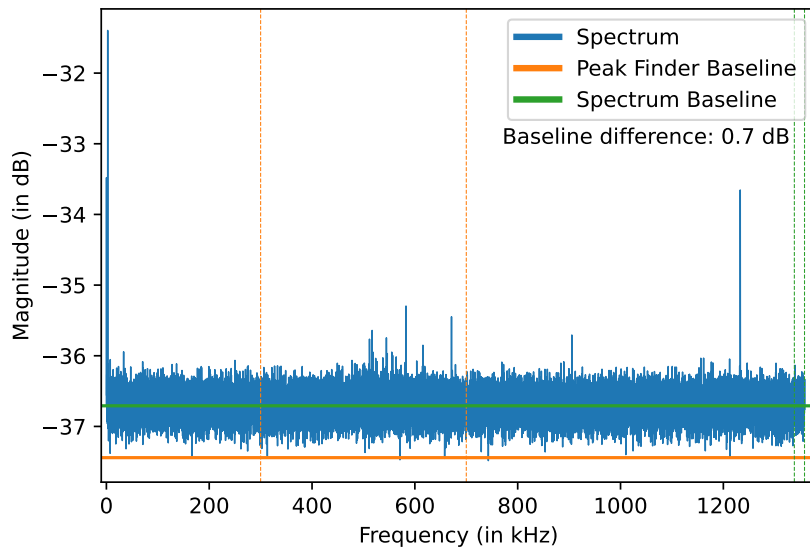


Figure 5.5: Noise determination of the beam spectrum. While the absolute amplitude of the peak finder is automatically stored, the relative notch depth is important to judge the level of confidence in the tune measurement. Therefore a method to calculate the noise level based on the live spectrum was developed using only the tail, which is generally speaking free of peaks. Since the spectrum data is very dense, already a small fraction, marked by the green vertical lines, is enough to calculate the noise level corresponding to the green horizontal line. For older measurements where this calculated noise level is not available, the noise level can be estimated by looking at periods without beam, since in that case the peak finder will only measure the noise between the defined frequency limits (orange vertical lines). It will still look for a minimum which results in an offset of around 0.7 db between both methods, which has to be taken into account.

and over-shooting. The decimation reduces the data density at the cost of losing some revolutions. The balance of these factors will determine the overall stability and speed of this measurement approach, while some additional parameters are needed for the general setup of the tracking. These are the number of the bunch to track, a drive frequency to start from, the drive amplitude to make the BTF measurable, and upper and lower frequency limits for tracking in case the lock on the phase transition is lost.

This approach does not rely on measuring many consecutive revolutions, calculating a FFT, and reading out large amount of data – which are all time consuming. Instead it can be used for very fast tune measurements. Successful tracking of the tunes was possible with a decimation level of 200 leading to a theoretical readout frequency of approximately 13 kHz compared to the 2 Hz of the previous approach using the multi-bunch acquisition engines (which might be further reduced in case of needed averaging). The dedicated single bunch (SB) acquisition engine can be used to acquire tune tracking at this decimation level. The maximum acquisition length of the SB engine is 98 304 revolutions, which translates to 36.2 ms acquisition time. Fig. 5.7 shows such a measurement. The tracked tune shows a very periodic behaviour, which is reproducible across all measurements. The standard deviation is very similar to the statistical error in tune measurements using the

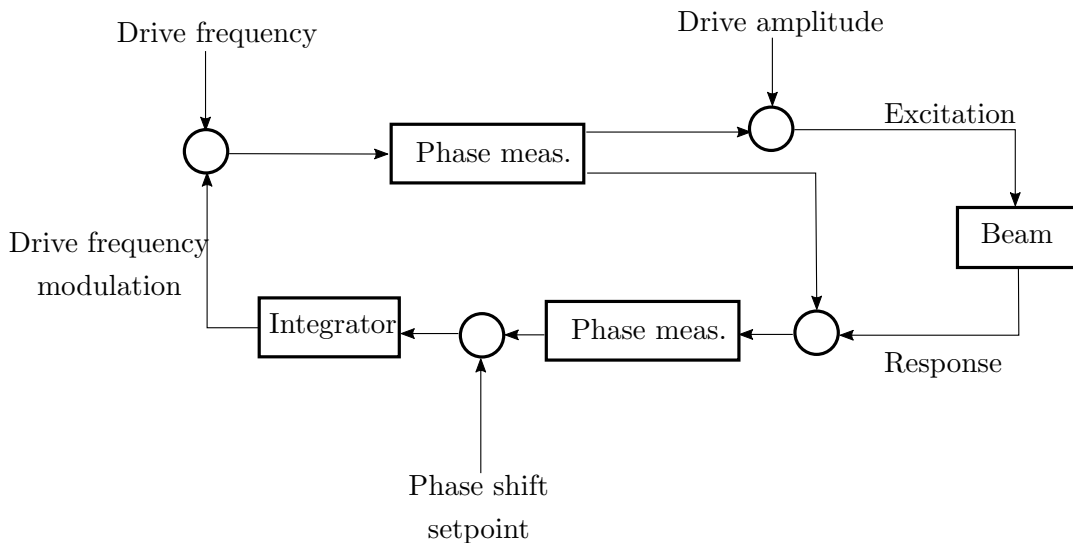


Figure 5.6: Simplified phase tracking block diagram. A single bunch is excited with a given frequency and amplitude. Measuring the beam phase of this bunch allows an integrator to move the excitation frequency to match the given phase setpoint. Since this method does not rely on calculating the spectrum and finding the peaks in that spectrum, it can be used for very precise and fast tune tracking. Important parameters to control the precision and resolution is the gain of the integrator, the overall decimation and a properly measured phase setpoint at resonance.

feedback approach and the SRAM engine:  $\delta\nu = \pm 0.0003$ . The periodicity of the oscillation is also very stable across all measurements and has a period length of about 20 ms. This is particularly interesting, since this corresponds to a frequency of 50 Hz, which is exactly the frequency of the main power grid in Germany, where KARA is located. The most likely explanation for the occurrence of oscillation is that the power supplies of the quadrupole magnets introduce this oscillation based on the general power grid frequency. This also implies that the tune stability and measurement is significantly affected by the stability of the quadrupole magnet power supplies. With more stable power supplies the standard deviation would most likely decrease, which would also result in the SRAM engine obtaining the resolution closer to the theoretical limit dictated by equation 5.2 and therefore improve all tune readouts.

The tune tracker can also be utilised in a slightly different configuration. By increasing the decimation to achieve similar readout frequencies to the feedback tune measurement approach it can be directly compared to an independent tune measurement technique, which might serve as a validity check for both measurements. For this, a decimation level of 500 000 is chosen, which leads to a readout frequency of roughly 5 Hz. To directly compare both measurements the idea is to use stable beam conditions, shift the tune by changing the current on one of the quadrupole magnets slightly, and collect a certain amount of data to do a statistical analysis. By changing the current on the quadrupole magnets the tune should actually shift immediately by a step proportional to the change in power supply current, but both techniques show intermediate tune measurements during the transition. For the SRAM acquisition this is mostly an averaging effect, while for the tune tracker this has an effect that the integrator of the PLL tries to follow the phase. The steepness is in

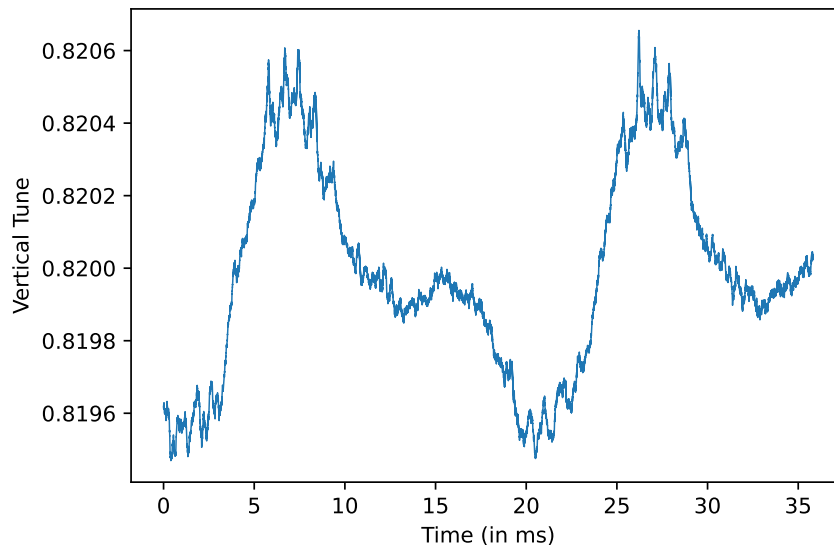
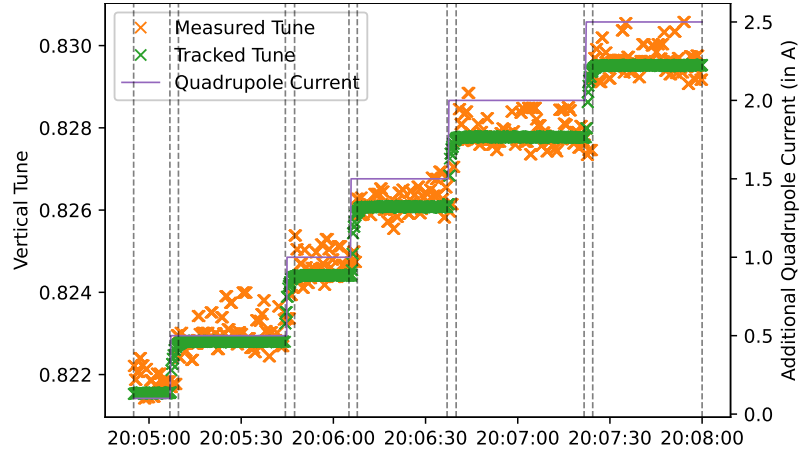


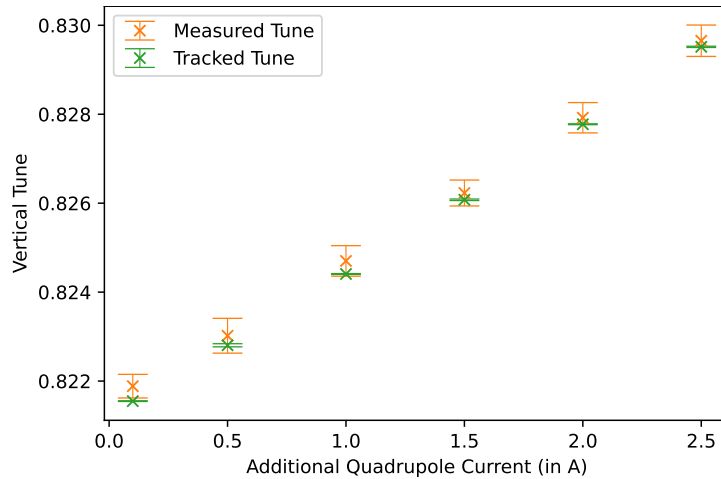
Figure 5.7: Shown is the very fast tune measurement using the phase tracker. The tune is tracked over the whole acquisition length of 36.2 ms showing a characteristic periodicity of around 20 ms or 50 Hz. The reason for this oscillation is most likely the general electric power grid oscillations introduced by the power supplies of the quadrupole magnets.

that case mostly defined by the gain parameter. For this analysis the transition sections were excluded. Figure 5.8 shows the results of this measurement. The tunes acquired via the tune tracker show much less spread with a standard deviation negligible compared to the feedback measurement, but agree very well to the actual measured tunes. This means that the tune tracker can be used for more precise tune measurements and can be configured more flexibly for scenarios where a change in tune is expected, such as the energy ramp, certain measurements, or other special circumstances, such as closing or field ramping of the insertion devices.

Similar to the feedback measurement section, it is also important to consider the validity of the tune tracker measurements and possible impacts on the tune measurement quality. The tune tracker itself also provides a phase difference measurement, which is basically the error of the loop, which it will try to correct during tracking. Using the gain and decimation parameter the error ideally should be minimized for stable beam conditions. Due to sudden shift in tunes or tune changes outside the frequency limit the PLL can also lose its lock, which leads to the frequency readout of the phase tracker running into the set frequency limits. At the same time the error will be large, which both can be used to determine a tracking loss and to discard the tune readouts. An advantage, compared to the feedback approach, is also there is no notch which might be affected by tune instabilities, since the tune tracker already tracks the positive response and an instability will not negatively affect the tune tracker. But more care has to be taken to verify that the bunch selected for tracking is actually a filled bucket and the amplitude level is important, similar to the general excitation method. But if set up correctly, the tune tracker provides very valuable data due to the smaller spread in measurements and faster response to changes.



(a) Plausibility measurement



(b) Mean and standard deviation

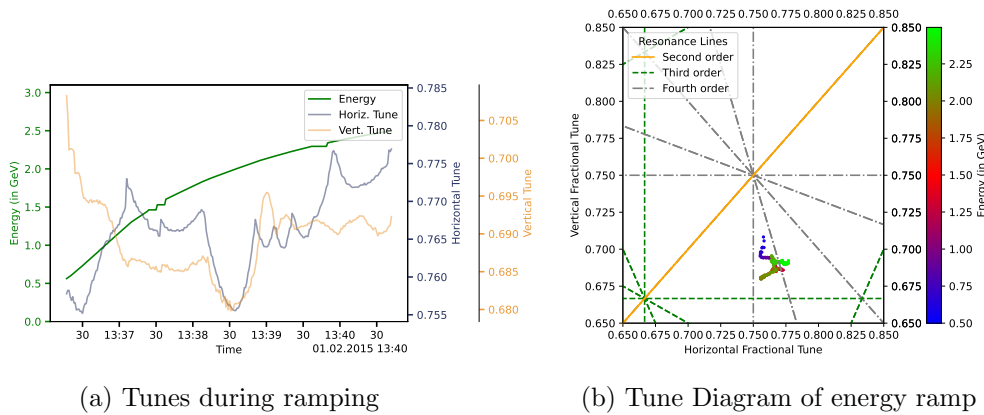
Figure 5.8: Phase tracker plausibility measurement. The tune derived from the phase tracker is compared to the tune measured using the feedback method while artificially adjusting one quadrupole magnet to force a change in tune. (a) shows the full measurement, where the period where the integrator adjusts for each new tune setting is excluded from the statistical evaluation. (b) shows the tracked tune in agreement with the tunes measured with the feedback method and at the same time showing much less fluctuations. The tracked tune is systematically slightly below the measured tune, which can be explained by a slight tune shift due to multi-bunch effects.

## 5.2 Tune Dynamics

The working point of an accelerator – the combination of horizontal and vertical tune – is a parameter which is carefully chosen and often cited as a fixed value. In reality however, due to the characteristic nature of tunes in describing the general optics and state of the accelerator, the tunes vary during operation. This section will take a closer look at the tune dynamics over short and long periods of time.

### 5.2.1 Tune Influences

Many factors can contribute to a variation in tune and might depend on the exact circumstances of how the accelerator is operated. For one, the tunes are typically beam current dependent and therefore change intrinsically [28, p. 18] if the beam current is increased or decreased. At KARA this is noticeable due to the nature of the operation cycle: With a clear separation between the injection process – where the beam current increases – and the operation state – where the beam current decreases. Additionally, KARA also operates in very different current regimes, especially during the *short bunch* operation mode. But the tunes also change regularly directly based on changes of other beam parameters. Here, a distinction into more categories can be made: First, there is the beam optic ramp. During the *optic ramp* all quadrupole families are changed synchronously according to a pre-defined *ramping table*. This happens in parallel during every increase of beam energy, since the focusing effect of the quadrupoles is depending on the beam momentum. But an *optic ramp* can also happen at a fixed energy – for example to change into the *short bunch* operation mode. While a change in overall beam optics also happens between the optics used for injection and the optics used at 2.5 GeV, this is incorporated into the adjustments happening during the energy ramp. The second category of tune changes is due to the operation of the insertion devices. These are typically only active during operation at 2.5 GeV, since they require a optic with small vertical  $\beta$  function. Therefore, after the energy ramp to 2.5 GeV, the insertion devices are activated. Depending on the type of insertion device by either closing a mechanical gap or by increasing the magnetic field – or both. During this phase, the tunes are changing, since the insertion devices have an effect on the optics [30]. Since the effect is local and very specific based on the insertion device, there are typically local corrections in place which try to minimise the effect on the global beam optic. The overall observable change in tune is therefore a combination of the change induced by the insertion device and the effort to compensate this effect. The last category of tune changes is due to a specific - mostly manual - change of a parameter of the accelerator. The two largest contributions to such changes at KARA is either a individual adjustment to one quadrupole family – outside of the optics ramp – or a change to general frequency of the cavities  $f_{\text{RF}}$ . Here again it is useful to distinguish active measurements, such as measurements of the *chromaticity* discussed in Sec. 5.3. If not for a particular measurement, the tune changes due to active measurements are not further discussed. During operation at 2.5 GeV, typically a *beam orbit feedback* is active, which corrects the general beam position – not to be confused with the BBB feedback. Since  $f_{\text{RF}}$  has a large contribution to the horizontal orbit,  $f_{\text{RF}}$  is part of the beam orbit feedback algorithm [31].



(a) Tunes during ramping

(b) Tune Diagram of energy ramp

Figure 5.9: Example for the tunes during energy ramp. The left side shows a typical plot over time for the energy and both tunes, while the plot on the right hand side is a so-called *Tune Diagram*, where the combination of both tunes is shown in the presence of relevant resonances of different order, marked by straight lines of varying color and style. In addition, the change of working points is color-coded along the change in energy according to the color bar on the right, with blue starting at 0.5 GeV. Green corresponds to the energy at 2.5 GeV.

Since the orbit feedback will make many small corrections over the course of many hours, tunes will also change accordingly. The beam orbit feedback is not used in other operation modes – such as the injection or short-bunch operation. Finally, this leaves manual individual changes to  $f_{RF}$  and quadrupoles outside of measurements and orbit feedback. Such changes can happen during the injection process as part of day-to-day optimization, but can also lead to permanent adjustment of the injection parameters. In summary: While there is typically one – or multiple – design working points, the actual tunes during operation are exposed to many circumstances where they will inevitably change.

### 5.2.2 Tune Stability Considerations

It is crucial to keep the tunes away from possible resonances, as discussed in Sec. 2.3.4. Since the working point is a design parameter, this is usually ensured to be the case. But as discussed in the previous section, there might be many additional contributions moving the tunes off the ideal working point. It is therefore often useful to look at the tunes on a so-called *tune diagram* – introduced in Sec. 2.3.4 and Fig. 2.10 – where the combination of both tunes is visualized in the presence of possible resonances of different order. Since the tunes are measured by the BBB feedback system continuously, it is possible to also observe the changing tunes. Figure 5.9 shows an example during an energy ramp at KARA. In this case the working point is color-coded according to the energy of the beam at the time of the measurement, making it possible to not only show the overall change, but also the flow of changes. Important to note is that the tune does not have to be necessarily fixed to the design working point. Therefore, during the *optics ramp* and the insertion device activation process, significant tune changes are happening. It only has to be ensured that potential tune resonances do not occur. Also, most use cases for the beam at KARA are not dependent on any specific working point. To avoid potential tune resonances it is

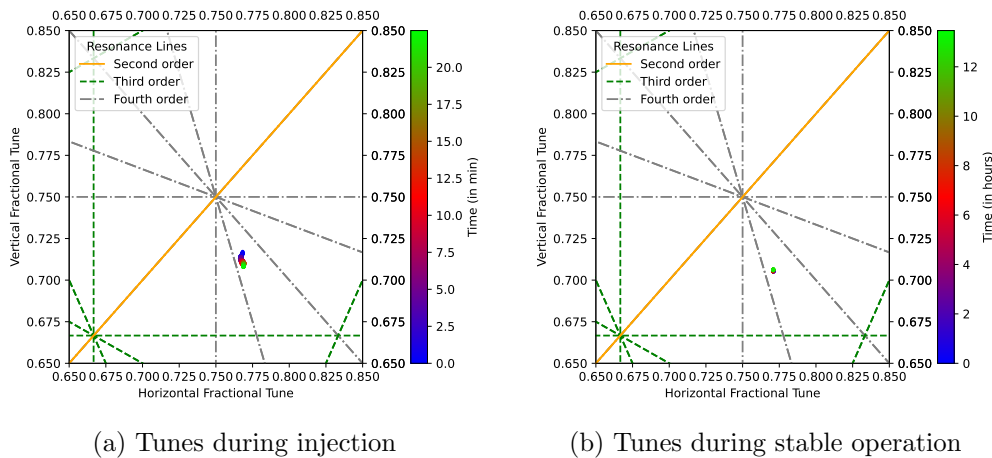


Figure 5.10: Tune variance during injection and beam operation. Shown are the working points over color-coded time range in the case of minutes for the injection in (a) and hours for the beam operation in (b). The major contributions to this variance is the current dependency of the tunes and minor corrections to the optics during beam operation due to beam orbit feedback. Overall the variance is small compared to tune changes during an optics ramp shown in Fig. 5.11.

still often useful to limit the range of changes to certain areas in the tune diagram. For better comparability and as long as not specified explicitly, all tune diagrams shown in this section will show the exact same area and scaling. Although the tunes change dramatically during the energy ramp, the risk of beam losses due to encountering tune resonances is low. This is because the energy ramp is by itself explicitly designed. This designed ramp still needs to be adjusted from time to time, for example if the injection optics is adjusted and therefore the starting point of the energy ramp is different. In direct comparison it is also useful to take a closer look to the – intrinsic – beam current-dependent tune change. Fig. 5.10 shows examples for a typical injection and beam operation. For this, the color-coding of the tune values is based on time, which in both cases translates also to beam current. Of note for the tunes at 2.5 GeV: the time scale here is many hours compared to minutes for the injection. Compared to the changes during energy ramp, the effects of the current-dependent tune shifts are minor. We can therefore safely assume that the danger of encountering resonances due to the current dependency of the tunes is fairly low. Since manual changes and changes due to ramping are larger, the typical design working points are at a safe distance from possible tune resonances. Fig. 5.11 shows two very different energy ramps. The upper tune range shows the situation after a redesign of working point at KARA [17]. This new optic is on the other side of a second-order resonance. Therefore this also required major adjustment to all special optics in use, since crossing the resonance line during an optics ramp would not be possible.

### 5.2.3 Long Term Observation

This section so far has shown examples and discussed the effects on the tunes for various different scenarios. All tune data is provided by the BBB feedback system. As previously

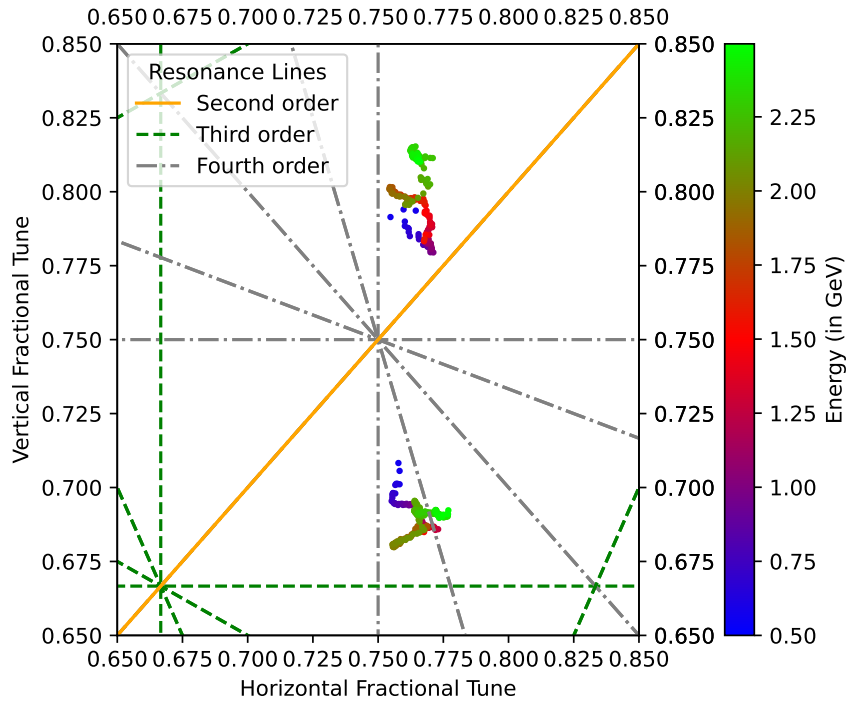


Figure 5.11: Working point during Energy Ramp before and after major optics redesign. Shown are two very different energy ramps. The lower ramp is before and the upper ramp after the major optics re-design at KARA [17]. Notably the new working points are on the other side of the linear coupling resonance, where the  $\nu_x = \nu_y$ .

discussed, the feedback system is able to provide the default tune measurements with up to 2 Hz, continuously and across all different operation modes of KARA. This data is also stored and archived at the same rate. Therefore for both horizontal and vertical tunes, up to 340 000 data points are stored daily. Extrapolating these daily rates over the time, the BBB feedback system in use at KARA leads to around 750 000 000 data points. A deep dive into how the data is stored and how it is retrieved is outside the scope of this chapter, but can be found in Appendix A. Not only the tunes, but also all relevant data points at KARA are stored continuously, creating a vast archive of data. This allows all kind of correlation effects of beam parameters and accelerator configurations to be studied. The challenge lies in how to access and handle this amount of data. Since the data can only be accessed via date and time, but not based on any inter-data relations, this requires the creation of a detailed index for every beam operation cycle. A detailed discussion of why this was necessary and how it was done can be found in Appendix B. Creating this index for historic data was a substantial effort, but the lessons learned during the process are applied to the current environment at KARA, leading to an automatic indexing of current and future beam operation cycles. Due to the characteristic nature of the tunes for describing the state of the accelerator, studying the tunes over large periods of time should lead to better understanding of the changing state of the accelerator. Applying past information to the current state should help in identifying potential issues and consequently improve reliability and stability for beam operation and research opportunities. Due to the many different factors which contribute to the values of the tunes, comparing

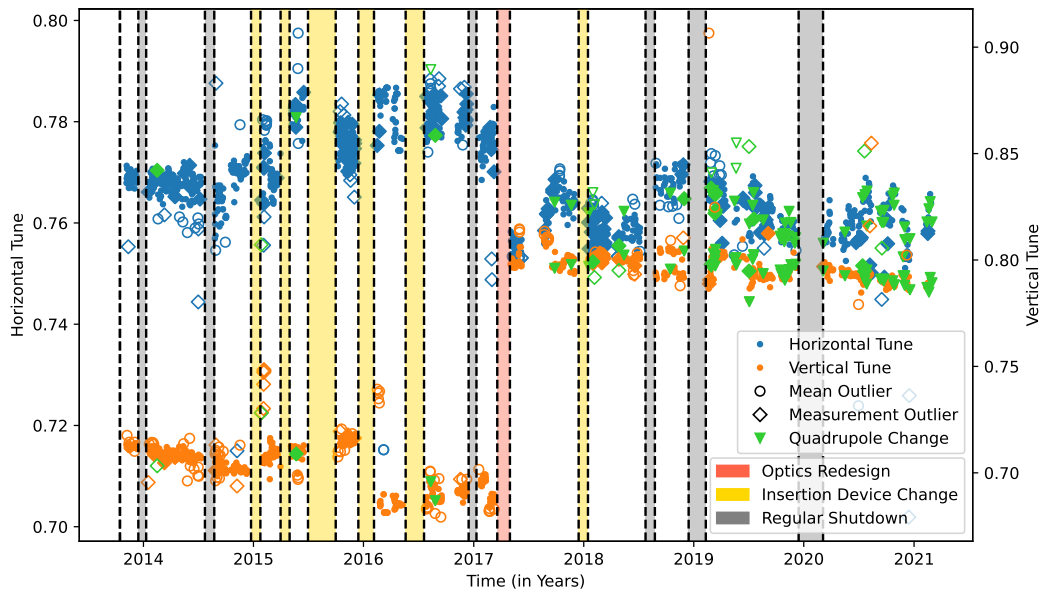


Figure 5.12: Long term overview of tunes during injection. Every data point represents an averaged tune across the same current range. The vertically color-marked sections represent shutdown periods. Yellow sections mark shutdowns which required significant compensation to beam operation typically due to addition or replacement of an insertion device. Grey sections represent maintenance periods. A detailed discussion can be found in the text. Fig. 5.13 shows similar data for operation at 2.5 GeV.

the absolute value of the tunes from now to, for example, a year ago is not helpful. What is helpful however is to be aware of the current tunes and potential differences in the day-to-day operation. If put into the correct context and considering potential influences, this should help in identifying potential issues or possible solutions. Also studying the relative change of tunes around certain time areas is beneficial. At KARA, periods of operation are divided by shutdown periods to perform needed hard- and software maintenance. During these shutdown periods fundamental changes to the structure of the accelerator can also happen – for example the addition of a new insertion device. Due to the technical requirements, but also due to the change in beam dynamics, such a change typically leads to substantial changes in beam stability and also leads to necessary adjustments for the tunes and the optics in general across all operation states. Due to the nature of KARA as a test and development accelerator facility, over the last several years multiple additions and replacements of insertion devices have happened. Fig. 5.12 combines the information of shutdown periods – both for fundamental changes to the accelerator and for maintenance shutdowns – with horizontal and vertical tune data. Every data point represents one of over 1000 injections of a beam operation cycle leading to the default operation at 2.5 GeV. This provides a more stable environment, compared to beam physics studies or accelerator development. Each data point consists of the mean of all tunes measured in the same current regime during injection  $\pm 5$  mA. Two different types of outlier detection have been performed: The first looks into the deviation of tune measurements inside the 10 mA current window, while the second one compares the data point to relevant tune measurements in the same period. The periods are typically defined by the shutdown sec-

tions. There are a couple of reasons as to why tune readout data might not be precise. In general there are three aspects: Firstly, a miss-configuration of tune readout parameters, which includes not adapting the configuration to general adjustments of the accelerator. The second source are unmitigated beam instabilities. The third factor is actual manual changes to the beam parameter, which might effect the tunes. With correlating additional data points most outliers can be accounted for. For example: Injections where an operator changed manually any of the quadrupole fields are marked differently. While typically a quadrupole change does effect both tunes, depending on the quadrupole family, the tune change in one plane is much larger. As seen in the more recent history, this was a much more common occurrence. This indicates that the default optic is not ideal and might need to be adjusted. Clearly visible is also the fundamental change in beam optics [17], with a drastic change in vertical tune. Using similar approach, also the tunes at 2.5 GeV can be studied. The data is shown in Fig. 5.13. Since the tunes are less prone to variations over time – either due to changing beam current or manual intervention – a larger current regime can be used to average the tunes. One of the possible contributions to tune variations which were not included are different filling patterns. Also especially in the recent past, some of the insertion devices either vary their characteristics during the operation cycle or between operation cycles which also effects the tunes. Correlating even more of

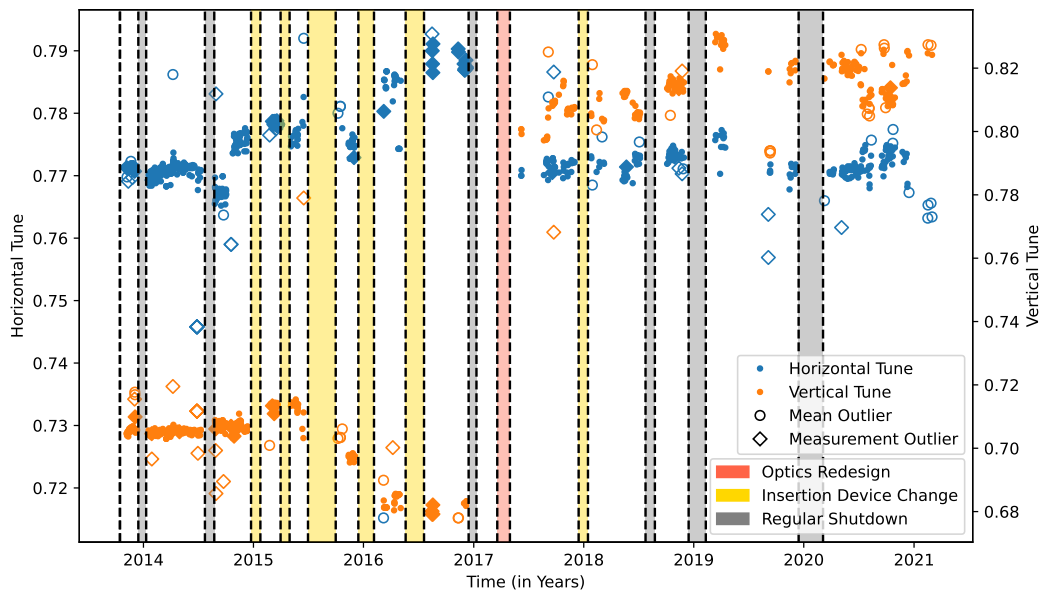


Figure 5.13: Long term overview of tunes during operation. Every data point represents an averaged tune across the same current range. The vertically color-marked sections represent shutdown periods. Yellow sections mark shutdowns which required significant compensation to beam operation, typically due to the addition or replacement of an insertion device. Grey sections represent maintenance periods. A detailed discussion can be found in the text. Fig. 5.12 shows similar data for injections.

the available data helps in classifying outliers to an even finer detail. But looking at the bigger picture there also seems to be quite a lot of room for improving the stability of tune measurements. One approach is considering tunes measured via the phase tracking technique as an alternative tune measurement. But even more important: It seems likely

---

that with more carefully configured tune readout configurations many outliers can even be prevented from happening in the first place. This is also evidenced by the fact that there seems to have been a general trend over many years where the tune readout stability degraded. This might be an effect of the BBB feedback system moving out of focus for possible optimizations due to its nature of continuously running in the background. In addition, the daily operator might be presented with too much data without the necessary context to help to identify sources of tune readout instabilities. The approach and visualizations designed to present the data across this chapter can for the future also be used to automatically classify the readout stability during individual operation cycles, together with providing clear visual feedback to the operator, allowing for corrective actions that would improve the tune readout or the beam stability.

---

### 5.3 Chromaticity Measurements

The chromaticity  $\xi$  of an accelerator describes the energy-dependent focusing errors of the quadrupole magnets, as discussed in Sec. 2.3.5. The chromaticity can be changed by using sextupole magnets which is necessary, since the *natural chromaticity* – the chromaticity without any corrections – is negative and would otherwise lead to instabilities (see Sec. 2.4.5). Due to its effect on damping instabilities, it can therefore also be increased above the necessary threshold of being positive [28, p. 164]. At the same time, high chromaticity values decrease the *dynamic aperture*. It is therefore important to find an appropriate balance, which makes it important to measure the chromaticity. Measuring a change in tune as a function of a change in momentum can be used to determine the chromaticity. Since a change in tunes can be measured for both horizontal and vertical tunes, the horizontal and vertical chromaticity can in consequence be identified. Similar to horizontally and vertically focusing quadrupole magnets, usually also two different types of sextupole magnets are used. Although sextupole magnets introduce non-linear fields and therefore also introduce non-linear coupling between the horizontal and vertical plane, for convenience, these sextupole magnets are labeled as horizontal and vertical sextupole magnets.

#### 5.3.1 Measurement Technique

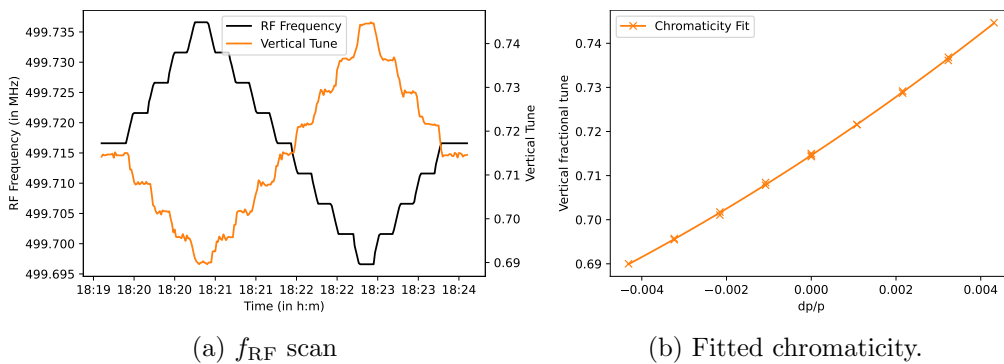


Figure 5.14: Basics of chromaticity measurement. The left plot shows the raw measurement with changing the  $f_{\text{RF}}$  and the effect on the tune  $\nu$ . For each step the  $\nu$  is measured after a defined waiting time. Measurements are taken on each step, resulting in multiple measurements per  $f_{\text{RF}}$ . On the right  $\nu$  is plotted over the relative change in momentum  $dp/p$ . The chromaticity can be estimated by a fit to the data.

To be able to measure the change in tunes over the change in energy, the momentum needs to be changed. While a change in energy is routinely done at KARA during the energy ramp from injection energy to the final operation energy, changing the strength of the dipole magnets is not a viable way of measuring the chromaticity. For one, changing the dipole magnets will affect the optics in general, it generates a rather large energy shift and is typically not reversible due to hysteresis effects of the magnets. Typically, a relative change of the momentum  $\frac{dp}{p}$  of three to five ‰ is enough. This can be achieved by changing the main RF frequency  $f_{\text{RF}}$ , since it will change the path length and therefore

Message ID: 650 Entry time: Sat, 07.07.2018 - 16:24	
Fill Number:	6689
Energy:	2.5
Beam Current:	11.01
Horz. Chroma:	2.957
Vert. Chroma:	2.178
MCF:	0.0095
RF Frequency:	499.7226
RF Steps:	[0 4 8 12 8 4 0 -4 -8 -12 -8 -4 0]
Wait Time:	10
Feedback Gain:	3   3   2
Feedback Avg.:	3   1   3
Feedback Pattern:	1:184   1:184   1:184
Measurement PC:	ankasr-matlab
Data:	/home/ankaop/controlsystemshare/MatlabMiddleLayerData/Storage
Attachment 1:	Chro_2018-07-07_16-22-29.png 79 kB   Hide   Hide all

Figure 5.15: Electronic logbook entry. Every measurement automatically creates an entry into the electronic logbook with the most relevant general beam parameters, such as the fill number, beam current, beam energy, but also parameters specific to the measurement, such as the wait time parameter, feedback configuration, and RF vector. A plot of the data is also attached.

the momentum, as discussed in Sec. 2.3.3. The relation between a change in  $f_{\text{RF}}$  and change of momentum is then only defined by the *momentum compaction factor*  $\alpha_c$ :

$$\frac{\Delta f_{\text{RF}}}{f_{\text{RF}}} = -\alpha_c \frac{\Delta p}{p}. \quad (5.4)$$

The chromaticity  $\xi$  can therefore also be defined as:

$$\xi = \frac{\Delta \nu}{\Delta p/p} = -\alpha_c \frac{\Delta \nu}{\Delta f_{\text{RF}}/f_{\text{RF}}}. \quad (5.5)$$

The BBB feedback system is able to measure the tunes and to make available the values online to the general control system, which made it possible to set up routines to automatically measure the chromaticity. An example of a chromaticity measurement is shown in Fig. 5.14. For the chromaticity measurements,  $\alpha_c$  is based on simulations of the accelerator using the *Accelerator Toolbox* of *MATLAB* © [32]. The chromaticity is obtained by a polynomial fit on the measured data. While the chromaticity therefore has also higher order components, in context of this thesis only the first – linear – order is discussed. Since the only measured values are the tunes, the context in which the tunes are acquired is essential (which was discussed previously in Sec. 5.1). Therefore for a successful measurement several constraints have to be considered. First, the BBB feedback must be active. Secondly, the range of the tune change must be inside the limits of the configured feedback filter (Sec. 4.2.2) if using *feedback measurement* detection, or inside the span of the applied excitation if using *excitation measurement*.

Thirdly, the limits of the automatic peak finder search have to match the range of tune changes. Fourthly, after the change in  $f_{\text{RF}}$  and before taking the tune measurement, a waiting time has to be defined to compensate for the averaging in the tune measurement.

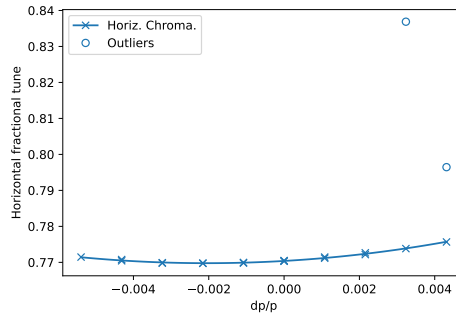


Figure 5.16: Outlier detection. Due to many different factors involving the beam conditions and configuration of the tune readout, wrong tune measurements are possible. An outlier detection was therefore implemented while analyzing the measurement data, using the *RANSAC* machine learning algorithm implemented in the *scikit-learn* Python module [30, 33].

Fifthly, changing the  $f_{\text{RF}}$  suddenly and in large steps might disturb the beam and other diagnostic equipment. For measurements at 2.5 GeV – within the default optics and well established BBB feedback settings – this typically boils down to making sure the measured tune notches in the spectrum are large enough for the overall beam current and defining the proper wait time for each step of  $f_{\text{RF}}$ . Additionally to the measurement time, the  $f_{\text{RF}}$  step size and the amount of steps can be defined. The rate at which the RF frequency can be changed is technically limited. Typically, the  $f_{\text{RF}}$  should be scanned in both directions and also have to be reset to the original value after the measurement. While a routine for the basic measurement approach and basic fitting was already present due to [34], this was modified severely towards a higher degree of automation and flexibility. For example, based on the given parameters of the wait time, step size, and number of steps, a measurement vector is calculated to measure the tunes multiple times during the scan, which increases the statistics and tries to minimize the time spent on changing the RF frequency. Therefore a measurement with four steps results in a scan with 13 measurement points, also visible in Figure 5.14 which shows such the raw measurement scan. The data set of each measurement is not only stored, but also summarized and documented in an electronic logbook, making it possible to search for certain beam criteria. An example entry is shown in Fig. 5.15. Having to look into hundreds of automated measurements makes it important to have robust analysis tools which can detect and reject – or if possible – handle flawed measurements. To achieve this, a module in Python has been developed. This module makes sure that the raw measurement data is consistent, it compares the results of two different implementations of a polynomial fit and – as a final sanity check – warns if the estimated chromaticity is outside of realistic boundary conditions for measurements at KARA. Additionally, it will try to detect outliers in the measured tune values, since typically a couple of outliers can be compensated due to the amount of measured values. This outlier detection was originally implemented in a thesis of a colleague [30]. The outlier detection is based on the *RANSAC* machine learning algorithm and its implementation is in the *scikit-learn* Python module [33]. An example of a successful outlier detection is shown in Fig. 5.16. Based on the consideration of

systematic errors in tune measurements, as discussed in Sec. 5.1, the tune error is also taken into account, but for most measurements it is negligible compared to the tune steps induced by the change in momentum.

### 5.3.2 Measurement Stability

Overall there are more than 1000 chromaticity measurements done at KARA which are available for analysis. Since the chromaticity measurement is a measurement which has to be actively carried out, most of these measurements measure the chromaticity for special conditions, such as a change in the field strength of sextupoles, for exploring new optics, or other circumstances which might effect the chromaticity. In contrast to the tune studies, it is therefore not as useful to look into all chromaticity measurements over time, but rather to look at certain studies by themselves. One important aspect is the long term stability of the measurement approach itself. A script was set up to measure 100 consecutive chromaticity scans, which took around six hours to complete. Over this time range the beam current decayed by around 10 mA. On the next day the same measurement, again with 100 scans, was repeated, but this time some of the available insertion devices were closed. As discussed in the previous section, the insertion devices affect the tunes. The results in Fig. 5.17 also show an effect of the insertion devices on the chromaticity. Additionally, this measurement demonstrates that the chromaticity measurement works reliably: Over all of the scan periods not one single outlier was detected. It also shows that the spread of chromaticity estimations based on the fits is small compared to external influences on the chromaticity. A deeper discussion on the effects of insertion devices on chromaticity is outside the scope of this thesis, but can be found in [30].

### 5.3.3 Operational Chromaticity

At the typical operation regime – at 2.5 GeV – the chromaticity is typically chosen to be at specific values so to balance the improved stability brought about by higher chromaticity without introducing beam quality limiting effects due to the reduced dynamic aperture. In the course of the general re-design of the optics, discussed in the previous section, the chromaticity was also adjusted. Figure 5.18 shows the previously used chromaticity and the chromaticity in use now. While especially the vertical chromaticity was chosen to be rather large at  $\xi_v \approx 6$  to reduce vertical instabilities, the new optics was able to reduce both horizontal and vertical chromaticity to the ideal small, but slightly positive values close to 1 [17]. This was enabled by the improved beam stability provided by the BBB feedback system.

### 5.3.4 Improved Tune Data Source

An alternative approach to the normal tune readout provided by the BBB feedback system is using the phase tracking approach. As discussed in Sec. 5.1, acquiring the tunes via phase tracking can be more precise. Also the phase tracker can be set up to adapt to changes in tunes more quickly than the approach via the SRAM acquisition engine. The wait time used for chromaticity measurements has to take into account the time the RF

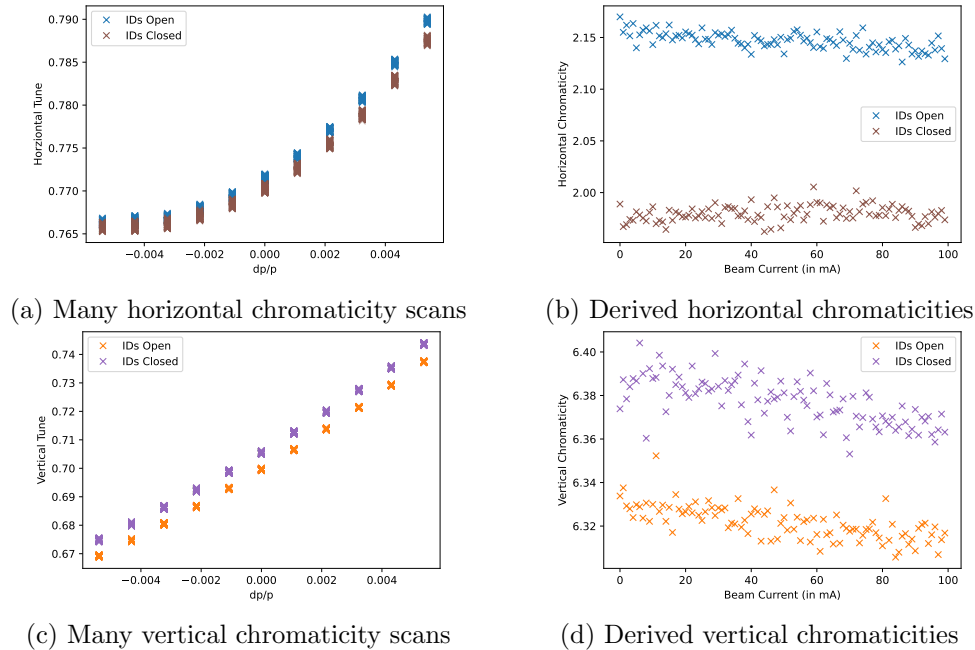


Figure 5.17: Measurement routine stability and influence of insertion devices. The figures on the left show in each color 100 consecutive chromaticity measurements. The second color in each diagram shows another 100 chromaticity measurements under the influence of insertion devices. In the plots on the right every data point corresponds to one chromaticity scan on the left, showing that typical influences on the chromaticity are larger than typical statistical variations in the chromaticity estimation. Additionally a minor current dependency on the chromaticity is visible. A more in depth discussion on the effects of insertion devices is found in [30].

needs to change due to the limited rate of  $\frac{\Delta f_{\max}}{\Delta t} = 1 \frac{\text{kHz}}{\text{s}}$  and the time needed, once the RF has reached its destination for the averaging in the tune readout, to catch up. If the tune readout can be now set up to be as fast as the RF is allowed to change, the wait time parameter becomes mostly obsolete. This allows either the measurement time needed for one chromaticity scan to be reduced or also allow the tunes along the frequency change to be measured much more often, without the need to wait for the averaging to settle. Additionally, this significantly improves the measurement data in scenarios with a low number of bunches. An applied chromaticity measurement making use of the phase tracker is shown in context of the natural chromaticity measurement discussed in the next section.

### 5.3.5 Natural Chromaticity

The natural chromaticity is defined as the chromaticity of an accelerator without the presence of non-linear higher order magnetic fields. Typically it is not possible to operate an accelerator at natural chromaticity and other techniques exist to indirectly estimate the natural chromaticity [28]. At KARA, two families of sextupole magnets exist. The strength of the sextupole fields can easily be reduced by reducing the current supplied to these two magnet families. Since sextupole fields introduce non-linear dynamics (as discussed in Sec.

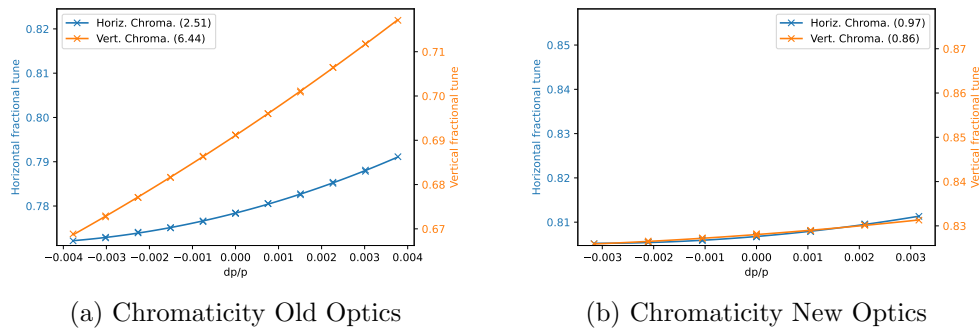


Figure 5.18: Comparison of chromaticities in use before and after the optics redesign [17]. Due to the improved stability provided by the BBB feedback system, the chromaticities could be reduced to the ideal low positive values without negative influences due to possible beam instabilities.

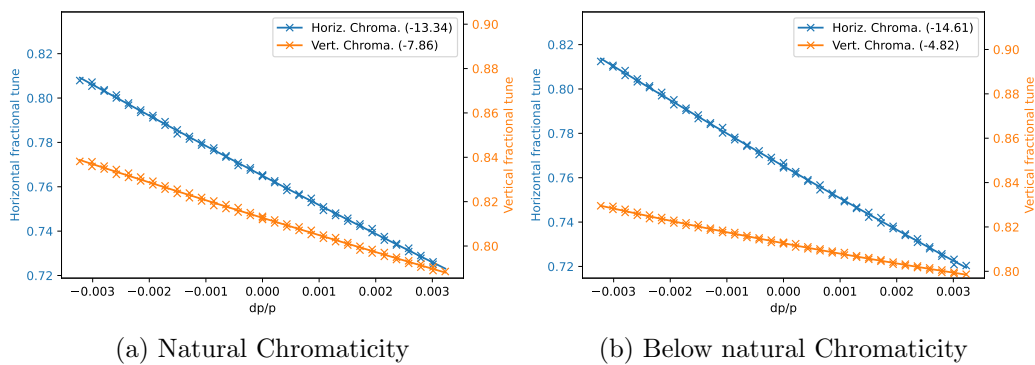


Figure 5.19: Measured natural chromaticity using improved tune measurements. The left diagram shows the measured natural chromaticity in the absence of sextupole fields. The right hand side shows a horizontal chromaticity even below the natural chromaticity in the presence of a small field in the vertical sextupole family only.

2.1.1) an incremental approach has been taken step-by-step and alternating between the families so to reduce the strength of the sextupole fields while measuring the chromaticity at each field configuration. The full range of possible sextupole fields was scanned and the result can be seen in Fig. 5.20.

Fig. 5.19 presents explicitly two chromaticity scans – now also making use of the phase tracker tune measurement. One shows the measured natural chromaticity in the total absence of sextupole fields. The measured natural chromaticities are:

$$\xi_{\text{natural, horizontal}} = -13.32 \pm 0.01, \quad (5.6)$$

$$\xi_{\text{natural, vertical}} = -7.86 \pm 0.01. \quad (5.7)$$

While the horizontal natural chromaticity is similar to the theoretical prediction in [17], the measured vertical natural chromaticity is significantly higher at  $-8$  compared to the  $-13$ . To calculate the chromaticity, the momentum compaction factor  $\alpha_c$  is used. As previously mentioned, this value is not measured but taken from theoretical predictions, which could point to one possible explanation for the difference between the measured and simulated natural chromaticity values. The measurement on the right shows a horizontal

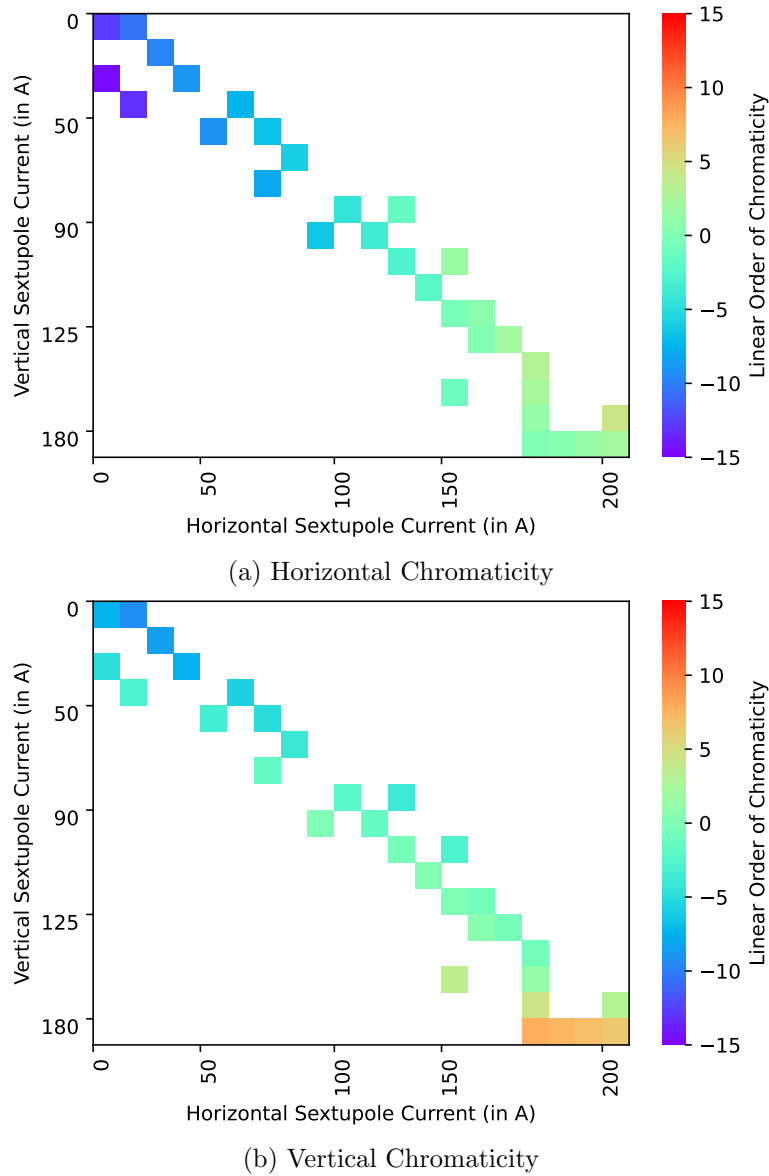


Figure 5.20: Chromaticity mapping from highest to lowest chromaticities. For each diagram the chromaticity value is color-coded according to the color bar from high chromaticity (red) to low chromaticity (purple). Horizontal axis represents the current of the horizontal sextupole family and vertical axis for the vertical sextupole family. (a) shows the results for the horizontal chromaticity and (b) for the vertical. While the vertical chromaticity can reach higher, the horizontal chromaticity can reach lower values.

chromaticity even below the measured natural chromaticity. In this case, the vertical sextupole field was slightly above 0.

### 5.3.6 Future Improvements

The implementation of the BBB feedback system allowed automated measurement routines to be used to measure the chromaticity. The measurement routine was altered and improved many times, for example by adding automatic entries to the electronic logbook or by implementing the phase tracking measurements. Other aspects are fundamental to the current iteration and cannot easily be changed. For example, it is very important that the *wait time* parameter is carefully chosen by the operator, otherwise measuring the tunes might not happen at the correct time and could result in skewed chromaticity values. But with the data available nowadays in the control system, the minimum wait time can be automatically be determined by: First, waiting until the limited frequency rate change is done. Secondly, taking into account the configuration parameters of the BBB acquisition engine – such as the averaging – and calculating the required time for the averaging to settle. Thirdly, the tunes can now be measured for a period of time, adding statistics and error estimation directly to the raw measurement data. Such deep and fundamental changes are not feasible without a full re-implementation of the measurement routine. This approach can also be used for a better integration into the control system user interface in general, in addition to other optimization. All of this will help improve the reliability and ease of use of chromaticity measurements.

## 5.4 Tune Shift Due to Resistive-Wall Impedance

The impedance in an accelerator is the result of wakefields generated by the interaction of rapidly changing electromagnetic fields with the environment. It was briefly discussed in Sec. 2.4.3. In this section only the *resistive-wall* impedance will be looked at. The main contribution to this impedance is the structure of the vacuum chamber both with regard to geometry and conductivity. Commonly, the impedance can be modeled by broadband resonators. Using this model, a linear frequency shift over beam current is expected [35]. This frequency shift is nothing else than a current-dependent shift of the tunes  $\frac{\Delta\nu}{\Delta I}$ . Potential sources which induce a tune shift were also previously discussed in Sec.5.2. In the absence of other contributions which effect the tune, the slope of the current-dependent tune shift is directly correlated to the resistive-wall impedance:

$$Z \propto \frac{\Delta\nu}{I_{\text{bunch}}}. \quad (5.8)$$

### 5.4.1 Prior Work

The current-dependent tune shift at KARA was previously investigated in [35] and [36], but is also of interest for other accelerators [37]. The basic measurement approach is shown in Fig. 5.21 and consists of a linear fit of tune change over the beam current change. To

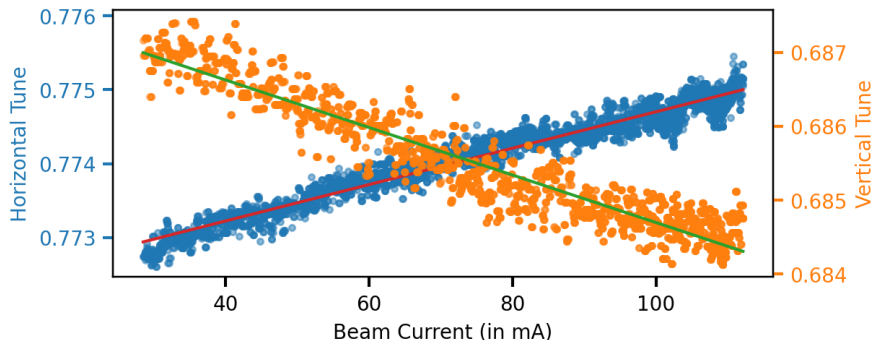


Figure 5.21: Example of current-dependent tune shift. Both the horizontal (blue) and vertical (orange) tune shifts are shown including the linear fit. The tunes were measured with the SRAM engine of the BBB feedback system. The fit values for the slopes are listed in Tab. 5.3.

fully calculate the impedance, additional parameters, such as the bunch length and the momentum compaction factor  $\alpha_c$ , is required [35]. Since this section focuses mostly on the characteristics of the tune shift and comparing tune shifts for different scenarios the actual impedance is not calculated. Table 5.3 shows the values from [35] and the example measurement in Fig. 5.21: The raw numbers are quite different, but at the same time many

Table 5.3: Example of slope of measured tune shifts.

Year	$\frac{\Delta\nu_x}{\Delta I} \frac{1}{A}$	$\frac{\Delta\nu_y}{\Delta I} \frac{1}{A}$
2004	$-(0.06 \pm 0.06)$	$-(0.55 \pm 0.06)$
2019	$0.0246 \pm 0.0001$	$-(0.0322 \pm 0.0002)$

years of changes to the accelerator have also happened. The slope of the tune change in vertical direction got larger, which is consistent with reducing the vertical chamber height, which can also be seen in Tab. 5.4. To be able to compare impedance measurements with each other, first potential influences in regard to the measurement approach have to be discussed. Also the KARA vacuum chamber is important to consider. It was discussed in Sec. 3.2. As is typical for an electron storage ring, it is relatively flat, with the basic dimensions in width of 76 mm and height of 32 mm. With such a chamber design, a smaller tune shift is expected for the horizontal tune then for the vertical tune [38].

#### 5.4.2 Dynamic Contributions

At KARA the effective vacuum chamber height which the beam experiences can be changed during operation. One contribution to changes in the vacuum structure are by closing in-vacuum gaps of insertion devices. As listed in Tab. 3.3 currently two insertion devices are installed with a movable gap: The *X-Spec* and *SCU20* insertion device. The exact details of the insertion devices do not matter for now, only the fact that the effective vacuum structure that the beam experiences will be different, if these devices are in operation. Another source for adjusting the effective vacuum chamber are so-called *scrapers*. These

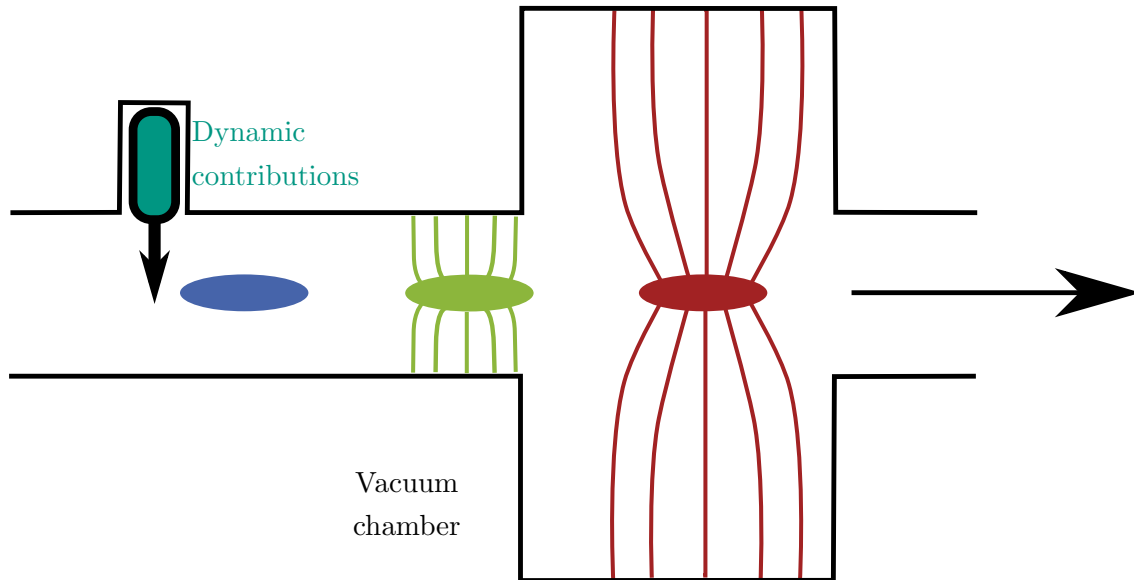


Figure 5.22: Visualization of dynamic contributions. In addition to the wake fields generated by the vacuum chamber, *dynamic contributions* can change to the effective vacuum structure the bunches experience. More details were discussed in Sec. 2.4.3.

are typically cylindrical rods which can be moved in and out of the effective travel path of the beam. At KARA horizontal and vertical scrapers are available, while for this section only the vertical scraper was used. Similar to the insertion devices, here, the scraper is used in a binary state of either in or out.

The measurement approach is then straightforward: Measure the current-dependent tune shift for various configurations of the dynamic contributions to the effective vacuum chamber. Figure 5.23 shows such a measurement using the default tune measurement of the BBB feedback system using the SRAM acquisition engine, which was discussed in detail in Sec. 5.1. The resolution of the tune measurement is close at the limit of the SRAM engine. The tune shift was measured for the four different scenarios: no dynamic contribution, X-Spec closed, SCU20 closed, or scraper moved in. A difference in slope especially in the vertical plane for the scraper measurement is visible. The approach can be improved by using the phase tracker to measure the tunes instead of the SRAM acquisition engine. The same measurement, but with the different tune measurement is shown in Fig 5.24. Table 5.4 shows the exact fit values. With the more precise tune measurement, there also seems to exist a contribution which does not fit to the simple linear approach in tune shift. This is visible around the same current levels on all otherwise separate measurements. This might indicate an influence which affects the effective impedance or an systematic influence introduced by the measurement itself.

Important to remember here is that the SRAM measurement averages over all bunches, whereas the phase tracker only measures the tune of one individual bunch. This becomes apparent if two measurements with the same impedance configuration but different filling pattern is compared. Figure 5.25 shows such a measurement, where the two different fills have a different number of bunches by a factor of three. This means that for the same overall beam current, for one fill each bunch has about three times the bunch charge. This

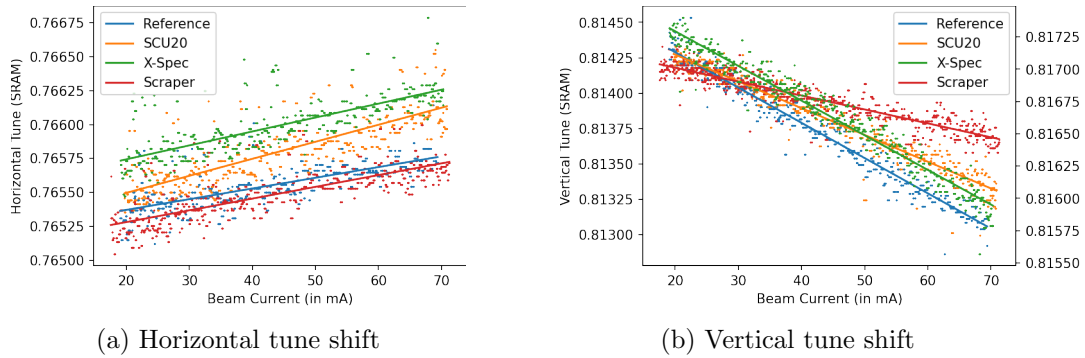


Figure 5.23: Tune shift in the presence of different dynamic contributions to the impedance budget. Each color represents a different configuration of the possible contributions to the impedance budget. The tunes were measured with the SRAM acquisition engine of the BBB feedback system. The measurement spread is relatively large, since the measured effect is close to the measurement resolution of the SRAM engine. The same measurements with the phase tracker tune measurement can be seen in Fig. 5.24.

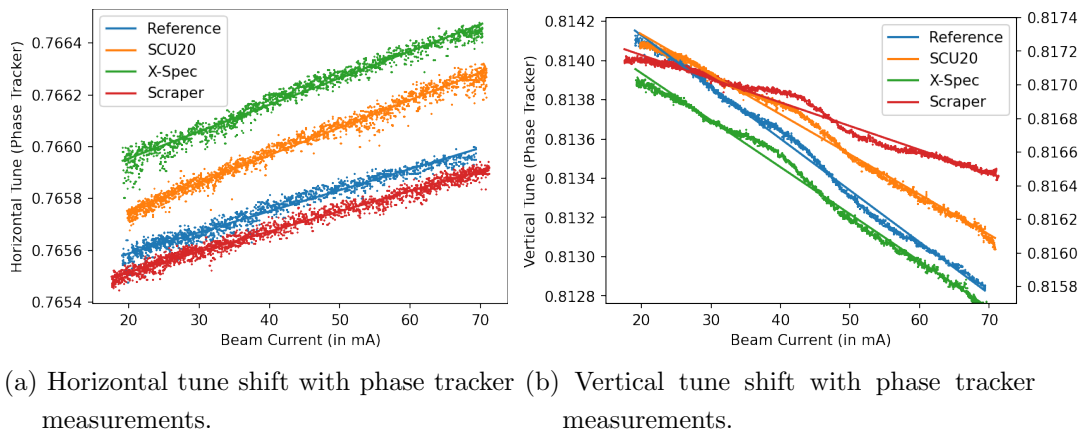


Figure 5.24: Tune shift in the presence of different dynamic contributions to the impedance budget. Similar to Fig. 5.23, this shows the effect of different contributions by insertion devices and a scraper. The tune data is measured with much higher precision using the phase tracker technique. Since the green line of X-Spec introduces a offset this line is plotted over its own vertical axis on the right hand side. The different offsets are introduced due to the absolute tune shifts introduced due to the insertion devices.

Table 5.4: Measured slopes of tune shifts for dynamic vacuum contributions.

Contribution	Horizontal tune shift slope (in $\frac{1}{\text{A}} \cdot 10^{-2}$ )	Vertical tune shift slope (in $\frac{1}{\text{A}} \cdot 10^{-2}$ )
Reference	$0.815 \pm 0.003$	$-2.633 \pm 0.003$
SCU20	$1.065 \pm 0.002$	$-2.042 \pm 0.002$
X-Spec	$1.034 \pm 0.003$	$-2.792 \pm 0.004$
Scraper	$0.78 \pm 0.002$	$-1.207 \pm 0.002$

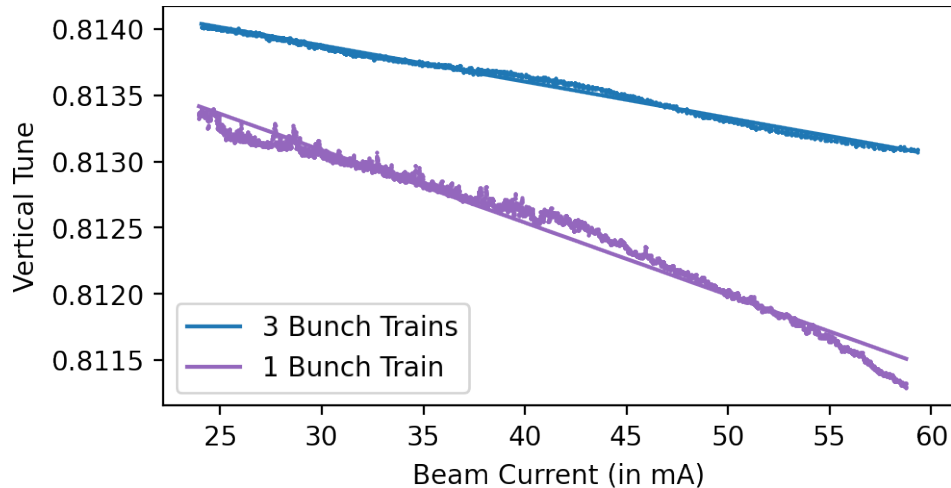


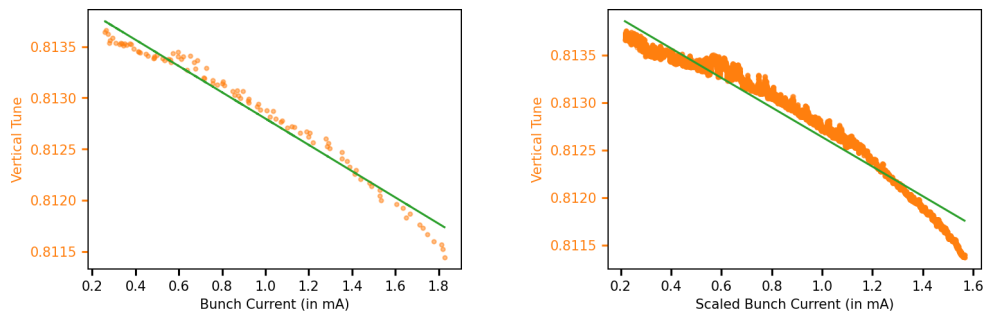
Figure 5.25: Difference in shift based on filling pattern. The colors show a different beam operation cycle with a different filling pattern, but the same overall beam current. The purple measurement only has a third of the amount of bunches compared to the blue measurement. This underlines the importance of scaling the tune shift to bunch current.

is also why Equation 5.8 already states the relation of the tune shift to the bunch current, not the overall beam current.

At KARA, a measurement setup exists to measure the exact bunch currents in a multi-bunch environment. This setup will be discussed more closely in the following chapter. Important to note for now is that the bunch current measurement is not running continuously due to technical constraints of the measurement setup. Therefore, if not measured explicitly, the exact bunch current distribution is not known. What is typically known is roughly the number of bunches since the number of bunch trains is a setting the operator has control over. The question is therefore if for a multi-bunch measurement the beam current can be scaled by the number of bunches to estimate the slope of the tune shift over the single-bunch current. Figure 5.26 compares the exact bunch current measurement of the tune shift with the approach of scaling the beam current by the total number of bunches present. Table 5.5 shows the fit result of Fig. 5.26. Based on these results it seems feasible to scale the beam current by the number of bunches, at least as long as the bunch current distribution along the filling pattern is roughly the same, even if the exact bunch current distribution is not available. Outside of special operations this is typically the case at KARA.

Table 5.5: Tune shifts with scaled and measured single bunch current.

	Vertical tune shift (in $\frac{1}{\lambda}$ )
Measured bunch current	$-1.30 \pm 0.20$
Scaled bunch current	$-1.55 \pm 0.03$



(a) Exact measurement of bunch current      (b) Scaled bunch current based on number of bunches

Figure 5.26: Tune shift over measured and scaled single bunch current using phase tracker.

The left figure shows the tune shift using the measured single-bunch current. The plot on the right shows the same tune shift but for the total beam current scaled by the number of bunches to estimate the single bunch current instead. In the first order, both approaches result in fairly similar results listed in Table 5.5. This allows to scale the tune shifts to single bunch currents in situations where exact bunch current measurements are not available.

### 5.4.3 Evolution of Tune Shifts

With the ability to determine the current-dependent tune shift and in combination with the continuously archived measured tune data, it should be possible to estimate the impedance based on historic archived data. At least in theory, each beam cycle should provide two opportunities to determine the impedance: during the injection process at 0.5 GeV and during the beam operation at 2.5 GeV. In practice however, there are some challenges involved in this approach. First of all, the tune readout has to be stable and the tunes should stay constant apart from the current-dependent shift. This already rules out each beam operation cycle at 2.5 GeV, since in general the orbit is automatically stabilized, which involves changing the main cavity frequency  $f_{RF}$ . As discussed in Sec. 5.2 this introduces non-current-dependent tune shifts. Therefore, trying to estimate the impedance based on archived the tune shifts is only possible with tune data during the injection process. Since the beam is intrinsically less stable during injection, the tune readout might also not be as precise as compared to some of the measurements shown previously. On the other side, the current-dependent tune shift also scales favorably with lower energies [35].

But as discussed in Sec. 5.2, there are a range of influences which can disturb a current-dependent tune shift measurement. Automatically determining suitable injection cycles turns out to be challenging. Figure 5.27 shows some manually selected injection cycles

---

over a time span of multiple years. Since all figures are scaled to the same relative axis, some differences in slope can be seen. Which of those differences can actually be attributed to real changes in the impedance would need closer investigation on a case-by-case basis to take into account other possible contributions such as the filling pattern as shown previously in Fig. 5.25. Systematically investigating the dynamic contributions in the whole range of beam parameters available at KARA should provide a clearer picture of how sensitive such an approach could be.

#### 5.4.4 Conclusion

The important message to take from this look at the slopes of tune shifts are: The BBB feedback system can provide very precise tune measurements to systematically study dynamic contributions to the impedance budget of the accelerator. Taking additional data into account – such as the filling structure of the beam or potential manual changes the beam optics it should be possible to estimate the impedance also on historic archived data, which can then be put into context of actual physical changes in the vacuum structure.

---

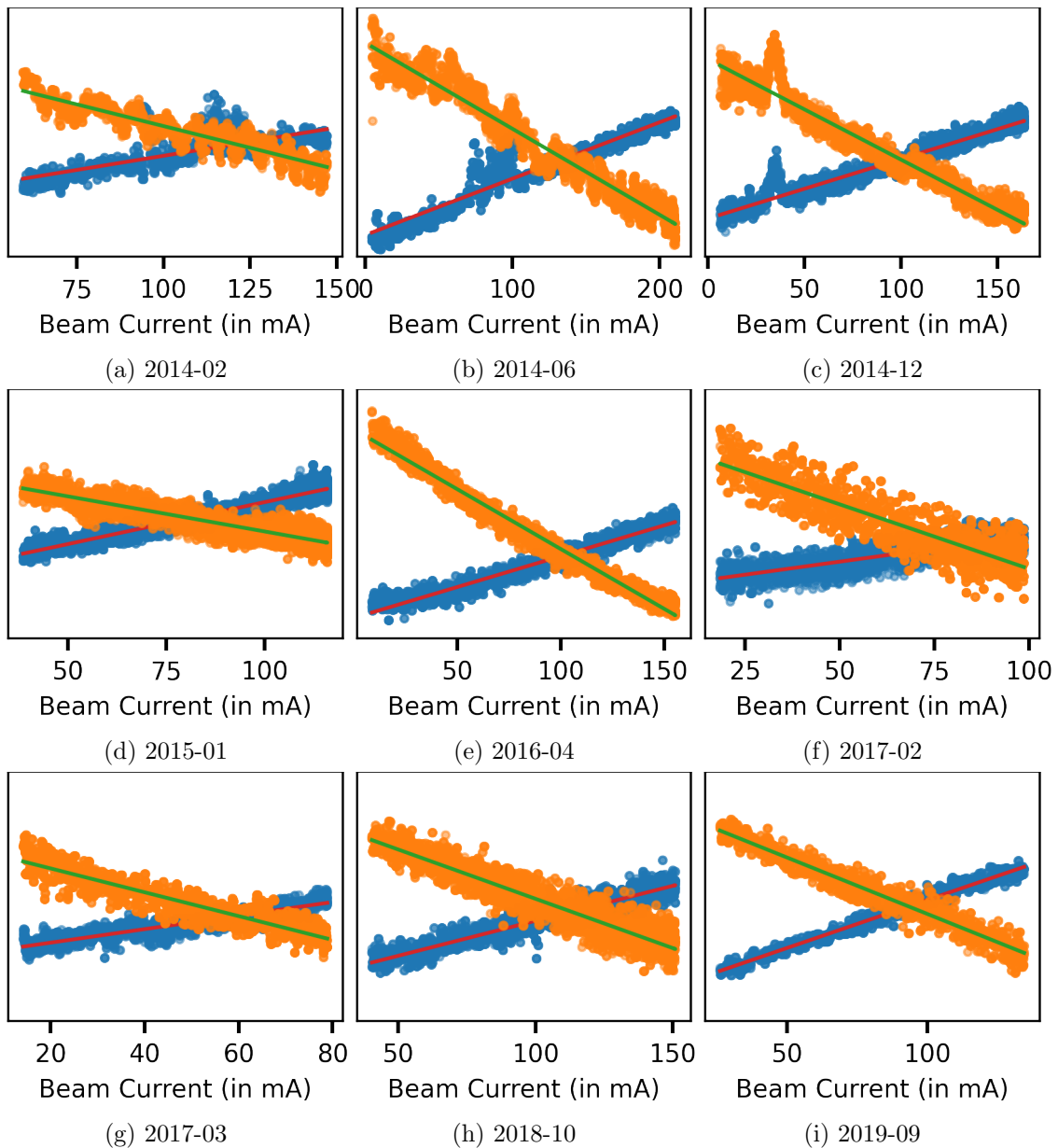


Figure 5.27: Examples of current dependent-tune shifts based on archived data across multiple years. Each figure shows both the horizontal and vertical tune shift over current including the fit. Also, all figures use the same relative scaling of the vertical axes, making the slopes of the fits directly comparable. While the horizontal tune shift looks fairly stable, the vertical tune shift shows some variations. Closer investigations regarding the beam configuration, such as the filling pattern, are required to reliably estimate the impedance.

## 6. Beam Dynamics

The beam dynamics chapter will discuss measurements which involve active manipulation of the beam on the bunch level. The BBB feedback system offers data acquisition capabilities for measuring such effects and also allowing manipulation of individual bunches. The first section will focus on such filling pattern manipulations. Since longitudinal and transverse beam motions have fundamental differences, it is often useful to discuss them separately. First the transverse beam damping under the effect of the feedback system will be discussed as well as benefits to the overall beam operation in regards to beam lifetime and reliability. One particular example of improving the injection efficiency is discussed afterwards making use of driven bunch lengthening using the excitation created by the feedback system. The last section will focus on longitudinal Eigenmode studies and present an approach to systematically study the strength of modes by changing the effect of higher order mode (HOM) inside the RF cavities. This requires a sophisticated setup and data processing chain to allow for the measurement and analysis large amount of data sets.

### 6.1 Filling Pattern Manipulation

One important aspect which the BBB feedback system can provide is the ability to influence the filling pattern of the accelerator, where the filling pattern is the name given to the structure of filled and empty buckets. Due to the periodicity of a circular accelerator even subtle changes in the filling pattern might result in noticeably different behaviour due to the high revolution frequency. KARA has a harmonic number  $h$  of 184. Therefore up to 184 bunches can potentially be filled in the storage ring. The basic filling pattern is mostly defined by the pre-accelerators of KARA, which was discussed in Chapter 3. The whole injection process can be slightly delayed compared to the fixed revolution clock allowing a different section of the filling pattern to be filled with a bunch train. Delaying the injection of a second train by exactly the length of the first train will create a filling pattern with basically one long bunch train defined by the length of both trains. In addition to the default multi-bunch injection scheme, the electron source used to inject into KARA

---

also provides an option for a single-bunch operation mode [4]. Since successfully guiding a single bunch from the source to the storage ring needs substantial adjustments to the magnetic layout of the injector, typically single and multi bunch injections are not used at the same time for one injection cycle. The single bunch operation mode is of particular interest for certain studies due to the following reasons. For one, effects due to multi-bunch interactions are not present. Additionally, the data acquisition requirements for consecutive measurements are significantly reduced. Some measurements are also susceptible to heating damage due to beam loading in a multi-bunch fill [39]. The overall flexibility with regard to the filling pattern therefore comes down to the ability to create gaps between bunch train positions, the overall number of trains, and the ability to inject one singular bunch. Filling pattern dependent measurements also require the precise measurement of the current distribution of all filled bunches. At KARA it is possible to measure the filling pattern using the time-correlated single photon counting method to achieve precise filling pattern measurements [40].

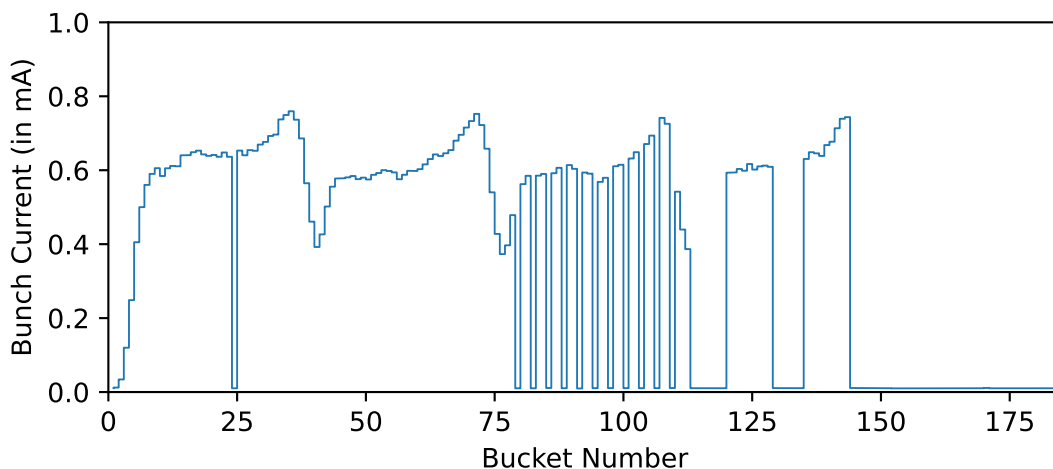


Figure 6.1: Example of a filling pattern created with bunch cleaning. In the first section - also called *bunch train* - the bunch number 25 was removed without effecting any neighboring bunches. In the third train every third bunch was removed. In the last section a group of bunches was isolated from neighboring bunches. Bunch cleaning in general allows therefore for the creation of any given pattern by removing bunches.

### 6.1.1 Bunch Cleaning

The BBB feedback system is capable of exciting any given frequency on any given bunch pattern. In Chapter 5 it was shown that the bunches will show a strong response around the resonance frequency even with small excitation amplitudes. Increasing the excitation amplitude while keeping a narrow frequency span of less than 1 kHz will force bunches outside of the acceptance criteria required for stable periodic bunch motion. These bunches will be lost. If the excitation parameters are tuned precisely, it is possible to remove a singular bunch without any impact on neighboring bunches. This procedure is referred to as *bunch cleaning*. Figure 6.1 shows an example filling pattern created using bunch cleaning. This allows for the creation of an arbitrary distribution of filled and empty

buckets for applications or studies that are dependent on the filling pattern structure. One such study is shown in Fig. 6.2, where the effect of the periodicity of filled and empty bunches on the CSR was investigated [41].

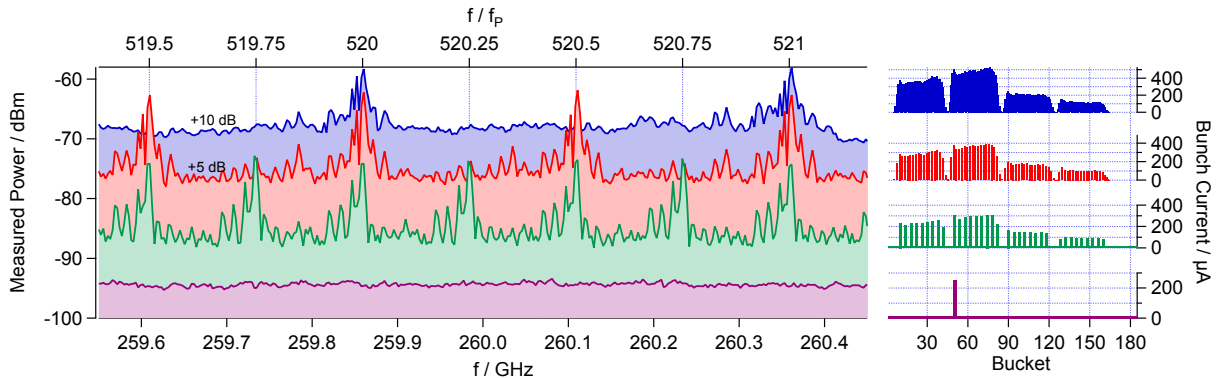


Figure 6.2: Applied studies using different periodic filling patterns created using bunch cleaning. The right part shows different filling patterns, starting with the top in blue with four bunch trains. The red data set has every second bunch removed and for the green data only every fourth bunch is kept. Finally the purple pattern shows only a single bunch remaining. On the left side the measured THz power spectrum at discrete multiples of the revolution frequency is shown with different characteristics depending on the filling pattern periodicity [41]. ©2016 American Physical Society

### 6.1.2 Single Bunch Injection

The overall beam current for multi-bunch beam operation at KARA can reach around 210 mA at 2.5 GeV distributed over four bunch trains. The average bunch current of such a multi-bunch beam is around 1.5 mA but with typical beam and bunch currents at a lower level. While it would be possible to remove all other bunches and therefore effectively create a single-bunch filling pattern, the bunch current would be limited due to multi-bunch effects. A more effective approach for obtaining a single bunch with a high bunch current is to inject only a single-bunch train and use the cleaning method to accumulate only current in one bunch. This allows for the circumvention of multi-bunch limitations and allows for the injection of single-bunch currents of more than 4 mA, as shown in Fig. 6.3. While creating a single-bunch filling pattern would also be possible with the short pulse operation mode of the e-gun, a pure single-bunch injection has its own challenges [4]. A pure single-bunch injection requires adjustments to the injection due to various differences if only a single bunch is accelerated and transferred between the pre-acceleration steps (discussed Chapter 3). It is often favorable to use the default multi-bunch injection scheme, since it allows to seamlessly transition between multi- and single-bunch operation. Typically in this scenario the injection starts with the whole bunch train for a while and once it has been established that all systems are operational and in nominal parameter range – which is easier with more bunches and higher overall beam current – all unwanted bunches are removed. Additionally, this approach also allows for the injection of more than one single bunch into the same train simultaneously. Figure 6.4

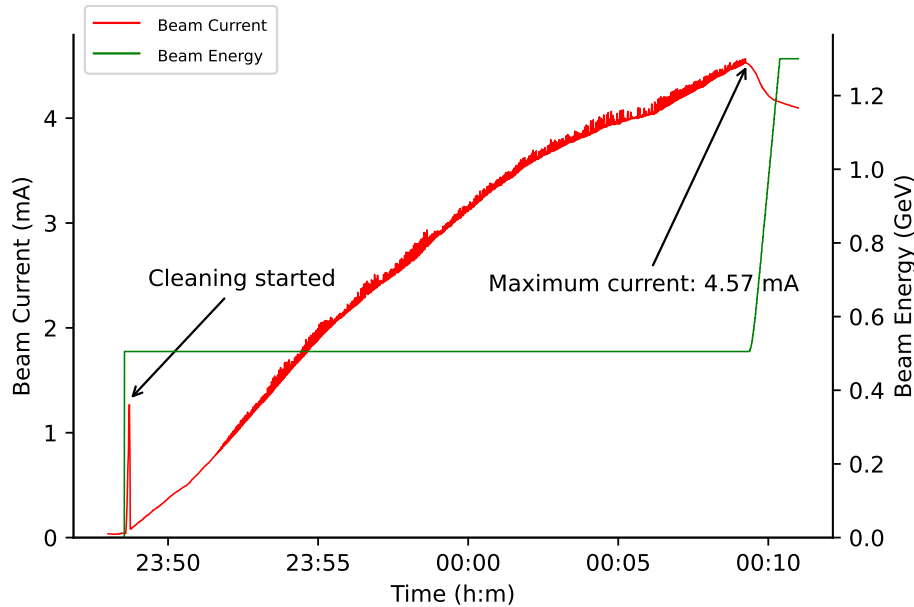


Figure 6.3: High single-bunch injection using active cleaning. This shows the beam current during the injection energy in preparation for short bunch studies at 1.3 GeV. The first peak in beam current is due to the injection into the whole bunch train, after which the cleaning process is switched on removing all but one bunch. During the increase of bunch current, the fluctuations of the beam current is characteristic for this approach, since the additional injected current is removed quickly but not immediately and the averaged beam current measurement picks up these current fluctuations. Once the injection is stopped the fluctuations also disappear. This single-bunch injection is one of the highest single bunch currents recorded at KARA in the recent history, still being above 4 mA even after the usual losses during the energy ramp, as seen on the right hand side.

shows a filling pattern consisting of three bunches which were injected using multi-bunch scheme with one bunch train and active cleaning but leaving three bunches untouched. For such a scenario with multiple bunches of one bunch train the multi-bunch injection scheme is much more efficient, especially since high bunch currents typically have low lifetime and injecting into each bunch individually would lead to overall lower bunch currents. Creating a filling pattern with more than one – but separated – bunches becomes especially useful for measurement setups which are limited due to heat- or beam-loading effects or where the data acquisition rate can be higher than the revolution frequency of 2.7 MHz, but still significantly below the full bunch-by-bunch frequency of 500 MHz, such as the Karlsruhe Linear array detector for MHz rePetition rate Spectroscopy (KALYPSO) detector, which is under active development at KIT [42].

### 6.1.3 Custom Filling Pattern

If the excitation amplitude during bunch cleaning is tuned very carefully it becomes possible to reduce the bunch current without fully removing the excited bunch. Therefore, the bunch current can be manually adjusted to any level (as long as the desired bunch level

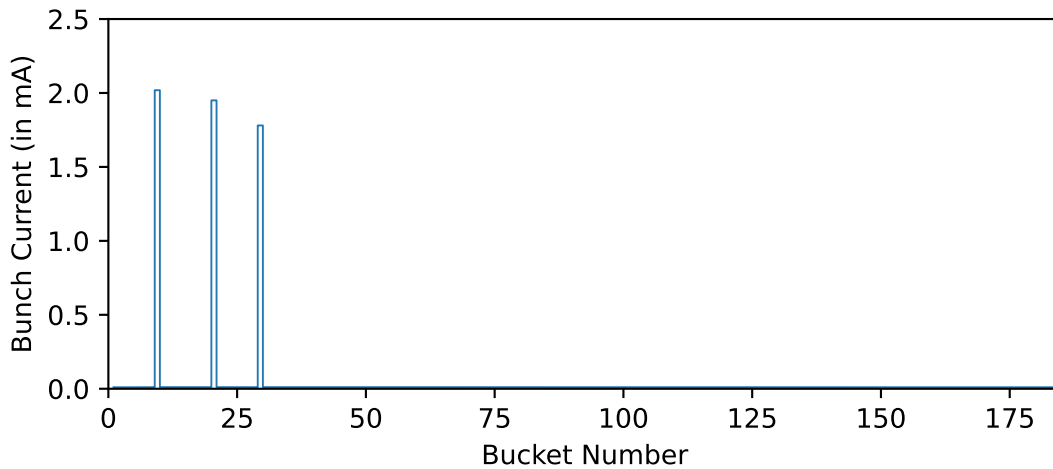


Figure 6.4: Measured filling pattern with three bunches. This is the result of a injection into one bunch train and simultaneous cleaning of all bunches except three. As long as the bunches which should be kept are part of one bunch train the effort in time and tuning is exactly the same independent of the number of bunches, which is especially useful, since higher single-bunch currents have low lifetimes.

is lower than the current bunch level). The approach is to create a custom filling pattern not only with buckets filled or empty but also with a well defined current distribution across the individual bunches of the filling pattern. Manually adjusting the bunch current of many bunches, which can take a substantial amount of time, is limited by the reaction speed of a human operator and because the overall natural loss rate of electrons is high – or in other words the lifetime is low – the process to create such a custom filling pattern has to be automated. Additionally, the specific current distribution required might change depending on the particular focus of the beam study. Therefore, an algorithm was implemented to automate the cleaning process and a user interface logic was designed to allow any operator to define such a custom filling pattern. This interface allows the creation of a linear slope in bunch currents. This slope can either be positive or negative. Also the range or the first and last bunch of such a slope can be defined. One special feature is to keep a linear bunch distribution, but randomize the order. Three sections can be defined which typically are oriented around three possible bunch trains, but one section is not necessarily fixed to a bunch train. Figure 6.5 shows the user interface. The user interface allows to calculate a *desired filling pattern* taking the actual filling pattern into account and previews the actual outcome directly to the operator. Once the operator is satisfied with the projected outcome, the algorithm can be started. The algorithm uses the BRAM acquisition engine, since it has the fastest acquisition cycle of 5 Hz. Next to the time domain signals and calculated FFT spectra – which were discussed in more detail in Chapter 5 – the acquisition engine also provides a mean signal level for every bunch which is directly correlated to the bunch current. Since the operator defined a target level for each bunch and the BRAM engine provides a current equivalent measured with 5 Hz, the algorithm can use bunch cleaning on every bunch individually. It will switch automatically and at the right time to the next bunch once the desired bunch level for the current bunch is reached. This allows for the creation of a multi-bunch filling pattern,



Figure 6.5: GUI to configure custom filling pattern. In the top section of the pattern shape planer three sections of the filling pattern can be selected by defining the first and last bunch of each section. Next, the minimum and maximum counts are defined which are directly correlated to the bunch currents. Finally the slope can be defined: Positive, negative or random. The result can be seen in the lower part, where the current filling pattern in blue, the purely calculated pattern based on the parameters above in green, and the expected outcome is shown in orange. Once the cleaning algorithm is started a red marker will show the progress.

where the individual bunches can cover a range of different bunch currents at the same time. This is of particular interest for studies of bunch current dependent effects such as CSR, where additionally certain bunch current thresholds exist [44]. Instead of having to measure a full natural beam current decay over many hours the bunch current can be reduced to the relevant threshold levels using the BBB feedback system. If the measurement setup is capable of measuring the detector response of the synchrotron radiation for every bunch individually this approach can be taken one step further. The Karlsruhe Pulse Taking and Ultrafast Readout Electronics (KAPTURE) acquisition system is capable of capturing a detector response for every bunch and every revolution – as long as the detector response is also below the bunch spacing at 500 MHz [45]. Acquiring data for only one second will still cover the relevant range of bunch currents without the need to slowly measure over extended periods of time – often multiple hours – until the bunch currents naturally drops below the interested bunch current range. This not only speeds up the required measurement time, but also allows the operator to systematically study the effect of certain beam parameters such as the cavity voltage or the beam optics configuration within the same beam operation session in so-called *snapshot measurements*. Since usually the number of bunches in one bunch train is enough to cover the relevant bunch current range, additional bunch trains can be formed with the same distribution but with different order of the bunches currents so as to investigate possible multi-bunch effects.

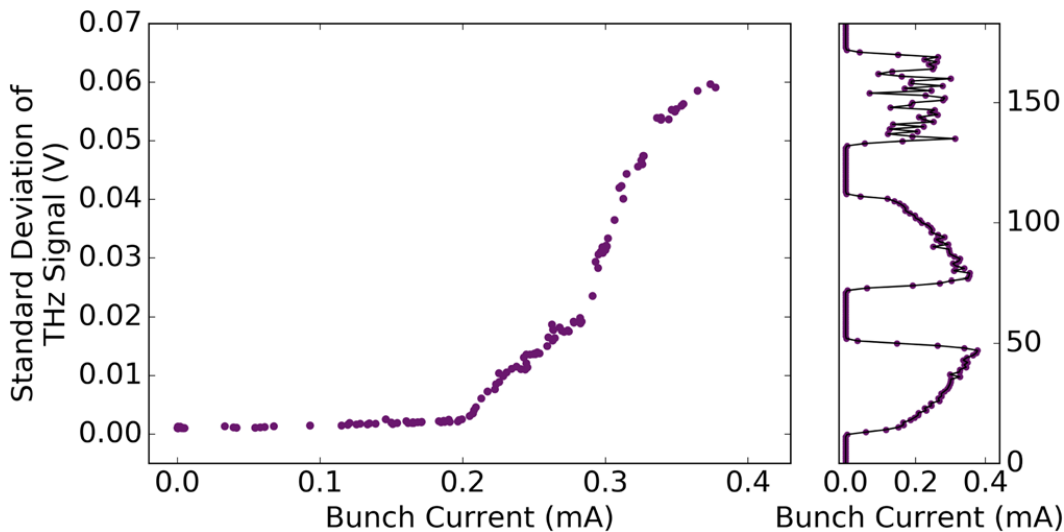


Figure 6.6: Example of applied study using a tailored custom filling pattern. The right hand side shows the filling pattern with three bunch trains. The bottom two trains show a sloped bunch current distribution along each bunch train whereas the top bunch train has a similar bunch current distribution but the bunch current order is randomized. On the left the standard deviation of the THz signal is shown.. Each data point corresponds to one of the bunches from the filling pattern covering a bunch current range from nearly 0 to 0.4 mA with some noticeable current thresholds around 0.2 and 0.3 mA. Courtesy of Miriam Brosi and previously published in [43].

Figure 6.6 shows one such study making use of both aspects [43]. Further improvements to the cleaning algorithm are planned especially for such a use case with multiple, but similar desired bunch train patterns, where the cleaning would happen simultaneously on multiple bunches instead of a sequential approach.

## 6.2 Transverse Beam Damping

The transverse beam dynamics are mostly defined by the optics and therefore the magnetic fields of the quadrupole magnets. The natural damping behaviour in the absence of instabilities is dominated by synchrotron radiation damping as discussed in Sec. 2.3.6, while other factors such as the chromaticity [46] also influence the damping times. The BBB feedback system can be very effective in damping transverse motion, as will be shown in this section, including direct effects on beam stability and reliability.

### 6.2.1 Single-Kick Excitation

To investigate transverse beam damping and the effect of active feedback *single-kick* measurements have been done. A single-kick excitation describes a strong and immediate excitation to the beam which only lasts a short amount of time – for nine revolutions in this particular case. This is possible using strong pulsed magnets usually referred to as *kicker magnets*. The transfer of beam during the injection process described in Sec. 3.3.1 requires multiple such kicker magnets in the booster synchrotron and the storage ring.

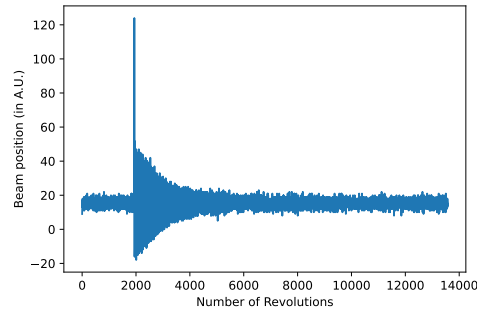


Figure 6.7: Single-Kick measurement in time domain for one bunch. Shown is the measurement of an individual bunch acquired with the BBB feedback system, which can record up to 65,000 revolutions for each bunch. The data shows the stable position of the beam centroid before the single-kick excitation and its subsequent damping.

Usually they are well aligned to generate the multiple kicks necessary to combine the already stored beam with the additional incoming beam. But to investigate beam damping behaviour they can also be used individually. Fig. 6.7 shows such a horizontal kick and damping behaviour using the acquisition engines of the BBB feedback system which allow to readout data for all bunches individually. For this measurement a filling pattern shown in Fig. 6.8 has been chosen with nearly every possible bunch filled with some bunch current. The individual bunch currents vary along the filling pattern and drops especially low for the bunches between the bunch trains. Fig. 6.9 shows a direct comparison of a bunch with lower and higher bunch currents, which does effect the original amplitude and the damping times. A possible explanation for this is that even the strong single-kick still has a rise time in which different sections of the beam will see slightly different strengths of the initial kick.

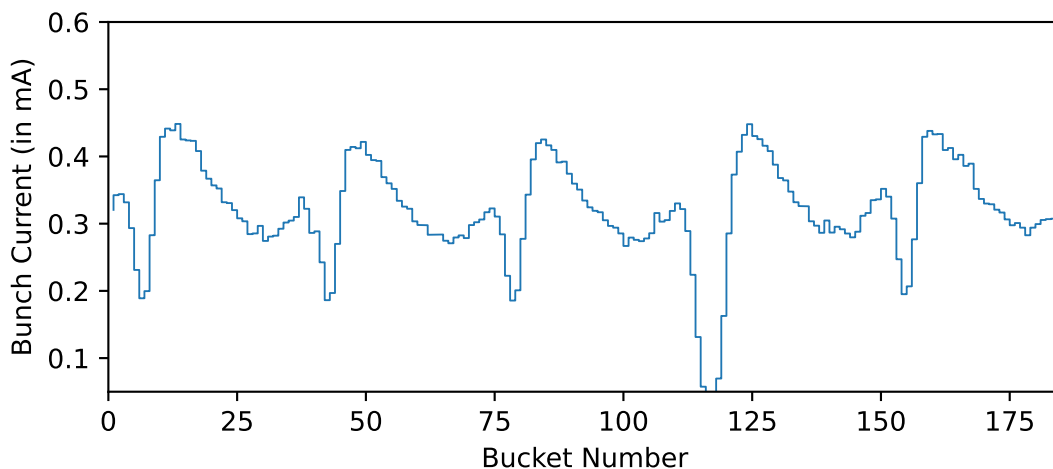


Figure 6.8: Filling pattern used for single-kick studies based on five bunch trains. Nearly all bunches are filled except a small gap around bunch number 120. This particular region of very low or no current is ignored throughout this section. The bunch current varies along each bunch train. Additionally, the very last and very first bunches of each bunch train have significantly less bunch current.

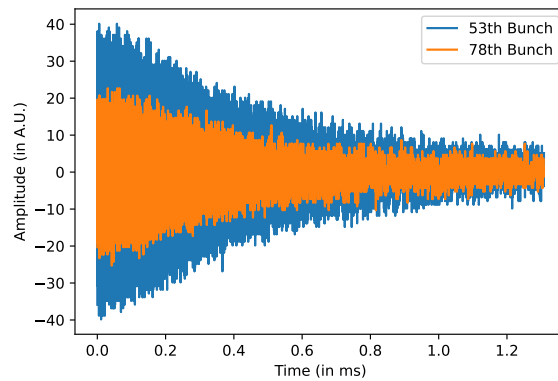


Figure 6.9: Natural damping behaviour of a single-kick measurement for different bunch currents. The beam centroid position is subtracted and the data starts at the revolution after the kick. The x-axis now shows the time in ms. Bunch 78 (orange) is one of the bunches with relatively low bunch current compared to bunch 53 (blue). The original excitation and damping behaviour is noticeably different. A possible explanation for this is that even the strong single-kick still has a rise time in which different sections of the beam will see slightly different strengths of the initial kick.

### 6.2.2 Effect of BBB Feedback

In a situation without beam instabilities the damping time is defined by the natural damping of the beam emittance as discussed in Sec. 2.3.3 and follows an exponential decay of the form:

$$y = e^{-\frac{1}{\tau}k}. \quad (6.1)$$

Applying this approach to the measured data can be used to estimate the damping times. To be able to fit the exponential decay the envelope of the beam oscillation has to be found. This is possible by applying a *Hilbert transformation* to the data [48]. Fig. 6.10 shows the envelope and the fitted exponential decay in two scenarios: faster and slower damping times. For slower damping times one single exponential decay does not describe the data very well. In this case only a later part of the whole damping is fitted, which results in larger estimated damping times. The slower damping will ultimately define the overall damping time. The BBB feedback system in active feedback configuration can damp oscillations and effectively prevent CBI from growing (as discussed in Sec. 4.2.2). But depending on the overall strength of the feedback setting, the BBB system will also have a significant effect on the overall damping behaviour. The strength of the feedback can be expressed as the *gain* (also discussed in Sec. 5.1), which is a integer number between 0 and 7. Important to note is, that even with 0 gain the feedback is still actively damping, and incrementing the gain by 1 roughly doubles the strength of the applied feedback. The envelopes of the damping behaviour with varying gain are shown in Fig. 6.11 with gain up to 5, which will dramatically reduce the damping times. At the same time, too much gain will also overdamp the oscillation and might introduce an additional oscillation as shown in Fig. 6.12. Therefore a typical gain value at KARA is around two to three. Using the BBB data, a damping time can be estimated for each bunch individually. Fig. 6.13 shows the damping times along bunches and for varying gains. Quite clearly visible is some dependency also on

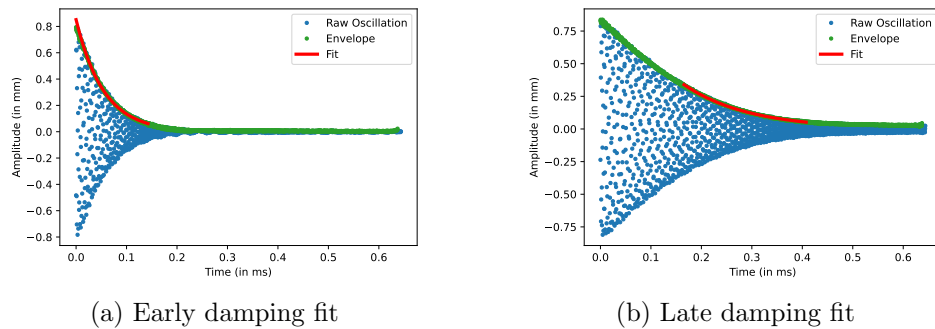


Figure 6.10: Envelope and fitted exponential decay to single-kick excitation for different damping times. The envelope (green) is obtained by a *Hilbert transformation* [48]. Based on the fitted exponential decay (red) to the envelope the damping time can be estimated. The left side shows strong damping and an exponential fit which describes the damping very well. For longer damping times one exponential fit cannot describe the full damping behaviour. Therefore the fit is moved to a later section of the damping, since the longer damping time is in the end the relevant damping time for the overall beam damping.

the bunch current, since the bunch current distribution is not constant. At the same time, the average across all bunches agrees very well with the averaged turn-by-turn data for each gain value. The results are listed in Table 6.1. Interestingly, even the natural damping times of around 0.5 ms are significantly below the theoretical transverse damping times of around 3 ms [49]. This was also already observed in previous measurements without the additional bunch-by-bunch resolution [46]. The natural damping times are even lower, but at the same time also the chromaticity has changed to lower values as discussed in Sec. 5.3. While a bunch current dependency on the damping times is visible, it does not explain the large difference to the theoretical damping times. One possible explanation could be that the proper damping times cannot be resolved by only measuring the coherent movement of the beam centroid as it is done for both the turn-by-turn and the bunch-by-bunch data. Measuring also the horizontal beam size would also be sensitive to the incoherent motion. Further studies with different amount of filled bunches and also measuring the horizontal beam size are planned to further investigate this. Also additional contributions based on the beam coupling between the horizontal and vertical plane or the temperatures of the RF cavities need to be considered.

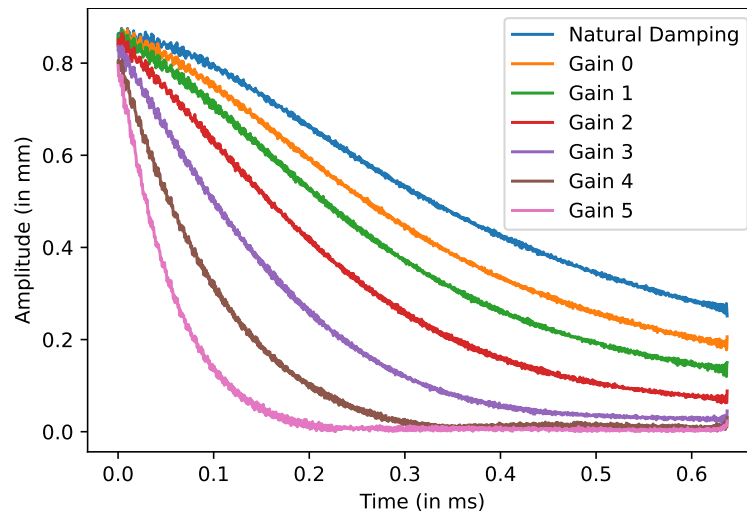


Figure 6.11: Damping envelopes of single-kick measurements for varying feedback gains. Each curve represents a different gain value or in case of the blue curve without any feedback. While the initial amplitude is independent of the feedback strength, a reduction of up to 90% damping times for high gains can be observed. Table 6.1 lists the estimated damping times based on the exponential fits.

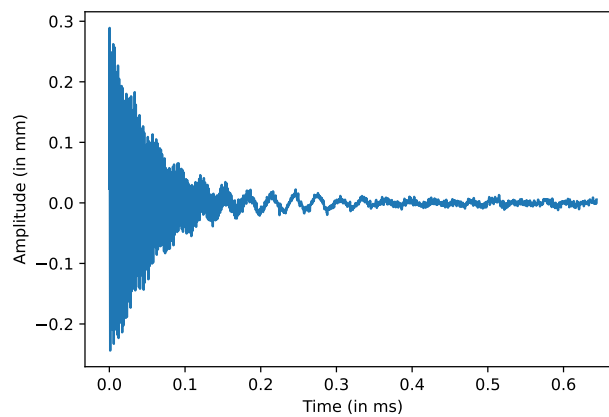


Figure 6.12: Beam ringing for very high feedback strengths. Shown is the ringing for one BPM with a gain setting of 5. The strong ringing during and after damping indicates too much damping and induced oscillation by the feedback system itself. During normal operation conditions usually lower gain values are used to avoid this kind of over-response.

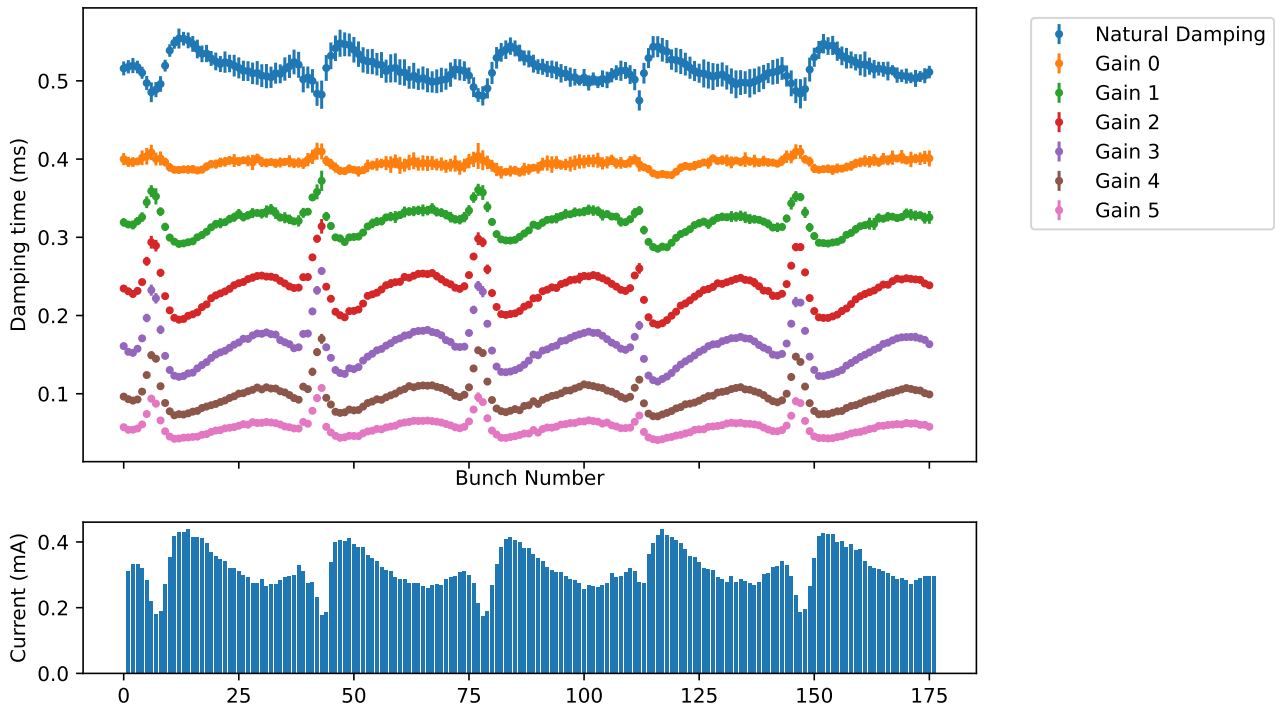


Figure 6.13: Damping times for all bunches. The lower part shows the filling pattern with some variation in bunch currents. The x-axis is the bunch number of the bunch in the filling pattern and is shared with the plot above, which shows the damping time for each bunch with different colors representing different feedback strengths. Each color represents different feedback strength. The damping times show a bunch current dependent effect: For natural damping the damping times decrease with bunch current, whereas with active feedback the opposite happens. With high gains the overall damping times are still lower for all bunches. Also the averaged damping times across all bunches agree very well with the turn-by-turn data as listed in Table 6.1.

Table 6.1: Damping times for varying feedback strengths for turn-by-turn and averaged bunch-by-bunch data.

Feedback Strength	Damping Time (in ms)	
	Turn-by-Turn	Bunch-By-Bunch
Natural Damping	$0.49 \pm 0.01$	$0.52 \pm 0.02$
Gain 0	$0.39 \pm 0.01$	$0.39 \pm 0.01$
Gain 1	$0.32 \pm 0.01$	$0.32 \pm 0.02$
Gain 2	$0.23 \pm 0.01$	$0.23 \pm 0.03$
Gain 3	$0.15 \pm 0.01$	$0.16 \pm 0.03$
Gain 4	$0.10 \pm 0.01$	$0.10 \pm 0.02$
Gain 5	$0.06 \pm 0.01$	$0.06 \pm 0.02$

### 6.2.3 Improved Beam Stability

Due to the reduced damping times provided by the BBB feedback system throughout the whole operation range from injection at 0.5 GeV to beam operation at 2.5 GeV, the general beam stability was improved substantially. The main contributions were less losses due to beam instabilities during injection and the energy ramp and therefore a more consistent and reliable injection environment. Once the beam has settled at 2.5 GeV beam instabilities are not a major concern anymore and the focus shifts to improving the beam lifetime. Outside of beam current drops due to instabilities, the feedback system is not capable of directly improving the lifetime of the beam, since the main contributions for the loss of particles are Touschek scattering – which is an intra-bunch effect – and residual gas scattering as discussed in Sec. 2.4.1. Fig.6.14 still shows an increase of lifetime once the feedback system was in operation of around 25%. The main difference here was that the feedback system allowed the injection of an additional bunch train into the filling pattern. Before active feedback during injection was possible, operation was limited to a three bunch train configuration with large gaps between the trains. With the improvements of damping time and suppressed CBI this configuration could be changed to a four bunch train configuration without gap between the trains. Figure 6.15 compares both configurations. The gain in beam lifetime then comes from improving the Touschek lifetime, which is dependent on the individual bunch currents, as shown in Sec. 2.4.1. The typical 2.5 GeV synchrotron

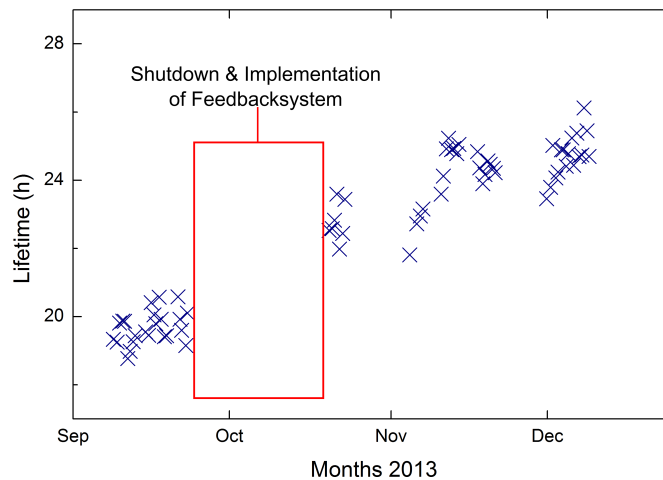


Figure 6.14: Increased lifetime due to active transverse feedback. Shown is the lifetime per operation cycle at the same total beam current. The BBB made it possible to inject more bunches into KARA which decreased the average bunch current while keeping the same total beam current. Since lifetime is largely effected by Touschek scattering, this improved the overall beam lifetime.

radiation applications at KARA are not sensitive to the individual bunch structure and are only interested in a high average beam flux. Another improvement was the increase in average beam current. The total beam current is not only limited by the achievable bunch currents, but also by the total beam current, due to beam loading, heating effects and impedance contributions (discussed in Sec. 2.4.3). Therefore changing to a four bunch train configuration does not necessarily also increase the overall beam current by 25%.

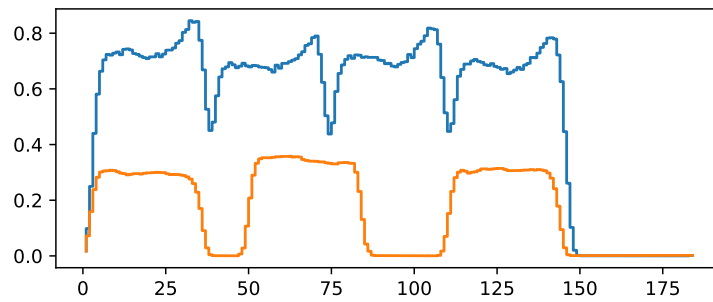


Figure 6.15: Comparison of typical filling pattern configuration for 2.5 GeV operation. Shown is the typical four bunch filling pattern (blue) and overlapped the typical three bunch train configuration (orange), where as the bunch current regime was chosen to visualize the difference in bunch position. The overall gap after the last bunch train is unchanged. The four bunch train filling pattern is only feasible with active transverse feedback.

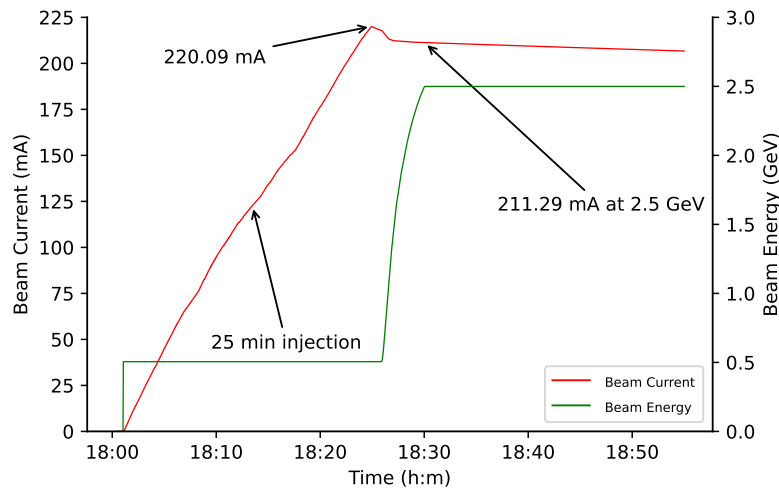


Figure 6.16: High current injection. Efficient injection to currents above 220 mA were possible due to active transverse feedback which was one of the reasons for a change in daily operation cycle of KARA to one injection per day.

Still, the average injected beam current could be improved and Fig. 6.16 shows an injection with one of the highest achieved total beam currents injected as well as one of the highest beam currents at 2.5 GeV, while injection lasted less than half an hour. The improvements to beam lifetime and average injected current was also one of the reasons the daily operation cycle of KARA was changed from originally performing two injections per 24 hour cycle to only one injection.

### 6.3 Bunch Lengthening

In Sec. 6.1 the BBB feedback system was used to excite individual bunches to effectively create a tailored filling pattern. But it can also be used on all bunches at the same time and therefore excite the whole beam. At KARA the injection process during which the beam current is accumulated, at a lower energy of 0.5 GeV, ideally takes half an hour to

an hour, depending on the beam current and filling pattern goal. The injection process was detailed in Section 3.3.1 and very efficient injection rates were shown in Fig. 6.16. But several factors can also create an intrinsically non-ideal environment for stable beam operation. For one, the accumulation process requires the merging of the new and existing beams using multiple strong pulsed magnets on both beams. Furthermore the beam optics and the beam orbit are designed to optimize the accumulation process, not the long-term stability. And due to the lower energy, the injection takes place at a reduced beam rigidity (see Eq. 2.84). The low lifetime of the stored beam has to be compensated for by the injection rate, otherwise the overall beam current cannot be increased. This is emphasized even more for higher beam currents, where also the beam loss rates increase with additional detrimental contributions due to multi-bunch and beam loading effects. This creates challenges in the day-to-day operation so as to consistently and reproducibly inject to high beam currents. The BBB feedback system can successfully mitigate beam losses due to coupled-bunch instabilities (CBI) by reducing the oscillation amplitudes of the electron bunches as seen in Section 6.2. At the same time this reduces the acceptance which can in turn reduce the injection rate. For higher currents this can lead to a saturation of the injection rate. But at the same time increasing the acceptance by switching off the active feedback might lead to a CBI-triggered beam losses. In this scenario, the BBB feedback system can provide a solution to these issues. While the beam is controlled by active feedback, the drive engine can create an additional – controlled – longitudinal beam excitation. This leads to a bunch lengthening and effective increase of longitudinal acceptance [50] as well as preventing possible beam losses due to CBI. The excitation is defined specifically at twice the resonance (synchrotron) frequency  $f_s$ . Figure 6.17 visualizes the longitudinal beam motion by using a streak camera [51] and showcases the three scenarios: beam current losses due to instabilities without active feedback, injection saturation but no beam losses due to strong active feedback, and an unaffected injection rate with active feedback and additional longitudinal bunch excitation. The controlled excitation can be switched on or off at any given moment as needed. For lower, more stable beam current regions the excitation is not needed and is also ideally switched off before the energy ramping process at high beam currents. It can also be set up in a way where it is switched on automatically during the injection at a given current threshold and switched off as soon as the injection is finished.

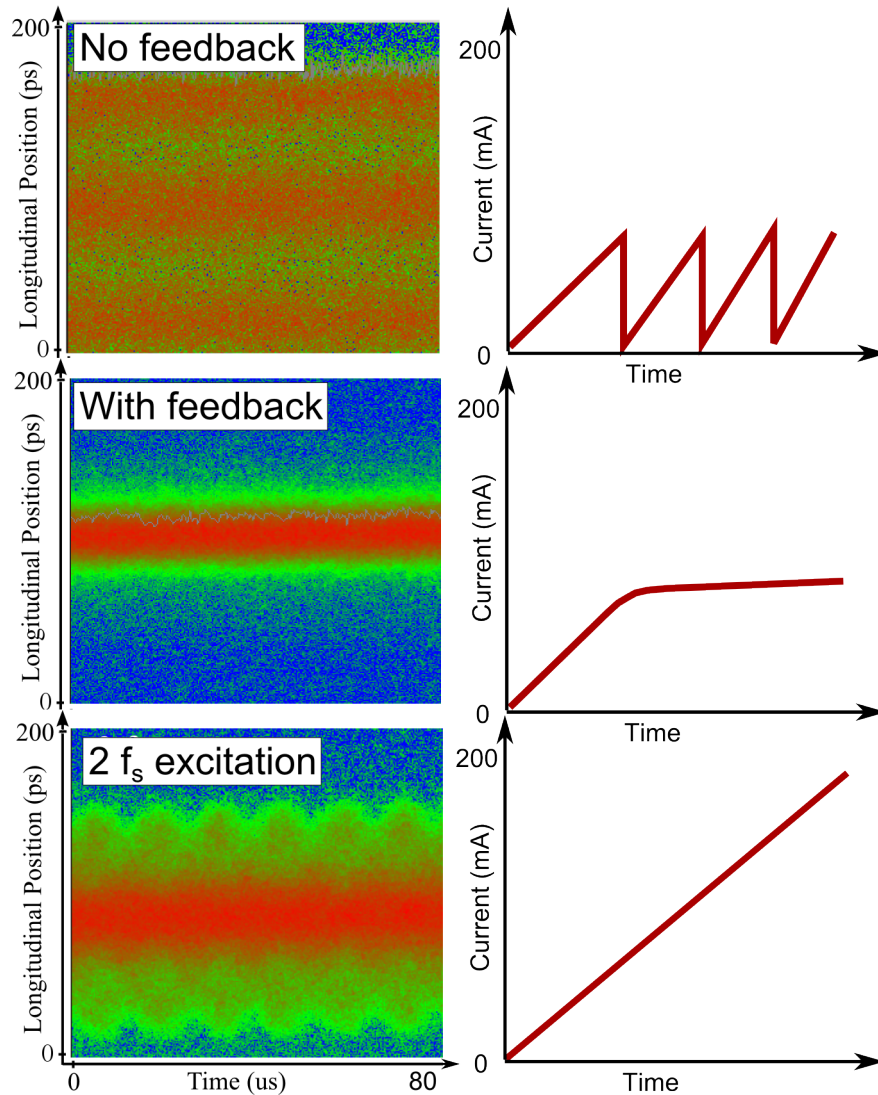


Figure 6.17: Controlled beam excitation during injection. Each row shows one of three scenarios. On the left side a measurement of the streak camera is shown, which shows the longitudinal center of charge position of the beam over time and therefore the longitudinal oscillation. On the right hand side the beam current during injection is shown. The scenario of the first row is without active longitudinal feedback showing large oscillations and beam losses during the injection. A certain beam current threshold could not be surpassed due to longitudinal instabilities. The second row shows the situation with active longitudinal feedback with a stable longitudinal motion. But the ability to inject into the existing beam is diminished, leading to a beam current saturation which creates a soft limit on the beam current. The last row shows the scenario with active longitudinal feedback and additional controlled beam excitation at twice the synchrotron frequency  $f_s$ . The streak camera measurement shows the controlled additional oscillation leading to an effective bunch lengthening. This keeps the injection rate stable allowing the beam current to surpass both the instability and diminished injection rate thresholds. The controlled beam excitation can be switched on and off at any given time as needed [50].

## 6.4 Longitudinal Beam Dynamics

Longitudinal beam dynamics is mostly driven by the RF fields inside the RF cavities and the emittance of synchrotron radiation as discussed in Sec. 2.3.3. In a multi-bunch environment possible instabilities are defined by existing higher order modes in the cavities and wakefields (discussed in Sec. 2.1.2 and Sec. 2.4.3). To investigate possible instabilities it is often useful to analyze the Eigenmodes of the longitudinal beam motion as discussed in Sec. 2.4.4. The acquisition engine of the BBB feedback system can record the individual bunch motion of every bunch, which can also be used to analyze the prevalence of certain modes.

### 6.4.1 Eigenmodes during Injection and Energy Ramp

One approach to investigating the modal spectrum is to record full data sets during certain phases of beam operation without active feedback. For this, every couple of seconds a full BBB data set is acquired which records the full length of data of 25.2ms or 68384 revolutions per bunch. The modes can be identified in the FFT of the bunch motions. Based on this, the mode spectrum is calculated and displayed as a function of time. In case of the injection process the beam current changes over time, while for the energy ramp the energy is changing over time. Fig. 6.18 shows such an analysis. While there are clearly dominant modes visible in this particular measurement between 40 mA and 60 mA the dominant mode switched from mode 45 to mode 40 for higher beam currents with the upper sideband mode  $184 - 40 = 144$  showing similar behaviour. During the energy ramp the energy range below 1 GeV is the most critical area, which usually also corresponds to larger beam current losses during the energy ramp compared to other energy regions. Above 1.1 GeV the longitudinal Eigenmodes mostly disappear and only the fundamental mode 1 remains, which is defined by the main synchrotron motion of all bunches. Using active longitudinal feedback will in general be able to damp down all Eigenmodes considerably, as seen in Fig. 6.19, which demonstrates the Eigenmode spectrum with and without active longitudinal feedback. At the same time, the BBB feedback system also allows for the systematic study of each mode as discussed in the following section.

### 6.4.2 Grow-Damp Measurements

While being able to measure and identify dominant Eigenmodes is already useful, it requires the mode to be naturally present during the measurement. Additionally, smaller but still relevant modes might not be visible. Next to the ability to excite certain frequencies and bunches, the BBB feedback system also provides a mechanism in which the feedback configuration is changed for a certain period of time. The timescale on which this is possible is in the range of the acquisition window of the of the SRAM or BRAM engine. The possibility to change the effective feedback is referred to as *grow-damp measurements*, since there is typically a period where the beam is not under active damping feedback – the growth period – which is immediately followed by the damping period. Technically the feedback system swaps the feedback filter during the growth period to a different predefined set, which is one of the reasons multiple feedback filter settings can be stored in

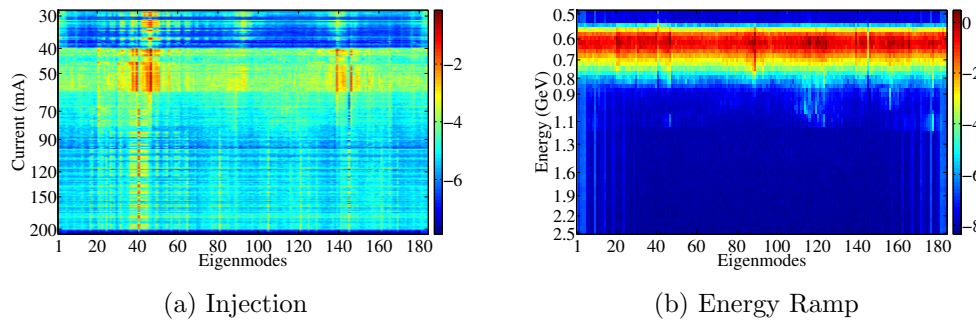


Figure 6.18: Longitudinal Eigenmodes during injection and energy ramp. Every line represents a fully analysed data set in regards to the strength of each particular mode, which is color coded, with red being stronger and blue weaker modes. The injection on the left is against beam current and the energy ramp on the right against energy. During injection, modes 40 and 45 are the most dominant modes. During the first 500 MeV of the energy ramp the beam is exposed to multiple effects leading to a less stable environment.

parallel (as described in Sec. 4.2.2). A basic approach is to store two filter sets: The first defines the normal damping behaviour, while the second filter is shifted by  $180^\circ$  in phase, resulting in explicitly driving the resonance term. This driving filter has the potential to quickly excite the beam in a way which will most likely result in total beam loss if applied for too long. Therefore the growth section can typically be limited to the ms regime, which is in the range of typical damping times (see also Sec. 6.2).

Another useful approach is to have one filter basically empty. Depending on if this is the main or the alternate filter, this allows one to investigate either natural oscillation growth or damping. Since running active damping feedback typically also masks the presence of uncommon instabilities – which might be worth investigating – this provides a safe option for exploring these. Due to the various settings for the acquisition shown in Fig. 4.12 and discussed in Sec. 4.3.2, the grow-damp mechanism is very flexible. Also since filters can be set up to only effect specific regions, this allows for the bunch-to-bunch effects to be more more closely investigated. Figure 6.20 shows a basic example of a driven grow-damp. The important benefit of grow-damp measurements is that it allows for the systematic investigation of the various factors contributing to beam instabilities, such as different beam currents, bunch currents, and filling pattern configurations, or different beam parameters such as the optics, the RF frequency, or the beam energy.

### 6.4.3 Temperature Dependency of Eigenmodes

Using grow-damp measurements gives an additional level of flexibility. The internal drive engine (Sec. 4.3.1), which was already used to modify the filling pattern (Sec. 6.1) and to lengthen the bunches during injection (Sec. 6.3), can also be applied during grow-damp measurements replacing or supplementing the growth period. These are often then referred to as *drive-damp measurements*. This also adds the full flexibility of the drive engines to grow-damp measurements. Since the drive engine can excite any frequency up to half of

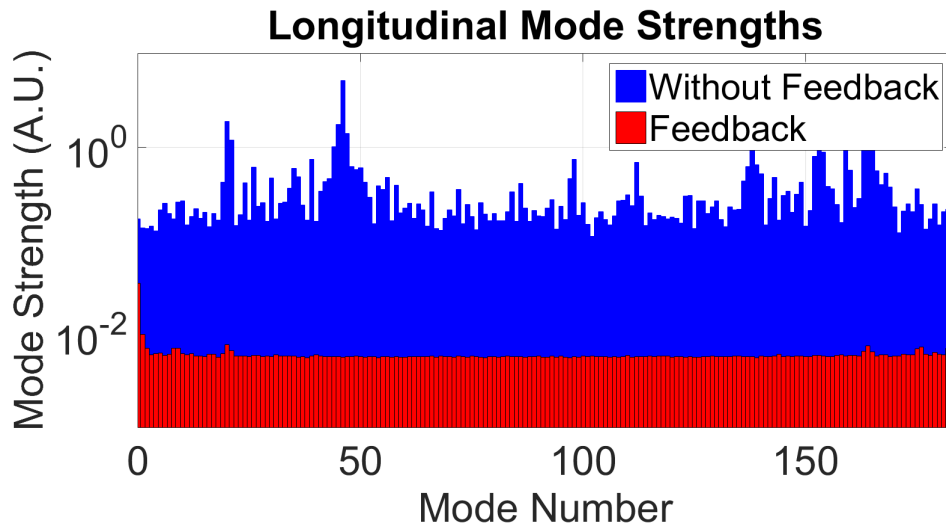


Figure 6.19: Presence of longitudinal Eigenmodes. Shown is the strength of each mode without (blue) and with (red) active longitudinal feedback. The BBB feedback system enables all modes to be significantly suppressed.

$f_{\text{RF}}$ , it can explicitly excite any Eigenmode. The frequency  $f_m$  to excite the mode  $m$  is given by:

$$f_m = \frac{(\nu + m)}{h} \cdot f_{\text{RF}} \quad \text{for } m < \frac{h}{2} \quad (6.2)$$

and

$$f_m = \left(1 - \frac{(\nu + m)}{h}\right) \cdot f_{\text{RF}} \quad \text{for } m \geq \frac{h}{2} \quad (6.3)$$

with the fractional tune  $\nu$ , the harmonic number  $h$  and the RF frequency  $f_{\text{RF}}$ . This also makes clear the difference between the modes below or above  $\frac{h}{2}$ , which are fundamentally the same mode, but excite the lower or upper sideband around the synchrotron frequency harmonic. It is therefore:

$$f_m(n) - f_m(h - n) = 2f_s \quad \text{for } n < \frac{h}{2} \quad (6.4)$$

with the synchrotron frequency  $f_s$ . The drive-damp measurement can now be setup in a way where during the drive section one particular mode is excited and during the damp section no active feedback is applied. With this approach the natural damping behaviour of each mode can be measured. Since no active feedback is applied, the beam has to generally be in a stable condition, for example below possible current dependent instability thresholds. Otherwise some excited modes might not damp naturally during the damp period. Fig. 6.22 shows an example of the damping of one specific mode. While this seems to be very similar to the analysis in Sec. 6.2, it is important to notice that here the damping time is based on the damping of a particular frequency and not overall beam oscillation, which is defined by the oscillation of all modes combined. Any one particular damping measurement is mostly limited by the amount of time it takes to read out the data, which usually takes longer than recording the data. For a systematic study of mode damping it is therefore useful to optimize the data readout. For this, the feedback system can be set up to stream out the raw data directly, which is usually switched off to avoid

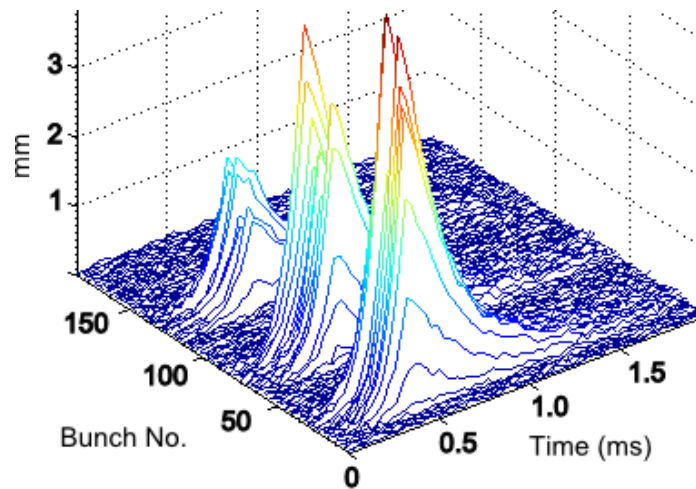


Figure 6.20: Example grow-damp measurement. Shown is the evolution of the bunch motion in the time-domain in one axis and the bunch number on the second axis while the height represents the oscillation amplitude. This is an example of a filter-reversal based grow-damp measurement, where the damping feedback filter is inverted for about 0.5 ms and with a three train filling pattern and the bunches respond individually to the slow excitation over many revolutions.

overloading the network. This limits the measurement now mostly to how fast the mode frequency can be set and how many data sets per mode frequency should be recorded. Five drive-damp measurements for each of the 184 possible modes then results in around 23 GB of raw data. Fig. 6.21 presents such a full mode scan with the damping times of the lower and upper sideband of each mode is shown against the mode number. Averaging the damping times over all modes results in the overall longitudinal damping time:

$$\tau_L = 0.93 \pm 0.08ms. \quad (6.5)$$

Compared to the transverse damping times in Sec. 6.2, the longitudinal damping times are more in line with the theoretical damping times of 1.5 ms, which is half of the transverse damping times as discussed in Sec. 2.3.6 [49]. The mode with the longest damping time will end up defining the overall damping time, which is mode 28 in this case, being slightly closer to the 1.5 ms:

$$\tau_{L, \text{Mode}=28} = 1.16 \pm 0.08ms. \quad (6.6)$$

The longitudinal Eigenmodes are characterized dominantly by the RF cavities and by their higher order mode (HOM). One way to change the behaviour of HOM is to change the operating temperature of a cavity [52]. Then a full mode scan can be repeated for different cavity temperatures and the change in damping times for each mode can be investigated. As discussed in Chapter 3 KARA has four main RF cavities of the same type. Due to the high sensitivity of the cavities to all of its design parameters, each cavity might have a different spectrum of characteristic HOM, which also manifests in the fact that each cavity is typically operated at a different selected temperature and the temperature of each cavity can also be adjusted individually. This allows for the investigation of the change in modal

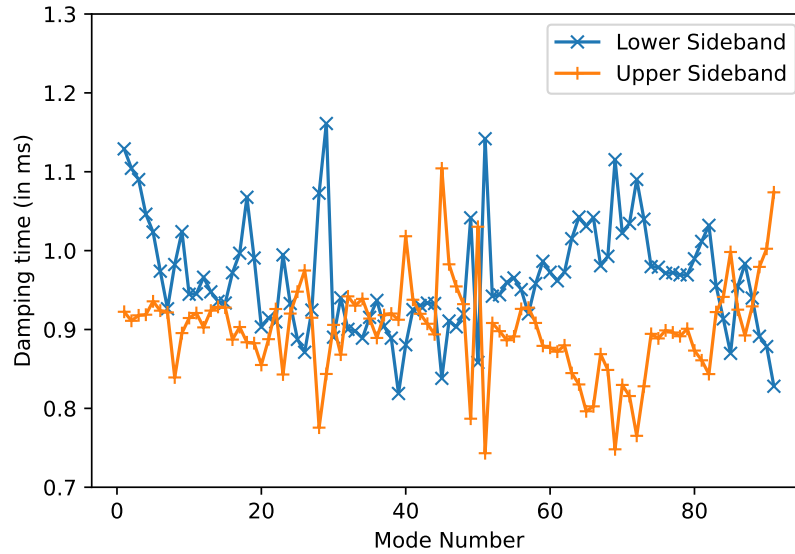


Figure 6.21: Damping times of all longitudinal Eigenmodes. Shown is the upper and lower sideband of each mode. The upper sideband of the lower sideband mode  $m = 5$  can also be identified as  $n = 184 - m$ . In this particular environment no single mode is particularly dominant, but areas around mode 25, 45 and 75 might be noteworthy. By averaging the damping times across all modes the longitudinal damping time can be estimated.

damping behaviour cavity by cavity by keeping the temperatures of the other cavities at a constant reference level.

Such a systematic cavity temperature scan has been done for nine different cavity temperatures in a range of  $\pm 2$  K relative to each cavity reference temperature with a step size of 0.5 K. Instead of showing both the upper and lower sideband of each mode, the difference between the upper and lower sideband can be a useful metric [52]. Figure 6.23 presents the combined results of the nine full mode scans per cavity across three of the four RF cavities. While for most modes and cavity temperatures the relative difference in damping times for the upper and lower sideband is very similar, the influence of the first cavity is significant for two different modes and different directions in temperature change. Figure 6.24 shows the changes in damping behaviour for these two modes along the temperature difference. Since any temperature change will effect some modes substantially, the HOM of this particular cavity seem to be dominating compared to the other cavities. Being aware of the temperature dependent mode characteristics of each cavity allows to choose the individual temperature for each cavity to accommodate the preferred behaviour for the current operation regime. Due to the complex measurement technique and analysis of large amount of data, the whole process from preparation of the accelerator and the BBB feedback system, the measurement process (which includes not only the repetition of the mode scans itself but also the change of cavity temperature and a long enough grace period until the cavity temperature settles to the new setting) up until the full analysis, including the temperature and cavity separation and plotting, has been fully automated. Considering that the raw measurement time and the analysis of all scans can take several

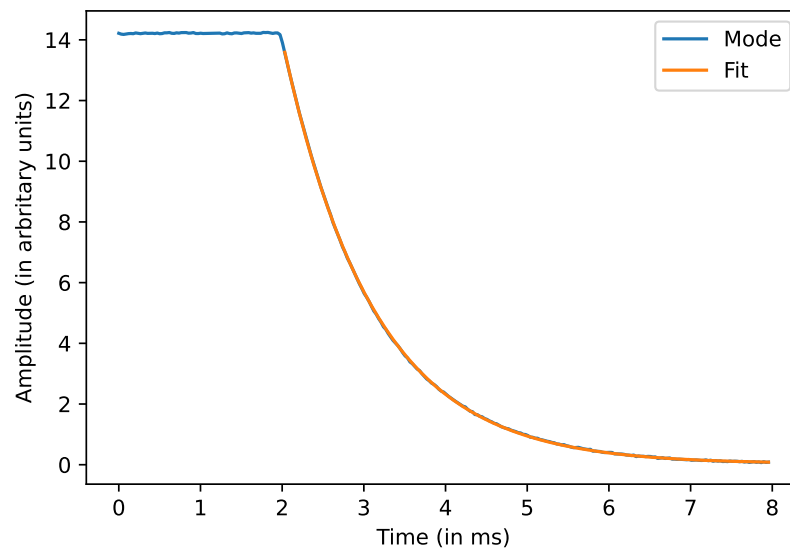


Figure 6.22: Example of drive-damp of one specific mode. Visible is the behaviour of one particular mode and the drive-damp approach, where the mode is driven for the first 2 ms and after that break point the drive is switched off and the mode damps naturally without active feedback. The acquisition period ends before the next drive period starts. While similar to Fig.6.10 the important difference is that this only shows the damping of one specific frequency component compared to the time domain signal which is the combination of all frequencies.

hours, automation is necessary to investigate larger temperature regions, as well as different beam conditions. The only limitation becomes at amount of available beam time.

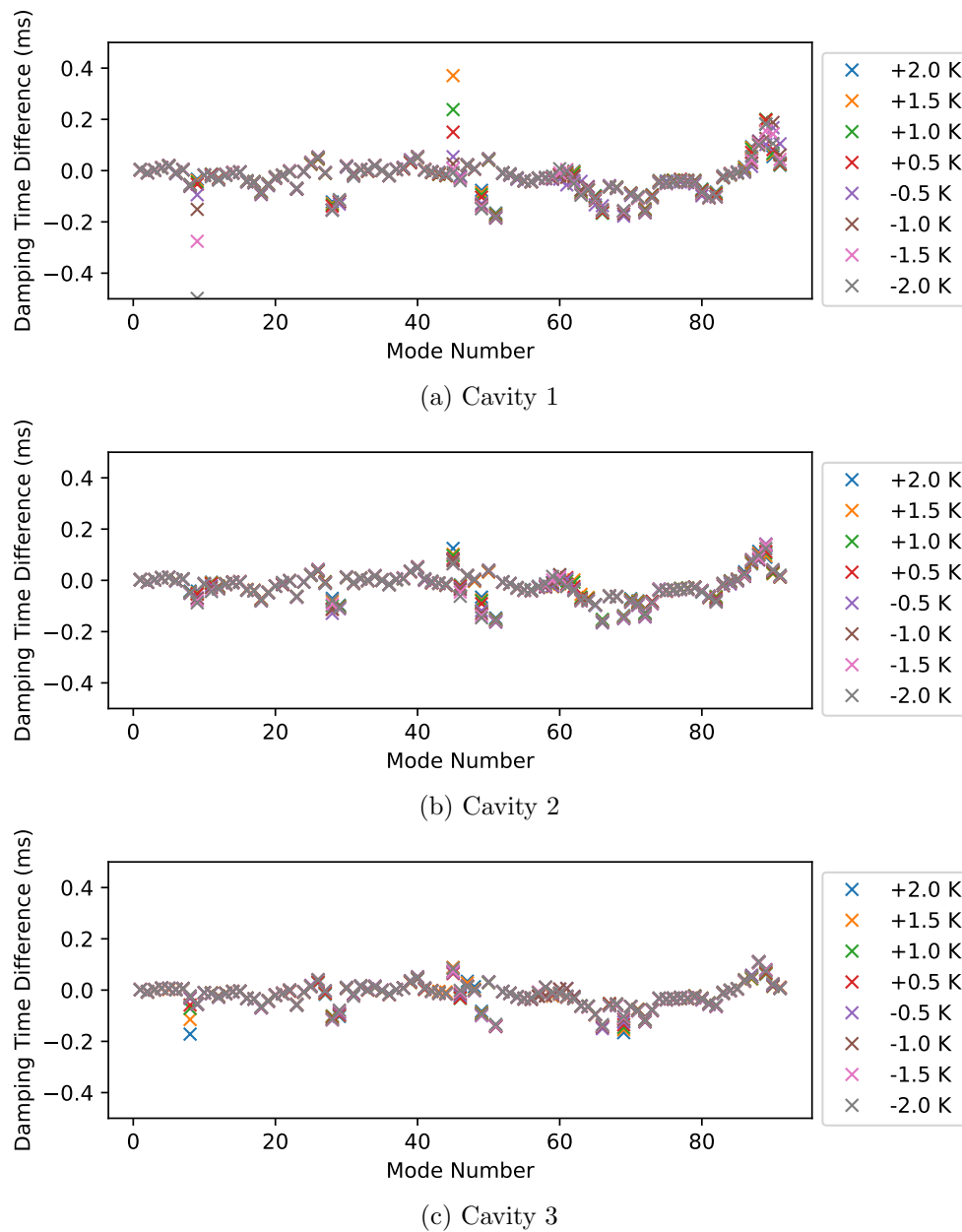


Figure 6.23: Systematic mode analysis over cavity temperature. In each figure one color shows the modes for a different temperature of the captioned cavity only. The modes are displayed as the difference between the lower and upper sideband. The mode changes of mode 9 and 45 during the temperature scan of cavity 1 indicate that the HOM of this particular cavity are dominant.

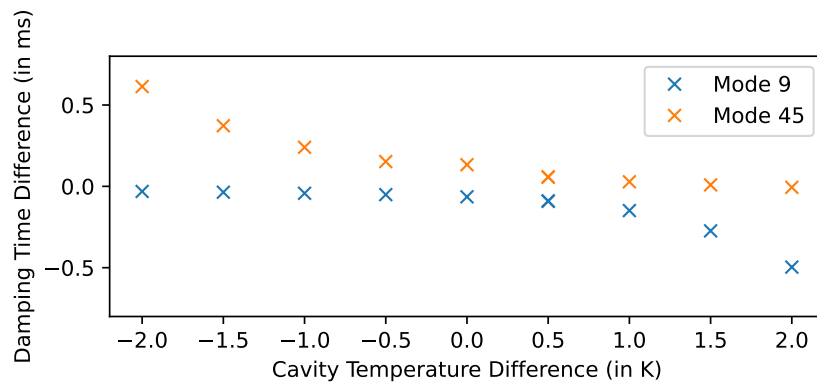


Figure 6.24: Influence of cavity 1 temperature on most significant modes. Mode 9 and 45 show the largest temperature dependency, while the relative change in upper and lower sideband difference is in the opposite direction.

## 7. Summary

As discussed at the beginning of this thesis being able to operate a particle accelerator with electrons moving close to the speed of light is a complex task. To provide the well-defined parameters required for the range of possible applications a sophisticated set of tools is required to monitor, influence and even control the beam motion. The BBB feedback system provides such a system focusing on the rapid oscillations and interactions of individual electron bunches.

As an outcome of this thesis, substantial improvements were made to KARA and the surrounding infrastructure by leveraging the capabilities of the BBB feedback system. The general approach taken here was to automate measurements, analysis, and specific beam manipulation patterns in such a way that they can be used as needed without requiring the full knowledge of how the BBB feedback system works and interacts with the accelerator. On the one hand this allows the feedback system to work transparently during regular beam operation without making the task of operating the accelerator more complex, while still providing all the crucial benefits for the varying operation conditions of KARA. On the other hand, automated active measurements and the ability to manipulate beam motion and beam structure as needed also allows the operator to take advantage of the feedback system for cutting edge research topics. To analyze the long-term data measured by the BBB feedback system, a framework was developed and each operation cycle of the accelerator was indexed. This will benefit many future studies and investigations, independent of the feedback system, and has the potential of becoming the default framework at the Institute for Beam Physics and Technology (IBPT) for all interaction with accelerator related data even beyond applications at KARA.

The studies presented in this thesis focuses on two areas. Firstly, the BBB feedback system provides additional information in the form of measurements which were previously unavailable – at least not in the same form. The main beam parameter that the feedback system provides in this context is the tunes. Since the tunes serve as a characteristic beam parameter for the state of the accelerator with regard to the beam optics, being able to

---

analyze the tunes during operation, but also for past operation cycles, becomes very valuable. First, it is important to be aware of how the tune measurement works and which possible technical factors might contribute to the reliability and precision of the tune read-out. Secondly, it is also important to know which changes that occur whilst operating the accelerator might intentionally or unintentionally affect the tune measurement. Once this is understood, the evolution of tunes can be studied and insights can be gained about the state of the accelerator on short timescales, such as during an energy ramp, but also over long periods of time, such as the beam operation over multiple months, as shown in the first half of Chapter 5. Deeper into the studying the tunes, there are also measurements derived by the changing tune. Such measurements also benefit greatly from an improved tune measurement. It was possible to now fully automate chromaticity measurements, leading to more than 1000 such measurements over time, making it a routinely used and reliable measurement. Using the active damping of the feedback and the active measurement of the chromaticity also allowed for the operation of KARA at natural chromaticity, something basic accelerator physics textbooks often summarize as not possible. In the last part of the tune chapter, the potential to investigate the geometrical impedance was shown, which can also be derived by observing changes in tunes. Due to the established more precise tune measurement using phase tracking on a single bunch, even small effects caused by multiple in-vacuum movable structures could be observed. This again was put into context by also looking at differences over the last several years, where multiple structural changes to the vacuum chamber of KARA occurred, mostly while installing new insertion devices.

Secondly, since the BBB feedback system needs to be able to interact with any bunch and at any frequency so as to damp coupled bunch motion, it opens up a large range of active beam manipulations. Furthermore, it also allows for the close monitoring and for measuring the results of such manipulations. Changing the structure of the filled bunches and research applications based on these techniques were discussed in the beginning of Chapter 6. With the focus of research at KARA on the structure of short electron bunches and new fast diagnostics, the ability to manipulate the filling structure by either fully removing or even precisely reducing individual bunch currents proved very valuable. In the extreme case this also allowed for the injection of only individual bunches instead of full bunch trains, thus making it possible to provide single-bunch currents, which is not possible in a multi-bunch environment. Another interesting use case was the bunch lengthening by exciting the beam motion longitudinally to allow for a more efficient injection. Both the active damping and active excitation can be relevant in such scenarios. And finally, one of the most crucial features provided by the diagnostic abilities of the BBB feedback system: Measurements of the individual bunch motion during a well-defined excitation. For the transverse case, this was used to study the damping effects of the feedback system. An interesting bunch current dependency was measured, as well as some additional insight being gained into the situation of the seemingly too short transverse damping times. In the longitudinal plane the presence and change in the strength of the Eigenmodes was investigated, while changing the driving factor of these modes, the higher order mode, inside

the RF cavities. It was shown that each cavity does have its own characteristic influence and at the same time the exact mode numbers, which are excited, could be identified.

This brings me to the final conclusion. By the versatility of the feedback system many improvements were achieved at KARA, starting from increased beam stability and ending with deep insights into the details about the intricate motion of a multi-bunch particle beam. Many of the results presented here will lead to further investigations and to a better understanding of the accelerator and the underlying physics involved, an understanding that was enabled by the here developed methods.

---



## 8. Appendix

### A Data Archiving at KARA

In a modern accelerator most devices typically communicate over the general network and provide continuous data towards the accelerator control system. This includes technical parameters of the hardware, as well as data of diagnostic equipment, providing many interesting beam parameters and measurements. These can easily exceed thousands of individual data points. Depending on the source of information, each individual data point might also be updated on an individual level in a range of up to 10 Hz or only, due to manual changes, once per day or even less. Typically there is a large interest in storing as much of this data as possible. Traditional concepts of storing data in *relational* databases are not well equipped for this task, since they are optimised for relational data which also might need to be changed at a later point of time.

#### A.1 Database Concept

An alternative approach is the use a database which is focused on storing key-value pairs in independent columns. The key is always the time stamp and the value is the process variable (PV) which should be stored. There is no need to ever go back and update an existing value and therefore the database can be optimised to write the data samples efficiently on a column by column basis. In an accelerator control system certain types of *meta-data* should be stored as well such as the alarm state of the data, possible measurement units, or precision information, among others. Since over time the demand to store more and more data always grows, the scalability is also important: The database should work in a cluster of database nodes, where additional nodes can be added as needed. To meet all of this criteria the *Cassandra PV Archiver* was developed for use at KARA, which uses the *Cassandra* database [53, 54]. Important to know is that in the stored time series the entries are not stored equidistant or in context with any other PV, but just by itself as often as it changes. The archive rate is also by no means fixed for one data column: For example, if the energy changes often during the four minute energy ramp of KARA, but not during the many hours of stable operation, the database only writes samples during

---

the energy ramp window. It is therefore also very simple to add additional data points to the archive, since basically only the unique identifier – the process variable (PV) – has to be added to the configuration of stored columns.

Right now at KARA more than 30 000 data points are being archived continuously, with additional PV being added month by month. To give one example relevant to this thesis: The horizontal tune data point is updated with a maximum rate of 2 Hz, which therefore creates up to 172 800 data points per day. Over the course of the existence of the data since the commissioning of the feedback system towards the end of 2013, around 7 years of data has been accumulated. Extrapolated based on the maximum daily rate, the amount of stored data could be more than 400 million data points (441 504 000 to be exact). The actual number is somewhat lower due to certain periods during shutdown periods where either the feedback system or the archive system might have been offline. Also to consider is that this is only for the horizontal tune. Overall one BBB unit for each plane of motion – horizontal, vertical and longitudinal – provides around 200 different data points. Of course not all of them are changed at a 2 Hz rate, but it is a significant number of read-back parameters for each unit.

Table 8.1 shows an example: Listed are the amount of data points stored in the archive for two different moments in time, but for the same length of five minutes or 300 seconds. Shown is the data for the measured beam current, the beam energy – which is technically not a measured but rather a set point value based on the current supplied to the dipole magnets –, the horizontal and vertical tunes, and the read back value of the current applied to one quadrupole magnet family. As seen, the data length might vary in every aspect, even for similar values such as the tunes or for the same value at a different point in time, but for the same time interval.

Table 8.1: Example for varying data length for different data points and moments in time.

Parameter	300 s Range 1	300 s Range 2
Beam Current	302	301
Beam Energy	1	2
Horizontal Tune	290	511
Vertical Tune	313	497
Quadrupole 1	131	163

## A.2 Compression Intervals

The database in use at KARA is optimised for very high throughput performance for writing samples to the archive, which enables storing of all available data continuously. The challenge in working with archived data now lies in how to efficiently retrieve and handle archived samples. For example, there is no situation where it could be even technically possible to retrieve and work with all stored data for the horizontal tunes in the range of multiple years. To help with this, the database internally handles data by additionally creating various compression intervals. This compression depends on the individual type

of data: A set point data such as the current supplied to a power supply cannot be compressed without losing relevant information. At the same time, there is usually no need to compress set point data, since the sample rate stored in the archive is very low. But for example the actual measured value of the current changes constantly, at least due to noise. Since this is typically a floating point number, a compression usually can be made by averaging this value, which does reduce the amount of data without necessarily losing too much information. The database automatically creates various different compression intervals for all of its stored data, if applicable to the type of data. Important to note is: At some point, historic raw data might be dropped from the archive in favor of only keeping the compressed values. So far this has not happened at KARA and would also only affect the oldest data.

To request data at least three parameters have to be provided. First: the PV. Secondly, the timestamp for the beginning, and thirdly, the timestamp for the end of the relevant time range. This will always try to request the raw data and might fail just due to amount of involved data. At which time range this will become an issue for raw data depends very much not only on the time range, but also on the data density of the requested PV.

Optionally, a fourth parameter can be used: the *count* parameter. With this parameter one can specify how many data points should be returned. This parameter does not enforce a fixed data density by decimating or averaging the data dynamically. Instead, by specifying the count parameter, the database will try to return data from one of its stored compression levels which best matches the count parameter. Table 8.2 shows the therefore not necessarily intuitive behaviour of the count parameter. Listed is the data length returned for the request of beam current for different time lengths with a fixed count parameter of 1000. The beam current is roughly stored at a 1Hz interval: For

Table 8.2: Example for varying data length based on the count parameter of 1000 for the beam current.

Requested time range (in s)	Returned data length
10	12
100	102
1000	1001
10 000	9989
100 000	1666

the first two intervals less raw data exists than the count parameter, therefore all data is returned. Requesting data for 1000seconds also returns the raw data plus one. But the last two values are interesting: Requesting data for 10 000seconds also returns roughly 10 000 values, despite the count parameter of 1000. This is because no better compression interval exists for this time range: Therefore the raw data is returned. For 100 000seconds on the other hand, a compression level does exist. Although it does not match exactly the count parameter (which it basically never does), it returns interestingly less data than the request for 10 000s. While this behaviour is not necessarily very intuitive, it serves an important application: Typically one wants to process and work with the data requested.

By using a fixed count parameter, the time range one requests data for is not as critical: It can be minutes, hours, months or even years and – mostly – one can expect that the request will work and the amount of data returned is manageable.

### A.3 Data Resampling

Getting the data one is interested from the archive nearly always results in the request of multiple different PV. Broadly speaking there are two types of data requests: The first type is when one wants to look at different PV in the same period of time. For example: To look at the current dependency of the tunes, one wants to request the beam current and both transverse tune values. So one will need to query the database three times with the same time range, but different PV. The issue now is that, due to the nature of how the data is stored, it is not trivial to directly compare the values. Each request will most likely return with a different amount of data. Also important to remember is that the data is not equidistant. To handle this issue it is important to remember that a data request will not only return the data points, but every data point also has a timestamp attached. One needs to treat each requested data always as a key-value pair with its own individual timestamp. But for many practical applications, it is often useful work with the data using one single index for all data. This can be done after the data is retrieved from the archive and is achieved by creating a table based on all available timestamps across all data and filling up the gaps in the rows with the information available. In addition to that, often a fixed time interval is preferred – for example an interval of 1 s. This *resampling* can be solved by an algorithm.

### A.4 Data Filtering

If one already knows the exact time range of where to find the data the problem regarding accessing the data from the archive is already solved. One can just request the data. If however, one naively wants to request data based on other related data – for example the tunes during a certain range of beam currents – there is an issue: Since data is stored without any relational structure, there is no way to directly request correlated data from the archive. The only approach available is starting to filter the data manually. For the example given – retrieving the tunes for a certain current range – it is assumed that of interest is the last injection cycle. Also it is already known when the injection started and when it finished. Therefore the task is fairly straightforward: One first requests the current for the whole injection. Then, one searches in this data for the current range of interest. Since every current data point also has a timestamp attached, two new timestamps can be defined which reflect the time range where the current has the desired values. With this newly obtained timestamps one can finally request the tune data.

Different to *resampling*, filtering the data cannot be automated or solved by existing algorithms. If a certain PV is generally useful filtering the data, it can be described as a *strong filter*. How strong a filter is depends in first order on how useful looking at this particular data is by itself. For example, the beam current is a fairly strong filter: A beam current larger as 0 indicates that the accelerator is in operation. If the current is increasing, one can definitely state that at that moment of time an injection is ongoing.

---

After this point the current becomes a weaker filter: If the current decreases it can be either because of the energy ramp, because of the accelerator is in stable operation, or it can actually still be during injection and the losses are due to technical issues or beam instabilities. As an opposite example, a tune value by itself is a very weak filter. Just the value of the tune without further knowledge provides nearly no information which can be used as a filter. Only with enough knowledge and experience can one start guessing certain beam conditions based on the tune values. But as seen in Sec. 5.2, sometimes a lot of context is needed.

Being able to filter the database requests efficiently requires not only experience, but also knowledge down to the technical level of the accelerator control system, to be aware of PVs which can be applied as strong filters to the problem at hand. Also combining different weak filters can create stronger filters while some of the strongest filter can become worthless in certain scenarios. As a general rule of thumb, one should always start with the strongest filter available for a given problem and narrow down the data filter by filter. There is only one filter which is always very strong: The timestamp. The more a-priori knowledge one has about the relevant time frames, the easier it gets to access the data. To stay with the given example: We assumed to already know when exactly the injection started. If this information is not available, the given task becomes more complex. Depending on the problem at hand, it might therefore be worth the effort to create and store an index of timestamps correlated with additional information. If one wants to study many injections, it will help tremendously to first create an index with the start and end of every injection cycle instead of always applying filters to the data. Once this index is created it now becomes very simple to, for example, study different correlations during each injection.

## A.5 Conclusion

Storing all available data points that KARA generates has tremendous advantages, since it also stores many beam parameters. Complex correlations can be done years back into the history of KARA. But the challenge lies in actually retrieving data in a usable way. Certain tools can be very helpful with the technical tasks of gathering the data. But for deep correlation studies, a fundamental overview is required of which PV exist and how they might be applicable as a useful filter. The effort required can be greatly reduced by creating an external index of timestamps for often requested time frames such as individual fills.

## B Indexing KARA Operation

The database described in Appendix A is active at KARA since 2013. While it did not start with anywhere near the 30 000 PV it is storing today, some of the most important PV were added right in the beginning. Also the BBB system was installed in 2013 and was one of the earliest additions to the archive. In Chapter 5 an in-depth study of the tunes over the full history of the BBB systems use at KARA was done. To be able to do

---

that, the first task was to create an index for every operation cycle. The importance of creating an index was discussed in the previous section.

## B.1 Motivation

During one operation cycle three very different situations occur: The injection process, the energy ramp, and the beam operation. These scenarios are very different in terms of which beam parameters change and which ones are interesting to look at. It is therefore useful to add to the index the time when the injection starts, when the energy ramp starts, and when the beam operation phase starts. These sections are also vastly different in how long they are present: The energy ramp lasts less than 4 minutes, the injection usually takes around 30 to 60 minutes, and the beam operation can last for up to 24 hours. It is therefore crucial to have the exact time down to the second for each of these phases. Since the energy ramp always follows directly after the injection and the beam operation follows the energy ramp, storing four timestamps per operation cycle is enough to describe the three phases: First, the moment the injection starts. Secondly, the moment the energy ramp starts. Thirdly, the moment the energy ramp finishes and lastly, the moment the beam is no longer stored. Figure B.1 shows these four timestamps along the beam energy and beam current of a typical operation cycle.

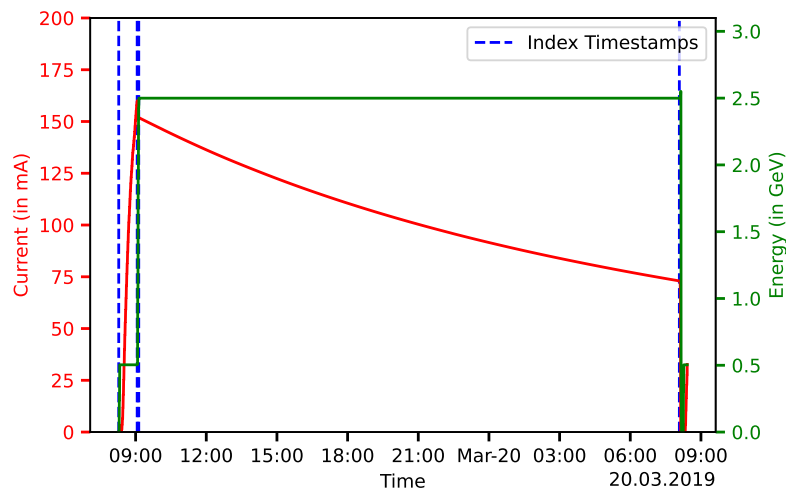


Figure B.1: Index timestamps for an operation cycle of KARA. The four blue lines mark the relevant timestamps which should be available for each operation cycle: Start of injection, start of energy ramp, end of energy ramp and end of beam operation. Start and end of energy ramp are only minutes apart.

## B.2 Filters

The database stores many PV in independent columns. To be able to figure out the desired four indices, a selection of *strong filters* is needed, as discussed in Appendix A. The discussion of filters used will be limited to the three strongest filters available for this task: the fill number, the beam energy, and the beam current.

### B.2.1 Fill Number

The *fill number* is an number, which is – manually – incremented for every operation cycle of KARA. The first stored fill number in the continuous archive is the 4747, while the fill number 7500 was crossed recently. In theory, the fill number should already solve the issue at hand: By looking at the fill number one should know about the start and end of each operation cycle. In practice, it turned out that solely relying on the fill number is not precise enough: First, the actual end of an operation cycle is not directly obvious. Since the fill number is incremented for the next operation cycle only, some scenarios are not easy to identify: On the one hand, accidental beam losses, and on the other hand, all kinds of shut down periods, especially during every weekend. Secondly, it is incremented manually. Therefore, the relative point of time when the fill number changes during an operation cycle is not consistent and may depend on the habits of the operator: Towards the end of an operation cycle while the beam is about to be removed (but still present), during the process of removing the beam, during the preparation phase to set up the next injection, right before the first beam current is being accumulated, or while the injection is already taking place. Still – without any other information – the fill number remains one of the strongest filters available.

### B.2.2 Beam Energy

The beam energy is another strong filter. Important to understand is that the beam energy PV is not a measured value, but just a scaled number representing the beam energy based on the current supplied to the dipole magnets. Therefore the beam energy is constant during most of the operation cycle. Only during the actual energy ramp and after the beam operation is finished is the energy PV changing. During a typical 24 hour operation cycle the energy PV creates new entries in the database only for a couple of minutes. This allows long time ranges from the database to be requested without the risk of resulting in too much data being returned. This is a important property of a strong filter. Additionally, by looking at the energy, the operation state that the accelerator is in can be quickly estimated: Below 0.5 GeV the accelerator is not able to store beam, 0.5 GeV indicates injection process, and any other non-changing value (typically either 2.5 GeV or 1.3 GeV) indicates beam operation. During the preparation process for the next injection, the energy PV will also shortly show values above 2.5 GeV, which can be used to further narrow down the beam operation window. This can also be seen in Fig. B.1 towards the end of the window. But at the same time it is important to note that just because the energy PV shows, for example, 0.5 GeV, it does not necessarily mean that an injection is actually taking place. On the other hand, all shutdown periods can easily be identified: The beam energy is at 0.

### B.2.3 Beam Current

By analyzing the beam current, the beam state can also be estimated very similarly to the beam energy: If the beam current is at 0 no operation is taking place. If the beam current is increasing, the injection is ongoing. If the beam current is steadily decreasing, beam

operation is most likely taking place. Different to the beam energy PV, the beam current is actually a measured value, resulting in entries being added to the archive around every second – independent of the operation state. Requesting large time ranges – which can be done with the beam energy or the fill number – cannot be done with the beam current. It is therefore not as useful as a first filter. But once a window of interest was determined by using the fill number or the beam energy, the beam current becomes very useful for definitely defining the beam state: The moment where the energy is at 0.5 GeV and the current increases above 0 mA is when the injection process starts. If the energy is not at 0.5 GeV – but constant and above 0 – beam operation is taking place. If the energy is changing, while beam current is present, the energy ramp is taking place. Finally, changes to the beam energy without measurable beam current indicate the preparation phase for the next injection.

#### B.2.4 Edge Cases

As long as the beam operation happens as planned, the filters can be used as described to determine the four indicies. It can get more complicated in situations where issues prevent the normal flow of beam operation. For example: The beam current can drop back to 0, although the injection has already started. In this case, the original time stamp of the first time the beam current rose above 0 should still be used as the start of injection time. Also the beam energy PV might change multiple times during one operation cycle while trying to reset the machine and restart the injection, among other cases. By clever combination of all three filters most edge cases can be identified and properly handled, although it can become more complex as discussed here.

### B.3 Index Management

Combining these filters, an operation cycle can now be identified in the database, including the four indices which define the three phases of each operation cycle. But the process to find these indicies is time and resource intensive. Therefore storing these indicies becomes incredibly useful, since it requires only a single extensive crawling of the database. Any subsequent query or study of beam parameters can be separated based on one operation cycle at a time, compared to scanning multiple years of data at once. At KARA an electric logbook [55] is used to document each default beam operation cycle. This allows the operator to note down any irregularities. One logbook entry consists of a list of attributes which have to be filled in – such as the fill number or the maximum injected current for this particular injection. The very first logbook entry is actually from the year 2005 with the fill number 500 and therefore predates the PV database. This electronic logbook also offers direct access via an API, making it possible to semi- or fully automate creation of entries. Therefore the electronic logbook was extended by four attributes representing the four indicies: start of injection, start of energy ramp, end of energy ramp, and end of beam operation. Since the beginning of the PV database in 2013, around 1800 logbook entries exist. An algorithm was developed to go through each logbook entry and determine the full operation cycle, including the four indicies, and these were added to the entry itself. Additionally, with this information, each entry was extended by two plots: One showing

---

the injection and ramping and the other one showing the stable beam operation. This makes scrolling through the individual logbook entries much more effective, since the beam conditions and beam evolution are visible at a glance. Finally, using the available API, the four indices can be retrieved for every operation cycle present in the logbook identified by the fill number.

#### B.4 Current Status

While the extensive crawling of the database to add the indices for all historic logbook entries was necessary once, it is no longer in the current control system environment. Nowadays all data is available as a PV, even if it is not stored in the PV database. For example, a PV exists which indicates if the energy ramp is currently ongoing – without any ambiguity in regard to other situations where the energy PV might change. The moment of time where this PV changes from zero to one is taken as the start of the energy ramp index. Subsequently, the moment of time where it changes back to zero is taken as the index for when the energy ramp is finished. Additionally, a separate logbook was designed in which all entries are created fully automatically every time an unusual beam current drop is detected. This information is stored together with the current fill number. While multiple beam current drops can happen, the very last beam current drop for each fill number will always mark the final beam dump or beam loss, which can be used as the index for the end of the beam operation cycle. And lastly, a PV exists which stores the information about when the first time the beam current is increased above zero per fill number, which marks the beginning of the injection. This information is automatically added to each new logbook entry which is being created. In parallel also the general work flow for the operator who handles the operation cycle was reworked and streamlined. For example, the fill number is now always incremented as the same step in a well-defined work flow. Lastly, also the design of the logbook was adapted to the new situation, where most data can be filled out automatically, letting the operator focus on only noting down potential issues.

#### B.5 Further Plans

In the future, even more processes will be automated leading to a more predictable pattern of how PV changes during an operation cycle. In addition, another redesign of the electronic logbook is planned. This is due to the fact that the current iteration does not fit the needs of the special machine physics shifts as described in Sec. 3.3.4. This also mostly explains the difference between the 1800 logbook entries but around 2700 increments of the fill number. Including these special operation phases to the general indexing is also especially relevant, since the accelerator is constantly being developed and accelerator research is happening in these operation cycles, which might often be of special interest in correlating certain effects possible all to available PV in the database, which is made substantially easier with the available indices for the different section of operations in combination with the timestamps of the actual active measurements.

---

## C Python Framework

Python is a powerful, fast, and easy to learn programming language [56]. It is available on all operation platforms and is free to use for everyone. Python is also very popular among scientists, with many modules specialized in machine learning or scientific data analysis, for example [33].

### C.1 Motivation

At the Institute for Beam Physics and Technology (IBPT), which operates KARA, the usage of Python has increased considerably over the last years. On the one hand, this was driven by young scientists working on their bachelor or master theses, but on the other hand also core services of the accelerator started to make use of Python. For example, to distribute the control system GUI or to configure the list of PV which are being stored by the *PV Archiver*. Individuals often created their own script libraries to access shared resources surrounding the accelerator infrastructure. To focus development and prevent the need to re-implementing the same functionality over and over again, the idea came up to create a Python framework dedicated to accessibility and to working closely with the available resources of IBPT and KARA. Since the framework was also explicitly foreseen to be part of the core control system, certain measures were taken to ensure a reliable and stable code base. The scripts which were already available were organized in a number of separate Python modules, which are available for anyone in the institute to install as easily as any other Python module. To support long-term maintainability, a set of conventions was defined in respect to the coding and documentation style based on often used conventions for other Python projects. In addition, a so-called *continuous integration* tool-chain was set up, which automatically takes care of: ensuring conventions are fulfilled, making sure the module functions as expected by running a set of tests, and distribution of the created Python modules for easy installation. And finally, any code added permanently to the modules should be reviewed by at least one other person. So far, this approach has already proved to be very valuable for the development of the Python framework.

### C.2 Module overview

The IBPT Python framework is organised in several modules to improve maintainability. Some of the modules have strong dependency on other modules of the framework, whereas others can also be used individually.

#### C.2.1 Accelerator Module

IBPT not only operates KARA, but also other accelerators, which are fundamentally different in regards to accelerator physics, hardware setups, and measurement equipment. The *Accelerator* module provides classes and methods specific to each accelerator. In case of KARA, functions exist to allow easy access to common parameters such as the beam energy, fill number, or  $f_{RF}$ . Also an interface to the BBB system was developed to provide access not only to the tunes, but also much supplementary information. For example, the

---

beam spectrum can be looked at and stored, including all configuration settings relevant to tune measurements, as discussed in Chapter 5. The tune diagrams used in Sec. 5.2 with the capabilities to draw tunes over time or over energy is also part of the accelerator module.

### C.2.2 PV Module

The process variable (PV) describes the unique identifier for accessing data of the control system. While the structure of such a PV follows a defined naming convention, it is rather technical and not easily grasp or remembered by non-experts. The PV module therefore provides aliases to commonly used PV. For example, to read the beam current, the alias *beam\_current* can be used instead of the actual PV *A:SR:BeamInfo:01:Current*. Additionally, the module also provides *PV groups* for lists of similar PV. To name two examples: A group to access all five quadrupole families exists, as well as a group to access the status of all insertion devices.

### C.2.3 Control System Module

The control system module provides access to the Experimental Physics and Industrial Control System (EPICS) in use at KARA. It extends the general *pyepics* module [57] by allowing simplified access to PVs using the *PV module* and improves general usability, for example, by providing exceptions for disconnected PVs.

### C.2.4 Database Module

The database module implements the interface to the *Cassandra PV Archiver* discussed in Appendix A. It is therefore one of the most important tools to work with archived data at KARA and was used extensively in this thesis. It also supports using aliases for PVs and PV groups provided by the *PV module*. One of the core features of the database module is the ability of *resampling* lists of PVs as discussed in Appendix A. Additionally, requests to the database can be made asynchronously, which greatly improves the performance while trying to fetch many PVs. It also allows for searching for any PV available in the database. Useful is also its feature to locally cache data requests. This reduces the amount of time the same data has to be transferred from the database, but also serves as a convenient feature to locally store requested data. The database module is developed and maintained by my colleague Julian Gethmann.

### C.2.5 ELog Module

The ELog module provides the interface to the electronic logbook [55] in use at KARA. It is based on the *py\_elog* module [58]. While there are some improvements made for the specific use case at KARA, an important part of the ELog module is the extension which was developed for the indexing of all KARA operation cycles discussed in Appendix B. It is also used for the semi- or fully automated creation of entries during KARA operation: It prepares entries for each injection cycle which are signed off by the operator and automatically it adds entries based on the beam loss detection algorithm.

---

### C.2.6 IO Module

The input-output (IO) module is a rather recent addition. The main purpose is to serve as a collection of tools to improve access to and handling of measurement data. It currently supports automatically downloading and locally storing data for some of the core measurement data created at KARA. It also provides an interface to *MATLAB* © files. A major feature is the explicit handling of chromaticity measurements. The chromaticity support was developed and used in Sec. 5.3 of this thesis. It ensures data integrity of the raw measurement data, provides multiple fitting routines, and a host of options for how to display and export the results. For fitting, the machine learning module *scikit-learn* is used [33].

### C.2.7 Physics Module

The physics module provides constants and functions useful in the context of accelerator physics. There is also a collection of functions calculating the effects of insertion devices and conversion functions between technical units of the control system to units used in accelerator physics.

### C.2.8 Utility Module

The utility module is a collection of often used methods, such as exporting of plots with proper handling of the meta data. It also provides IBPT specific functions relevant for the different networks in use, which allows other modules to properly react depending on whether the module is used inside the enclosed accelerator network or at home.

## C.3 Status and Further Plans

This Python framework is already now incredibly useful in accessing and using the resources available at IBPT and KARA. It is also already in use in the core control system of KARA. For nearly every module, ideas, plans, and wishes exist to add more features and further improve access to more resources. There are also ideas to create additional modules, for example, to also directly implement measurement routines. To invite more collaboration and contributions IBPT internal presentations are planned to make everyone aware of its existence.

---

# Acronyms

**ADC** analog-to-digital converter

**BBB** Bunch-by-Bunch

**BPM** beam position monitor

**BTF** beam transfer function

**BRAM** block random-access memory

**CBI** coupled-bunch instabilities

**CSR** coherent synchrotron radiation

**DAC** digital-to-analog converter

**DBA** double bend achromat

**EPICS** Experimental Physics and Industrial Control System

**FFT** Fast Fourier Transformation

**FIR** Finite Impulse Response

**GUI** graphical user interface

**HOM** higher order mode

**IBPT** Institute for Beam Physics and Technology

**KALYPSO** Karlsruhe Linear arraY detector for MHz rePetition rate SpectrOscopy

**KAPTURE** Karlsruhe Pulse Taking and Ultrafast Readout Electronics

**KARA** Karlsruhe Research Accelerator

**KIT** Karlsruhe Institute of Technology

**LLRF** low-level RF

**PLL** phase-locked loop

**PV** process variable

**RF** radio frequency

---

**SB** single bunch

**SP** signal processor

**SRAM** static random-access memory

**SLS** Swiss Light Source

**FBE** front-end/back-end

---

# Bibliography

- [1] Andrzej Wolski. *Beam Dynamics in High Energy Particle Accelerators*. Imperial Collage Press, 2014.
  - [2] Klaus Wille. *Physik der Teilchenbeschleuniger und Synchrotronstrahlungsquellen*. B. G. Teubner Stuttgart, 1996.
  - [3] Ernest D. Courant and Hartland S. Snyder. Theory of the alternating-gradient synchrotron. *Annals of physics*, 3:1–48, 1958.
  - [4] E. Huttel, I. Birkel, A.-S. Müller, and P. Wesolowski. A Single Bunch Electron Gun for the ANKA Injector. In *Proceedings of the 23rd Particle Accelerator Conference (PAC), Canada*, pages 602–604, 2009.
  - [5] L. Praestegaard. *Investigations of the ANKA Injector: Lattice, Beam Properties and Performance*. PhD thesis, University of Aarhus, Denmark, 2001.
  - [6] D. Einfeld, F. Pérez, S. Voigt, A. Fabris, C. Pasotti, and M. Svandrlik. Status of the RF System for the ANKA Storage Ring. In *Proceedings of the 18th Particle Accelerator Conference (PAC)*, volume 2, pages 809–811, 1999.
  - [7] A. Mochihashi, E. Blomley, T. Boltz, E. Huttel, and M. Schuh. Longitudinal Beam Manipulation by the RF Phase Modulation at the Karlsruhe Research Accelerator. In *Proceedings of the 10th International Particle Accelerator Conference (IPAC), Melbourne, Australia, 19-24 May*, pages 3123–3126, Geneva, Switzerland, 2019. doi: doi:10.18429/JACoW-IPAC2019-WEPTS016.
  - [8] E. Huttel, I. Birkel, A.-S. Muller, Francis Perez, and Montse Pont. Studies of Beam Lifetime at ANKA. In *Proceedings of the 20th Particle Accelerator Conference (PAC)*, volume 2, pages 893 – 895 Vol.2, 06 2003. doi: 10.1109/PAC.2003.1289523.
  - [9] S. Hermle, D. Einfeld, and E. Huttel. Layout of the Absorbers for the Synchrotron Light Source ANKA. In *Proceedings of the 18th Particle Accelerator Conference (PAC)*, volume 2, pages 1360–1362, 1999.
  - [10] E. Huttel, I. Birkel, A.-S. Müller, and P. Wesolowski. Low Beta Structure for the ANKA Storage Ring. In *Proceedings of the 11th European Particle Accelerator Conference (EPAC), Italy*, pages 2034–2036, 2008.
  - [11] V.H. Mezentsev, N.; Volkov, A.A.; Skaruba, V.; Khrushchev, S.; Tsukanov, V.; Migninskaya, E.; Syrovatin, V.M.; Lev. Final Design Report Superconducting Multipole Wiggler for ANKA CATACT beamline, 2012.
-

- 
- [12] S. Casalbuoni, A. Cecilia, S. Gerstl, N. Glamann, A. Grau, T. Holubek, C. Meuter, D. Saez de Jauregui, R. Voutta, C. Boffo, Th. Gerhard, M. Turenne, and W. Walter. Overview of the superconducting undulator development program at ANKA. *AIP Conference Proceedings*, (1), 2016. doi: 10.1063/1.4952781.
- [13] N Mezentsev, A A Volkov, V Shkaruba, S Khrushchev, K Zolotarev, A Bragin, I Poletaev, V Tsukanov, V M Syrovatin, V H Lev, A Zorin, and Tarasenko O. Technical Report: ANKA CLIC Superconducting Multipole Wiggler, 2016.
- [14] Lothar Weinhardt, Ralph Steininger, Dagmar Kreikemeyer-Lorenzo, Stefan Mangold, Dirk Hauschild, David Batchelor, Thomas Spangenberg, and Clemens Heske. X-SPEC: a 70eV to 15keV undulator beamline for X-ray and electron spectroscopies. *Journal of Synchrotron Radiation*, 28(2):609–617, 2021. doi: 10.1107/S1600577520016318.
- [15] S. Casalbuoni, E. Blomley, N. Glamann, A. Grau, T. Holubek, E. Huttel, D. Saez de Jauregui, S. Bauer, C. Boffo, Th. Gerhard, M. Turenne, and W. Walter. Commissioning of a Full Scale Superconducting Undulator with 20 mm Period Length at the Storage Ring KARA. *AIP Conference Proceedings*, 2054(1), 2019. doi: 10.1063/1.5084588.
- [16] D. Einfeld, S. Hermle, E. Huttel, R. Rossmanith, and R. Walther. The Injection Scheme for the ANKA Storage Ring. In *Proceedings of the 6th European Particle Accelerator Conference (EPAC), Stockholm*, pages 2135–2137, 1998.
- [17] A. I. Papash, E. Blomley, M. Brosi, J. Gethmann, B. Kehrer, A.-S. Mueller, M. Schuh, P. Schoenfeldt, and J. L. Steinmann. Non-Linear Optics and Low Alpha Operation at the Storage Ring KARA at KIT. In *Proceedings of the 9th International Particle Accelerator Conference (IPAC), 29 April-04 May, Vancouver, BC, Canada*, number 9, pages 4235–4238, Geneva, Switzerland, 2018. doi: doi:10.18429/JACoW-IPAC2018-THPMF070.
- [18] N. Hiller, A. Hofmann, E. Huttel, V. Judin, B. Kehrer, M. Klein, S. Marsching, A.-S. Müller, et al. Status of Bunch Deformation and Lengthening Studies at the ANKA Storage Ring. In *Proceedings of the 2nd International Particle Accelerator Conference (IPAC), Spain*, pages 2951–2953, 2011.
- [19] F. Perez, I. Birkel, E. Huttel, A.-S. Muller, and M. Pont. Beam size and bunch length measurements at the ANKA storage ring. In *Proceedings of the 20th Particle Accelerator Conference (PAC)*, 2003.
- [20] P. Schreiber, T. Boltz, M. Brosi, B. Haerer, A. Mochihashi, A.-S. Mueller, A. I. Papash, and M. Schuh. Status of Operation With Negative Momentum Compaction at KARA. In *Proceedings of the 10th International Particle Accelerator Conference (IPAC), Melbourne, Australia, 19-24 May*, number 10, pages 878–881, Geneva, Switzerland, 2019. doi: doi:10.18429/JACoW-IPAC2019-MOPTS017.
-

- 
- [21] A. I. Papash, E. Blomley, T. Boltz, M. Brosi, E. Bruendermann, S. Casalbuoni, J. Gethmann, E. Huttel, B. Kehrer, A. Mochihashi, A.-S. Mueller, R. Ruprecht, M. Schuh, and J. L. Steinmann. New Operation Regimes at the Storage Ring KARA at KIT. In *Proceedings of the 10th International Particle Accelerator Conference (IPAC), 19-24 May, Melbourne, Australia*, number 10, pages 1422–1425, Geneva, Switzerland, 2019. doi: doi:10.18429/JACoW-IPAC2019-TUPGW016.
- [22] A.-S. Müller, N. Hiller, A. Hofmann, E. Huttel, K. Il'in, V. Judin, B. Kehrer, M. Klein, S. Marsching, C. Meuter, S. Nakhaimueang, M. J. Nasse, A. Plech, P. Probst, A. Scheuring, M. Schuh, M. Schwarz, M. Siegel, N. J. Smale, M. Streichert, F. Caspers, A. Semenov, H.-W. Hübers, and E. Bründermann. Experimental Aspects of CSR in the ANKA Storage Ring. *ICFA Beam Dynamics Newsletter*, 57:154–165, 2012.
- [23] Dmitry Teytelmann. *BPMH-20-2G Data Sheet*. Dimtel Inc., 2012. , Revision 1.1 May 2012.
- [24] Dmitry Teytelmann. *FBE-500LT Bunch-by-bunch Feedback Front/Back-End Technical User Manual*. Dimtel Inc., 2011. , Revision 1.1 May 2011.
- [25] M. Dehler, V. Schlott, D. Bulfone, M. Lonza, and R. Ursic. Current status of the ELETTRA/SLS transverse multi bunch feedback. In *Proceedings of the 7th European Particle Accelerator Conference (EPAC), 26.-30. June, Vienna, Austria*, pages 1894–1896, 2000.
- [26] Shahroz Khan, Torsten Knuth, Gallo Alessandro, Fiorella Marcellini, B. Sparato, and M. Zobov. Longitudinal and transverse feedback kickers for the BESSY II storage ring. In *Proceedings of the 18th Particle Accelerator Conference (PAC), New York, USA*, pages 1147 – 1149, 02 1999. doi: 10.1109/PAC.1999.795477.
- [27] R. Boni, A. Gallo, A. Ghigo, F. Marcellini, M. Serio, and M. Zobov. A waveguide overloaded cavity as longitudinal kicker for the DAPHNE bunch-by-bunch feedback system. *International Workshop on Collective Effects and Impedance for B-Factories.*, 52:95–113, 1996.
- [28] Michiko G Minty and Frank Zimmermann. *Measurement and Control of Charged Particle Beams*. Particle Acceleration and Detection. Springer, 2003.
- [29] D. Teytelman. Experience with feedback systems in modernsynchrotron light sources. Accelerator Performance and Concepts Workshop Frankfurt, 2018.
- [30] Julian Gethmann. *Beam Dynamics Studies with a Superconducting Damping Wiggler at KARA [Unpublished Manuscript]*. PhD thesis, Karlsruhe Institute of Technology, 2021.
- [31] Anže Zupanc, Igor Križnar, Mark Pleško, and Urban Simončič. Orbit Correction with Frequency in Java. In *Proceedings to the 4th International Workshop on Personal Computers and Particle Accelerator Controls*, 2002.
-

- 
- [32] G. Portmann, Jeff Corbett, and Andrei Terebilo. An Accelerator Control Middle Layer using MATLAB. In *Proceedings of the 21st Particle Accelerator Conference (PAC)*, 2005.
- [33] F. Pedregosa, G. Varoquaux, A. Gramfort, V. Michel, B. Thirion, O. Grisel, M. Blondel, P. Prettenhofer, R. Weiss, V. Dubourg, J. Vanderplas, A. Passos, D. Cournapeau, M. Brucher, M. Perrot, and E. Duchesnay. Scikit-learn: Machine learning in Python. *Journal of Machine Learning Research*, 12:2825–2830, 2011.
- [34] S. Marsching, E. Huttel, M. Klein, A. S. Mueller, and N. J. Smale. First Experience with the Matlab Middle Layer at ANKA. In *ICALEPCS*, volume 11, page 253, 2011.
- [35] A. S. Muller, I. Birkel, E. Huttel, F. Perez, M. Pont, and F. Zimmermann. Studies of current dependent effects at ANKA. In *Proceedings of the 9th European Particle Accelerator Conference (EPAC) July 5-9, Lucerne, Switzerland*, 2004.
- [36] Pedro F. Tavares, Miriam Fitterer, Nicole Hiller, Andre Hofmann, Erhard Huttel, Vitali Judin, Marit Klein, Sebastian Marsching, Anke-Susanne Muller, Nigel John Smale, et al. Beam Coupling Impedance Measurements at the ANKA Electron Storage Ring. In *Proceedings of the 1st International Particle Accelerator Conference (IPAC), 23.-28. May, Kyoto, Japan*, 2010.
- [37] Emanuel Karantzoulis, Victor Smaluk, and Lidia Tosi. Broad band impedance measurements on the electron storage ring elettra. *Physical Review Special Topics-accelerators and Beams*, 6, 03 2003. doi: 10.1103/PhysRevSTAB.6.030703.
- [38] J. Gareyte. Impedances: Measurements and Calculations for Non-symmetric Structures this conference. In *Proceedings of the 8th European Particle Accelerator Conference (EPAC) June 3-7, Paris, France*, pages 89 – 93, 2002.
- [39] N. Hiller, A. Borysenko, E. Hertle, E. Huttel, V. Judin, B. Kehrer, S. Marsching, A.-S. Müller, M. J. Nasse, A. Plech, M. Schuh, and N. J. Smale. ELECTRO-OPTICAL BUNCH LENGTH MEASUREMENTS AT THE ANKA STORAGE RING. In *Proceedings of the 4th International Particle Accelerator Conference (IPAC), Shanghai, China*, pages 500–502, 2013.
- [40] B. Kehrer, N. Hiller, A. Hofmann, E. Huttel, V. Judin, M. Klein, S. Marsching, A. S. Mueller, N. Smale, et al. Filling Pattern measurements at the ANKA storage ring. In *Proceedings of the 2nd International Particle Accelerator Conference (IPAC) San Sebastián, Spain*, pages 1209–1211, 2011.
- [41] Johannes L. Steinmann, Edmund Blomley, Miriam Brosi, Erik Brueundermann, Michele Caselle, Jeffrey L. Hesler, Nicole Hiller, Benjamin Kehrer, Yves-Laurent Mathis, Michael J. Nasse, Juliane Raasch, Manuel Schedler, Patrik Schönfeldt, Marcel Schuh, Markus Schwarz, Michael Siegel, Nigel Smale, Marc Weber, and Anke-Susanne Müller. Frequency-comb spectrum of periodic-patterned signals. *Phys. Rev. Lett.*, 117, 2016. doi: 10.1103/PhysRevLett.117.174802.
-

- [42] M. Caselle, Lorenzo Rota, A. Kopmann, S. A. Chilingaryan, M. Mahaveer Patil, W. Wang, E. Bruendermann, S. Funkner, M. Nasse, G. Niehues, M. Norbert Balzer, M. Weber, A. S. Mueller, and S. Bielawski. Ultrafast linear array detector for real-time imaging. In *Optical Data Science II*, pages 1 – 9. International Society for Optics and Photonics, 2019. doi: 10.1117/12.2508451.
- [43] M. Brosi, J. L. Steinmann, E. Blomley, E. Bruendermann, M. Caselle, N. Hiller, Benjamin Kehrer, Yves-Laurent Mathis, Michael J. Nasse, Lorenzo Rota, Manuel Schedler, Patrik Schönfeldt, Marcel Schuh, Markus Schwarz, Marc Weber, and Anke-Susanne Müller. Fast mapping of terahertz bursting thresholds and characteristics at synchrotron light sources. *Phys. Rev. Accel. Beams*, 19, 2016. doi: 10.1103/PhysRevAccelBeams.19.110701.
- [44] Anke-Susanne Müller. Accelerator-based sources of infrared and terahertz radiation. *Reviews of Accelerator Science and Technology*, 03(01):165–183, 04 2010. doi: 10.1142/S1793626810000427.
- [45] M. Caselle, M. Balzer, S. Chilingaryan, M. Hofherr, V. Judin, A. Kopmann, N. J. Smale, P. Thoma, S. Wuensch, A. S. Mueller, M. Siegel, and M. Weber. An ultra-fast data acquisition system for coherent synchrotron radiation with terahertz detectors. *Journal of Instrumentation*, 9(01):C01024–C01024, jan 2014. doi: 10.1088/1748-0221/9/01/c01024.
- [46] A.-S. Müller, I. Birkel, E. Huttel, and P. Wesolowski. Analysis of Multi-Turn Beam Position Measurements in the ANKA Storage Ring. In *Proceedings of the 22nd Particle Accelerator Conference (PAC)*, volume 2, pages 809–811, 2007.
- [47] S. Marsching, N. Hiller, E. Huttel, V. Judin, B. Kehrer, M. Klein, C. Meuter, A.-S. Mueller, M. J. Nasse, M. Schuh, et al. Commissioning of a new beam-position monitoring system at anka. In *Proceedings of the 3rd International Particle Accelerator Conference (IPAC), May 20.-25., New Orleans, USA, 2012*.
- [48] Alan V. Oppenheim and Ronald W. Schaffer. *Harmonic Analysis and Applications*. Pearson, third edition edition, 2014.
- [49] M. Svandrlik, A. Fabris, and C. Pasotti. Coupled Bunch Instability Calculations for the ANKA Storage Ring. In *Proceedings to the 6th European Particle Accelerator Conference (EPAC) Stockholm, Sweden, June 22-26, 1998*, 1998.
- [50] E. Blomley, A.-S. Mueller, and M. Schedler. Beam Studies with a New Longitudinal Feedback System at the ANKA Storage Ring. In *Proceedings of the 7th International Particle Accelerator Conference (IPAC), May 8-13, Busan, Korea*, number 7, pages 2658–2660, Geneva, Switzerland, 2016. doi: 10.18429/JACoW-IPAC2016-WEPOR001.
- [51] B. Kehrer et al. Visible Light Diagnostics at the ANKA Storage Ring. In *Proceedings of the 6th International Particle Accelerator Conference (IPAC), Richmond*,
-

- VA, USA, May 3-8, number 6, pages 866–868, Geneva, Switzerland, 2015. doi: 10.18429/JACoW-IPAC2015-MOPHA037.
- [52] K. C. Harkay et al. Characterizing the Coupled Bunch Driving Terms in a Storage Ring. In *Proceedings of the 6th International Beam Instrumentation Conference (IBIC), Grand Rapids, MI, USA, 20-24 August*, number 6, pages 21–27, Geneva, Switzerland, 2017. doi: 10.18429/JACoW-IBIC2017-MO3AB1.
- [53] S. Marsching. *Cassandra PV Archiver Reference Manual v3.2.6*. aquenos, 2019. URL <https://oss.aquenos.com/cassandra-pv-archiver/docs/3.2.6/manual/html/>.
- [54] S. Marsching. Scalable Archiving with the Cassandra Archiver for CSS. In *Proceedings of the 14th International Conference on Accelerator and Large Experimental Physics Control Systems (ICALEPCS), San Francisco, CA, USA, 2013*.
- [55] Stefan Ritt. *Electronic Logbook*. URL <https://elog.psi.ch/elog/>.
- [56] Python Software Foundation. *Python*. URL <https://www.python.org/about/>.
- [57] Matthew Newville. *EPICS Channel Access for Python*. URL <https://cars9.uchicago.edu/software/python/pyepics3/>.
- [58] Simon Gregor Ebner. *Native Python Interface for ELog*. URL [https://github.com/paulscherrerinstitute/py\\_elog](https://github.com/paulscherrerinstitute/py_elog).
-

# Acknowledgments

*The acknowledgments will be mostly written in German.*

Mein Dank geht zuallererst an meine Professorin Dr. Anke-Susanne Müller, die es mir überhaupt erst ermöglicht hat an meiner Dissertation zu arbeiten und dies auch über einen deutlich längeren Zeitraum als sonst üblich. Danken möchte ich auch an meinen Korreferenten Prof. Dr. Günter Quast. Zudem geht mein Dank an meinen Betreuer Dr. Akira Mochihashi für die unzähligen Diskussionen und Motivation beim zusammenschreiben meiner Arbeit und an meine Graduiertenschule KSETA, die mir den Blick über den Tellerrand ermöglicht hat und mich auch direkt finanziell unterstützen konnte.

Mein weiterer Dank geht an meine Arbeitsgruppe und meine ehemaligen Kollegen Nicole, Vitali und Benjamin, die mit unzähligen und sehr spaßigen (Nacht-)Messschichten und Diskussionen immer für sehr viel Spaß bei der Arbeit gesorgt haben. Zudem kamen so auch viele Wünsche und Anforderungen auf, die mich weiter motiviert haben und deren Umsetzungen zumindest auch teilweise in meine Doktorarbeit eingeflossen sind. Speziell erwähnen möchte ich an dieser Stelle noch Julian, mit dem ich vor allem in der letzten Phase, in der wir beide unsere Arbeit zum Abschluss gebracht haben, sowohl ein Büro, als auch viel Zeit mit Python verbracht haben. Was nicht nur Spaß gemacht, sondern letztendlich auch essenziell für die technische Seite meiner Auswertung geworden ist.

Wichtig zu erwähnen sind auch meine Korrekturleser Markus, Andrea, Johannes und Miriam. Ins besondere gilt mein Dank auch meinem Schwiegervater, der die undankbare Aufgabe hatte als Fachfremder die komplette Arbeit zu lesen und mein Englisch zu korrigieren.

Mein besonderer Dank geht aber an meine Familie, meine Geschwister und meine Freunde. Ins besondere meine Frau Rosmarie, die oft viele Kompromisse im beruflichen, wie auch privaten Bereich eingegangen ist, um mir den Abschluss dieser Arbeit zu ermöglichen und meinen Kindern und Freunden, die mich in stressigen Zeiten immer erden konnten. Aber auch meinen Eltern, die immer an mich geglaubt, mich motiviert und mich auf meinem Weg unterstützt haben, so lange sie es konnten. Es macht mich sehr traurig, dass leider beide den Abschluss meiner Doktorarbeit nicht mehr miterleben konnten.

Last, but not least, I would like to thank Dmitry Teytelman for his tremendous help in discussing techniques, ideas and for providing examples of how to work with the feedback system, as well as for endless explanations to the many questions that I had. This thesis would not have been possible without his help.

---